Alma Mater Studiorum – Università di Bologna

DOTTORATO DI RICERCA IN

INGEGNERIA CIVILE E AMBIENTALE

Ciclo XXVI

Settore Concorsuale di afferenza: 08/A1

Settore Scientifico disciplinare: ICAR/01

ANALYSIS AND MATHEMATICAL MODELING OF WAVE-STRUCTURE INTERACTION

Presentata da:

Andrea Natalia Raosa

Coordinatore Dottorato

Chiar.mo Prof. Alberto Lamberti

Relatore

Prof. Barbara Zanuttigh

Relatore

Prof. Javier L. Lara

Esame finale anno 2013-2014

Index

LIST OF FIGURES

LIST OF TABLES

CHAPTER 1

INTRODUCTION

1.1 Motivations

Shore protection against erosion has turned to be a major issue in a great part of the worldwide coastal areas. About 80% of the world shorelines are under an erosion process while 70% of the global human population, representing 4 billions of persons, live in a 60 km-wide strip contiguous to the sea. The natural tendency of coastal erosion has been dramatically accelerated by the impact of human activities, and the average rate of shoreline recession in some coastal sites of the world reaches values of tens of meters a year (Komar, 1998; Pilkey and Hume, 2001). In particular, in the countries of the European Union, about 20.000 km of coasts, i.e. 20% of the European coasts, are to some extent affected by erosion, being most of them actively retreating. The area lost or seriously impacted by erosion is estimated to be 15 km^2 per year. Extensive coastal areas in the Netherlands, England, Germany, Poland and Italy are already at an altitude lower than the levels of the high tide and therefore inherently more vulnerable to flooding. At the same time, over the past 50 years, the population living in European coastal municipalities has more than doubled to reach 70 millions inhabitants in 2001 (EUROSION UE project).

Hence, the population and development pressures on the coastal zones require life and property defense policies from coastal hazards and the definition of technical alternatives for shore protection. The response options to eroding coasts are multifold, and have been basically split into “soft” solutions, mainly beach nourishment designs, and “hard” solutions of shoreline stabilization using seawalls, grayness and offshore breakwaters.

Climate change will have significant impacts on coastal areas, due to the sea level rise (based on the SRES scenarios in the range 0.2-0.8 m/century) and the increased frequency

and intensity of extreme events. So, the large stretches of the coast that are protected by hard structures, are very sensitive to rising average sea level because these kind of structures will be more frequently overflowed and the shoreline will consequently subject to greater wave energy remaining. These elements make essential an accurate knowledge of the phenomena of wave-structure interaction and the rising wave on the beach and / or dunes which over time can be eroded until the formation of a breach.

The University of Bologna has leaded the investigation tasks of the THESEUS project and the present PhD Thesis has been realised in the frame of this project. One of the main objectives of the project was to analyse innovative technologies aimed at the mitigation of the flood and erosion risk (as resilient dikes or over-washed structures).

The increase of frequency and intensity of storms, combined with the uncertainties related to extreme events and climate change, carries an increased the risk of flooding of low lying areas, an accelerate erosion of exposed soft beaches and a challenges in the long term design of coastal protection structures. The aim of this thesis work, included within the THESEUS project, is the development of a mathematical model 2DV two-phase, based on an existing code, able to represent the real conditions of inundation i.e able to represent together the overtopping phenomenon on emerged/submerged structures and the sediment transport.

1.2 Background

Traditionally wave-structure interaction has been studied through physical tests (two- and three-dimensional, small- and large- scale model tests). Empirical formulations arisen from physical modeling present several restrictions and a narrow range of applicability. Many other issues related with scale factors or processes such as porous media flow, wave impacts or viscous effects are not correctly represented in the experiments. A great effort has been made over the last decade in the numerical modeling of wave interaction with coastal structures to overcome these limitations.

A similar consideration can be made also for the study of the sediment transport. In fact, field experimentation is challenging due to the difficulty and expense in deploying equipment, obtaining robust data and the variability of meteorological conditions. Although, laboratory measurements have some limitations, due to the constrained circumstances compared with the field, the data obtained are the most reliable for investigating processes and for validating models. Meanwhile, developments in computational hardware and numerical solution methods have driven the popularity of numerical modeling of coastal hydrodynamics.

Several approaches have been followed to study the wave-structure interaction, the induced hydrodynamic and the consequently mixing and sediment suspension. Among other existing approaches, Nonlinear Shallow Water (NSW), Boussinesq-type or Navier-Stokes equations models have traditionally been used.

Good results in terms of averaged magnitudes have been obtained using NSW equation (Kobayashi et al., 2007), though vertical velocity structure cannot be resolved using this approach and the energy transfer to higher frequencies occurring before wave breaking cannot be reproduced accurately due to the lack of dispersion.

Boussinesq-type models are able to include frequency dispersion, a depth-dependent velocity profile, and they can be applied to both breaking and non-breaking wave conditions. A great effort has been made in order to relax the original equations by deriving the extended Boussinesq equations (Kirby, 2003). However, this type of models requires setting both the triggering wave breaking mechanism and the subsequent wave energy dissipation due to wave breaking. Moreover, these models fail to reproduce the strong nonlinear shoaling prior to wave breaking and the free-surface and velocity higher order statistics which are thought to be relevant for structure stability.

Navier-Stokes equations models assume a number of simplifications in the equations lower than in other approaches. These models are able to calculate flows in complex geometries and provide very refined information on the velocity, pressure and turbulence field. Models based on a two dimensional eulerian Navier-Stokes set of equations (Losada et al., 2008; Lara et al., 2008; Guanche et al., 2009; Lara et al., 2011) have proven to be powerful to address wave-induced processes. Wave reflection and

overtopping have been reproduced numerically with a high degree of accuracy, introducing new models to be used as a complementary tool in the design process. These types of models are so accurate and promising that 3D applications were developed (P. Higuera et al., 2013).

Wave-structure interaction and wave run-up on beaches and/or dunes require models capable to deal with steep and emerged slopes. Traditional 2DH numerical models, such as Mike21 Shallow Water equations model (SW+HD modules), can be applied only when the structure/beach is submerged. Other models, such as the Boussinesq models (as Mike 21 BW module) can be powerful tools for run-up and overtopping in case of steep slopes up to 1:3 but so far are time consuming tools (high spatial resolution, low Courant number) and need the introduction of a lot of artificial dissipation usually to avoid instabilities: application thus depends on the extension of the area to be modelled and on the phenomena to be included (wave breaking, wave run-up). Moreover, existing Boussinesq models do not include the representation of sediment transport do that beach/dune reshaping during storms and possible breaching cannot be reproduced. So far only RANS-VOF models can deal with wave run-up and overtopping on steep slopes (also structures, slopes 1:2) without the inclusion of many artifices.

1.3 Definition of the objectives

The overall aim of this thesis is to develop a tool that can represent wave run-up and overtopping together with beach reshaping during storms. Actually what can be a more promising research field, due to the lack of good representation for many of the related processes, is the modellisation of the swash zone that is an area of greatest importance both for flooding issues and ecosystem conservation.

The specific objectives of the present study are:

- to characterize the flow (velocities and layer thicknesses) on the crest of the structure in order to extend the theoretical models and provide criteria for the design of structures close to mean sea level or overwashed;

- to introduce in a two-dimensional numerical model based on the Reynolds Averaged Navier–Stokes equations (RANS), called IH-2VOF (Losada et al., 2008), new equations for the representation of the sediment transport;
- to verify the model as a reliable tool for the simulation of wave-structures interactions and sediment transport dynamics.

1.4 Outline

The present thesis is organized following the objectives listed above.

In chapter 1, an introductive description of the work and the objectives of the study are presented.

In chapter 2, a state-of-the-art review of both experimental and mathematical the modelling of sediment transport is included.

In chapter 3, the characteristics of the numerical model used to carry out the present work are described. The governing equations and main mathematical assumptions, free surface tracking method and resolution procedure are presented.

In chapter 4, previously the existing theories for the overtopping process are described, than the numerical tests and its set-up for the study of wave overtopping process above a particular kind of coastal defense structure are introduced. The key results obtained by the numerical simulation (for example the influence of the seaward-landward slope and of the dike submergence), the analysis of the wave flow characteristics above the structure and the comparison with the theoretical approach are reported.

In chapter 5, the modifications of the initial code are reported. New equations implemented for the representation of the sediment transport in a two-phase model are shown and described.

In chapter 6, the stages and results of the two-phase model verification process are presented.

In chapter 7, conclusions and discussion are finally drawn.

CHAPTER 2

SEDIMENT TRANSPORT MODELLING IN THE SWASH ZONE. STATE OF THE ART.

The surf and swash zones are hydrodynamically active regions. Nearshore breaking waves play a paramount role in coastal morphology and influence most coastal processes. These waves produce highly turbulent regions causing significant mixing and sediment suspension. The suspended sediments are transported by the nearshore currents induced by breaking waves. Moreover, breaking waves impact offshore structures and should be considered in their design. Fluid and sediment interactions occurring in the swash zone determine the erosion or accretion of a beach and act as boundary conditions for nearshore hydrodynamic and morphodynamic models. A schematic illustration of the surf and swash zones is shown in Figure 2.1.

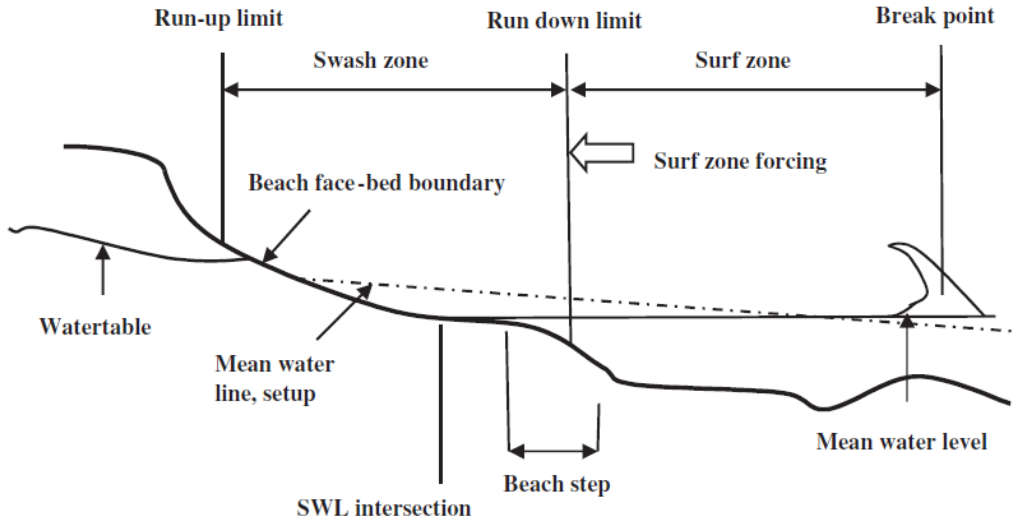

Figure 2.1. Schematic illustration of swash zone (Elfrink and Baldock, 2002).

In this chapter a critical review of conceptual and mathematical models developed in recent decades on sediment transport in the swash zone is presented.

Evidently, the hydrodynamics of the swash zone are complex and not fully understood. Key hydrodynamic processes include both high-frequency bores and low-frequency infragravity motions, and are affected by wave breaking and turbulence, shear stresses and bottom friction. The prediction of sediment transport that results from these complex and interacting processes is a challenging task. Besides, sediment transport in this oscillatory environment is affected by high-order processes such as the beach ground water flow. Most relationships between sediment transport and flow characteristics are empirical, based on laboratory experiments and/or field measurements. Analytical solutions incorporating key factors such as sediment characteristics and concentration, waves and coastal aquifer interactions are unavailable. Therefore, numerical models for wave and sediment transport are widely used by coastal engineers.

2.1 Parametric and empirical modeling of cross-shore swash zone sediment transport

The swash zone sediment transport and foreshore evolution have been analyzed in several studies (e.g., Masselink et al., 2005; Miles et al., 2006). Empirical formulas based on numerous experiments on steady flow have been implemented to describe the amount of sediment transport (Nielsen, 1990). Most of these formulas were based on the relationship between the Shields parameter (Shields, 1936) and the dimensionless sediment transport rate.

Madsen (1991) derived a sediment transport rate formula for the instantaneous bed-load $q_b(t)$ that was further generalized by Madsen (1993). Masselink and Hughes (1998) found that Bagnold's energetics-based bed-load sediment transport equations fitted their field data, and concluded that formulae based on a modified Shields parameter could also be used. Since physically the up-rush and back wash flows are different, it seems logical that the associated sediment transport processes can also be different. Masselink and Hughes (1998) showed that swash zone sediment transport rate formula required different empirical constants (C) in order to fit measured velocities and sediment transport rates in both up-rush and back wash phases of the swash.

On one hand, the modeling approach using two different values of model coefficient is consistent with differences between the up wash and back wash (flow characteristics and sediment transport modes) as speculated by previous researchers (Nielsen, 2002). On the other hand, our limited understanding of the up wash and back wash hydrodynamics prevents us from quantifying further these coefficients for different conditions (different values have been obtained for different data sets; i.e., they remain empirical). Nielsen (2002) presented two mechanisms for the sediment transport during up-rush:''(i) the existence of higher shear stresses during up-rush; and (ii) the existence of pre-floating sediment from the bore collapse (Masselink and Hughes, 1998)''. The shear stress of the bed was modeled by the time series of the free stream velocity in terms of the wave boundary layer model plus a phase lead φ_τ of the bed shear stress, compared with the free stream velocity at the peak frequency. He postulated that the total amount of sediment transport during up-rush and back wash is well estimated by the model without the need for incorporating different multipliers for up-rush and back wash and suggested that the range in C values is 9.7 ± 0.2 (Nielsen,2002). It should be noted that although the total amount of sediment transport is the same, the timing of sediment transport rate has not yet been accurately modeled due to the very unsteady nature of the swash zone and the existence of pre-floated sediments. Besides, some mechanisms have not been considered in this formulation. For example, the observed lag between the instantaneous bed shear stress and the rate of sediment transport has not been considered (Nielsen,2002).

Larson et al. (2004) developed the sediment transport formulae to predict the net transport rate over many swash cycles and compared the predictions with field data. Net sediment transport rate sand the formulae developed to calculate the net sediment transport in the swash zone showed good agreement with transport rate measurements at the seaward end of the swash.

Drake and Calantoni (2001) added an extra term to the Bailard formula to account for acceleration effects and showed that the inclusion of acceleration effects improved the performance of the transport model. Puleo et al. (2003) also modified an energetics model for sediment transport to include the effect of fluid acceleration and were able to

strongly reduce the prediction error. Pedrozo-Acuña et al. (2007) modified the bed-load formulation to include an acceleration term similar to that proposed by Drake and Calantoni (2001):

$$q_b(t) = \begin{cases} 0 & for\ \theta < \theta_{\beta crit} \\ \frac{C}{1 + tan\beta / tan\emptyset}(\theta - \theta_{cr})^{3/2}\frac{u_b}{|u_b|} + K_a(a - a_{crit}) & for\ \theta \geq \theta_{\beta crit} \end{cases} \quad (2.1)$$

where θ is the Shields parameter; β is the local beach angle; $\emptyset$ is the friction angle for a moving grain; u_b is the horizontal velocity at the sea floor; a_{crit} is the acceleration threshold and K_a is the efficiency. The acceleration is calculated by differentiating the velocity time series from the hydrodynamic model. The addition of an acceleration term does not by itself improve the prediction. However, it enables morphological models to predict on shore migration of bars, in accordance with results shown by previous researchers (Pedrozo-Acuña etal., 2007).

Karambas (2003,2006) derived the non-dimensional sediment transport rate based on modified Meyer-Peterand Muller (1948) formula using different values the multiplier C for up-rush and back wash that includes infiltration/exfiltration effects.

Note that a Shields-type transport formula does not account for inertial forces, which may become significant for coarse grains due to the high fluid accelerations during up wash (Baldock and Holmes, 1997). In summary, none of the above models can resolve all potentially important details of the flow and sediment transport in the swash zone, such as the wave boundary layer, percolation, flow separation at the beach step and the 2D or 3D distribution of suspended sediments. Despite these efforts, the energetics-based models are unable to account for the phase difference between the sediment transport rate and hydrodynamic forcing parameters. Hsu and Raubenheimer (2006) indicated that sediment transport in the swash zone might not correlate to the instantaneous forcing computed in a specific location, so such equations might not be valid in the swash. A means to make progress on this issue are process-based and a two-phase modeling approach.

2.2 Longshore sediment transport rate (LSTR)

The longshore current generated by obliquely incident breaking waves plays an important role in transporting sediment in the swash zone and is a key component of most coastal engineering studies (Kumar et al.,2003). Under obliquely incident waves, near shore sediment moves in a zig-zag way that results in LST in the swash zone (Asano, 1994).

The cross-shore distributions of LST indicate three distinct zones of transport: the incipient breaker zone, the inner surf zone and the swash zone (Smith et al., 2004). A peak in transport occurs for plunging waves in the incipient breaker zone, indicating that this breaker type suspends more sediment for transport. The breaker is a function of wave height, period and beach slope. In the inner surf zone, wave height is the dominating factor in controlling sediment transport, which depends less on wave period. Swash zone sediment transport, which accounts for a significant percentage of the total transport, shows a dependence on wave height, period and beach slope. The occurrence of the increased longshore flow velocities in the swash zone is related to differences in fluid motion between the inner surf zone and swash zone (Smith et al., 2004).

In the surf zone, the oscillatory part of the flow is directed more or less perpendicular to the wave crests. In the swash zone, however, the flow direction during up-rush is perpendicular to the wave crest, but perpendicular to the beach orientation during backwash, in the absence of longshore current. This effect increases with increasing bed slope or, rather, the surf similarity parameter (Elfrink and Baldock, 2002).

Bijker's (1971) LST formula is one of the earliest formulae developed for waves and currents in combination. It is based on a transport formula for rivers proposed by Kalinske–Frijlink (Frijlink, 1952). Bailard (1981) developed an energy-based surf zone sediment transport model based upon Bagnold (1963, 1966) steady flow models. His model has both bed-load and suspended load components. Both components were expressed in terms of various instantaneous velocity components, which limited the model's usefulness. The gross LST is mainly computed with the CERC formula (Shore Protection Manual, 1984) in engineering applications. This model, which is based on the assumption that the total LSTR is proportional to longshore energy flux, was developed

from the pioneering work of Bagnold in the early 1960s and further developed by Komar and Inman (1970). The sediment transport rate was also calculated using the breaker height, surf zone width and average longshore current velocity in the surf zone (Walton and Bruno, 1989). Kamphuis (1991) performed laboratory experiments on sediment transport due to oblique wave attack and found two peaks in the LSTR: one in the surf zone and one in the swash zone. Kamphuis (1991) expanded his earlier work and developed a relationship for estimating LSTR based upon dimensional analysis and calibrated it using experiments within a physical model. Kamphuis (2002) found the equation to be applicable to both field and laboratory data. Watanabe (1992) proposed a formula for the total load. The Watanabe formula and its coefficient values have been calibrated and verified for a variety of laboratory and field data sets. Nevertheless, it has not yet been recognized whether the value of the non-dimensional coefficient in the formula is a constant or it depends on the wave and sediment conditions.

Bayram et al. (2001) studied the cross-shore distribution of LST and evaluate the predictive capability of well-known sediment transport formulae, based upon field data sets. They pointed out that no existing sediment transport formula has taken into account all the different factors that control LST in the surf and swash zones. Kumar et al. (2003) compared measurement and estimation of LSTR for data from the central west coast of India. Tajima (2004) developed a computer routine to model surf zone sediment transport. The code is in the form of two programs that run sequentially: a hydrodynamics model and a sediment transport model. The hydrodynamic model calculates the forcing functions needed to drive the sediment transport model at each point in the profile, and includes modules for nonlinear wave propagation, wave breaking, surface rollers and nearshore cur- rents. The sediment transport model calculates the transport at each profile point and includes bed-load and suspended load modules. The models selected are not intended to be inclusive, but merely representative of classes of models. The CERC equation, containing one term for the calculation of total load (combined bed-load and suspended load), is the simplest formula in general use. The Kamphuis formula is also a one-term, total load model, but explicitly includes the effects of wave period, beach slope and grain size. The Bailard formula is representative of models that divide the transport into bed-load and suspended load

transport. The Tajima model is representative of the complex computer routines that provide a stepwise model of hydrodynamics and sediment dynamics across the surf zone, and thus predict not only the total bed-load and suspended load LST, but also its cross-shore distribution.

Although some of the above models included the swash zone component, in most LST models, the swash transport contribution is either completely ignored or merely accounted for as part of the total sediment transport budget. Van Wellen et al. (2000) developed an engineering model, STRAND, to provide a simple engineering model of swash sediment transport on steep, coarse- grained beaches. Although a good correlation between their predictions and Kamphuis' laboratory data was obtained, new laboratory and field data are required to validate the model further. Kobayashi et al. (2007) developed a numerical model based on the time-averaged continuity, cross-shore momentum, longshore momentum, and energy equations to predict the longshore current and sediment transport on a sand beach of alongshore uniformity under unidirectional irregular breaking waves. For obliquely incident waves, the water particles in the run-up flow move on saw-tooth trajectories with net longshore displacement. There are three significant works on this procedure: Leont'yev (1999), Antuono et al. (2007), and Baba and Camenen (2008). Leont'yev (1999) studied the contribution of the swash zone to the total sediment transport and showed that the mean longshore transport velocity at the shoreline is proportional to the net longshore displacement per wave period. Antuono et al. (2007) investigated the integral properties of the swash zone and defined longshore shoreline boundary conditions for wave- averaged nearshore circulation models and found two main terms to contribute to the longshore drift velocity: (i) a drift-type term representing the momentum transfer due to wave breaking; and (ii) a term proportional to the shallow water velocity, accounting for short wave interactions, frictional swash forces and continuous forcing due to non-breaking wave nonlinearities. Baba and Camenen (2008) implemented a LST model for the swash zone in a beach evolution model based on the N-line approach. The erosion and the accumulation around the shoreline are clearly represented by the introduction of sediment transport in the swash zone. It was found that sediment transport in the swash zone has an important effect on beach evolution and could be one of the main contributors for the erosion/accumulation

processes close to the shoreline. Bakhtyar et al. (2008) calculated the LSTR in the nearshore using an Adaptive-Network-Based Fuzzy System (ANFIS). Their results reveal that the ANFIS model provides higher accuracy and reliability for LSTR estimation than empirical formulae.

The sediment transport models described include some aspects of a detailed deterministic approach. The main short- coming of these models is that they give a wide range of different predictions and, consequently, their reliability under changing wave conditions is uncertain.

2.3 Process-based numerical modeling of swash zone sediment transport

Numerical models become powerful tools for the understanding of sediment transport, hydrodynamics and morphology in the coastal areas, yet most of the sediment transport relationships between the sediment transport rate and flow parameters relations are based on empirical and experimental studies. Process-based numerical models simulate the major processes in the swash zone (interacting wave motion on the beach, coastal ground water flow, sediment transport) using a hydrodynamic model coupled with as wash zone sediment transport, beach profile change sand porous flow models. Different numerical techniques have been devised and practiced. In the following sections, the numerical methods frequently implemented in the swash zone analysis are reviewed.

2.3.1 Non-linear shallow water equations (NLSWE)

The solution to the shallow water wave equations is one of the classic problems for coastal engineers. This model describes the evolution of water surface elevation and depth-averaged velocity induced by small amplitude waves with large wave lengths compared to the water depth. The model assumes that the pressure distribution is hydrostatic everywhere, i.e., there is no variation of flow variables with depth other than the pressure. Swash hydrodynamics and run-up are traditionally modeled using the NLSWE, a simplification to the full Navier-Stokes equations. One general form of the NLSWE is

$$y_t + (yu)_x + (yv)_y = 0 \tag{2.2}$$

$$u_t + uu_x + uv_y + g\eta_x = 0 \tag{2.3}$$

$$v_t + vu_x + vv_y + g\eta_y = 0 \tag{2.4}$$

where y is the total water depth; u and v are the cross-shore and longshore velocity components.

Breaking waves and bore motions on a sloping beach were investigated by Carrier and Greenspan (1958) and Shen and Meyer (1963). The focus was on the collapse of the bore at the beach and the subsequent motion of the thin up-rush tongue and backwash flows. These studies led to analytical descriptions of the location of the leading swash edge as a function of space and time through ballistic motion equations and the shape of the swash lens during its cycle. Using the analytical solution of Carrier and Greenspan (1958), Baldock and Huntley (2002) and Jensen et al. (2003) described the run-up of standing long waves and the run-up of non-breaking solitary waves, respectively. While these investigations have shown that the analytical solution provides a good overall model for motion at the shoreline, the internal hydro- dynamics are less well described. For example, for real swash, flow reversal tends to occur later than predicted by the analytical solution. Also, the prediction of flow depth is unrealistically small in comparison with laboratory and field data (Baldock et al., 2005). Moreover, the swash prediction given by the analytical solution is hydrodynamically similar for all swash events, i.e., the internal flows are independent of the incident wave conditions at the seaward swash boundary after the initial bore collapse. Guard and Baldock (2007) presented numerical solutions for swash hydrodynamics for the case of breaking wave bores on a plane beach and found significant difference from the standard analytical solution of Shen and Meyer (1963). The results are important in terms of determining overwash flows, flow forces and sediment dynamics in the swash zone and show that the analytical solution gives a very shallow swash lens in comparison to the field measurements.

Brocchini and Peregrine (1996) proposed a flow model in which swash zone motions are described in terms of integral properties, i.e., spatially averaged over the swash width. Their solution is a 3D extension of that given by Carrier and Greenspan (1958) for the shallow water equations for a wave reflecting on an inclined plane beach. The integral model seems very valuable for numerical integration, as long as details of swash zone behavior are not required. When the full swash zone is included in a computation, it not only involves a larger domain of integration with a special boundary condition at the shoreline, but also frequently determines the maximum permitted time step. The changing position of the swash zone boundary and the longshore flow in the swash zone may be determined. Archetti and Brocchini (2002) used numerical analyses to assess the validity and potentialities of the integral swash zone model of Brocchini and Peregrine (1996), which was extended to include seabed friction effects. They concluded that the model was useful for two main purposes: (i) it can provide swash zone boundary conditions for both wave-resolving and wave-averaging models of nearshore flows; and (ii) an integral version of available sediment transport models, using as input conditions the integral hydrodynamic properties computed by means of the proposed model, might represent an improvement over currently used models as it would not require local values of seabed friction inside the swash zone. Alsina et al. (2005) presented a numerical model for sediment transport in the swash zone based on the classical ballistic motion for the shoreline described by Shen and Meyer (1963), and the hydrodynamic-kinematic model of Hughes and Baldock (2004). In the sediment transport module, the suspended load is calculated by a Lagrangian scheme, whilst the variation of suspended sediment concentration is computed with the advection–diffusion equation along particle trajectories.

Kobayashi et al. (1989) and Kobayashi and Poff (1994) developed a 1D depth-averaged nonlinear shallow water model, known as RBREAK, to predict the wave transformation in the surf and swash zones on gentle slopes. The numerical simulations covered a range of incident wave conditions between spilling and plunging waves. It has compared well with laboratory data in terms of time-averaged hydrodynamic parameters. Dodd (1998) developed an upwind finite volume scheme to solve the NLSWE for wave run-up and overtopping. The model tends to over-predict the water depth on the revetment. Asano

(1994) developed a numerical model to predict the flow characteristics in the swash zone for obliquely incident wave trains. In his study, the 2D shallow water equations were decoupled into independent equations each for on–off shore and for longshore motion. Hu et al. (2000) presented a high-resolution NLSWE model for wave propagating in the surf zone and wave overtopping of coastal structures. Although they indicated that the use of NLSWE to model wave overtopping is computationally efficient, model has not been tested for the up-rush of breaking wave and the detailed structure of wave breaking is ignored. Shiach et al. (2004) implemented a numerical model based on NLSWE to model a series of experiments examining violent wave overtopping of a near-vertical sloping structure. They pointed out that this model needs to extend to include dispersive terms for improving the model capability.

However, these models are unable to simulate details of the flow and turbulence fields necessary for predictions of sediment transport in the swash zone. Raubenheimer (2002) compared the observations and predictions of fluid velocities using nonlinear shallow water equations in the surf and swash zones and proposed that velocity skewness, up-rush and backwash velocities were over-predicted in the swash zone. Therefore, the applicability of these equations to sediment transport modeling in the swash zone had not been adequately investigated.

2.3.2 Boussinesq equations

Applications of the Boussinesq equations cover a variety of ocean and coastal problems of interest: from wind wave propagation in intermediate and shallow water depths to the study of tsunami wave propagation across large ocean basins (Sitanggang and Lynett, 2005). The governing equations consist of the 2D depth-integrated continuity equation and the horizontal momentum equation. In the dimensional form, the nonlinear Boussinesq equations are (Lynett et al., 2002)

$$\frac{\partial H}{\partial t} + \nabla(Hu_\alpha) - \mu^2\nabla\left\{H\left[\left(\frac{1}{6}(\eta^2 - \eta h + \eta^2) - \frac{1}{2}z_\alpha^2\right)\nabla S\right] = 0 \right. \\ \left. + \left(\frac{1}{2}(\eta - h) - z_\alpha\right)\nabla T\right\} = 0 \tag{2.5}$$

$$\frac{\partial u_\alpha}{\partial t}+\frac{1}{2}\nabla(u_\alpha\cdot u_\alpha)+g\nabla\eta+\frac{\partial}{\partial t}\left[\frac{1}{2}z_\alpha^2\nabla S+z_\alpha\nabla\mathrm{T}-\nabla\left(\frac{1}{2}\eta^2S+\eta T\right)\right]+$$
$$+\nabla\left[\frac{\partial\eta}{\partial t}(T+\eta S)+(z_\alpha-\eta)(u_\alpha\cdot\nabla)T+\frac{1}{2}(z_\alpha^2-\eta^2)(u_\alpha\cdot\nabla)S+\right.$$
$$\left.+\frac{1}{2}(T+\eta S)^2\right]=0 \qquad (2.6)$$

where $S=\nabla\cdot u_\alpha, T=\nabla\cdot(hu_\alpha)+\partial h/\partial t$; h is local water depth; z is free surface elevation; $H=h+\eta$, u_α is horizontal velocity vector and z_α is the reference depth.

Many researchers have modified the Boussinesq equations. Madsen et al. (1997a, b) discussed results from a Boussinesq-type wave model of swash oscillations induced by bichromatic wave groups and irregular waves on gentle beach slopes. They speculated that the shoreline motion consists of a significant low-frequency component at the group frequency and individual swash of the primary waves.

Sørensen et al. (2004) presented a numerical model for solving a set of extended time domain Boussinesq-type equations including the breaking zone and the swash zone. The model is based on the unstructured finite element technique. The model has been applied to a number of test cases, and found to compare well with laboratory measurements showed good agreement. The use of unstructured meshes offers the possibility of adapting the mesh resolution to the local physical scale and reduces the number of nodes in the spatial discretisation.

Kennedy et al. (2000) used a numerical model based on weakly nonlinear Boussinesq equations with a slot-type shoreline boundary. The model was further enhanced to improve numerical stability on steep beach slopes. Both infragravity and wind wave frequency swash are significant on steep beach slopes, while their relative dominance depends on the frequency of the incident waves. Karunarathna et al. (2005) studied swash motions on steep and gentle beaches based on numerical simulations and found swash excursions on any given slope were highest when individual bores from a partially saturated surf zone rode on top of low-frequency waves. A poor correlation was found

between swash excursion and the surf similarity parameter due to the involvement of infragravity wave energy in the swash.

The Boussinesq hydrodynamic model of Rakha et al. (1997) was coupled with a bed-load formulation to calculate changes across the beach profile. It showed reasonable agreement with observed elevation changes but under-predicted the observations. Karambas (2006) investigated numerically the sediment transport rate in the swash using a nonlinear wave model equation that incorporated infiltration/exfiltration effects. The model is based on the Boussinesq equations and is able to describe breaking and non-breaking wave propagation and run-up (Karambas and Koutitas, 2002). It was coupled with a porous flow model to account for infiltration/exfiltration effects on the sediment transport rate (Karambas, 2003). The authors suggest that their nonlinear model better describes sediment motion than other simplified approaches.

Pedrozo-Acuña et al.(2006) presented a numerical–empirical investigation of the processes that control sediment transport in the swash zone on steep gravel beaches. This was based on a sensitivity analysis of a sediment transport/profile model driven by a highly non-linear Boussinesq model that was compared to nearly full-scale measurements performed in a large wave flume. Pedrozo-Acuña et al. (2007) extended their analysis to compare these earlier results with those relating to a mixed sediment (gravel and sand) beach. The parametric sensitivity analysis incorporated a discussion of the effects of acceleration about which there is much debate. The sensitivity analysis suggests that fluid acceleration can contribute to the onshore movement of sediment that causes steepening of initially flat beach faces composed of coarse sediment. A complex balance of processes is responsible for the profile evolution of coarse-grained beaches with no single dominant process.

The accuracy of nearshore wave modeling using high-order Boussinesq-type models compared with typical order models was examined by Lynett (2006), who used the high-order two-layer model of Lynett and Liu (2004). For regular wave evolution over a bar, high-order models are in good agreement with experiments, correctly modeling the free

short waves behind the step. Under irregular wave conditions, it was shown that high-order non- linearity is important near the breaker line and the outer surf zone.

Fuhrman and Madsen (2008) simulated nonlinear wave run-up with a highly accurate Boussinesq-type model. A new variant of moving wet-dry boundary algorithms based on so-called extra- polating boundary techniques were utilized in 2D. Computed results involving the nonlinear run-up of periodic as well as transient waves on a sloping beach were considered in a single horizontal dimension, demonstrating excellent agreement with analytical solutions for both the free surface and horizontal velocity, with some discrepancies near the breaking point.

2.3.3 Navier-Stokes equations (NSE)

Another framework for numerical simulation of wave breaking and wave run-up/run-down is the implementation of models based on the Navier-Stokes equations (NSE). These equations have become more common with the improvement in computational techniques and facilities. The mass and momentum conservation equations are as follows:

$$\nabla \cdot \mathrm{V} = 0 \tag{2.7}$$

$$\frac{\partial V}{\partial t} + \nabla \cdot [VXV - v\nabla \mathrm{V} + \nabla \mathrm{P}] = F \tag{2.8}$$

$$\frac{\partial \varphi}{\partial t} + \nabla \cdot [V\varphi - \alpha \nabla \varphi] = S \tag{2.9}$$

where $\mathrm{P} = \mathrm{p}/\rho$ is the kinematic pressure; F is the body force; φ is a scalar quantity like concentration; α is the diffusivity; V the velocity vector; (VXV) stands for the tonsorial product of V, and S is a source term. Unlike the depth-averaged models, NSE are able to simulate details of the flow and turbulence fields, and vertical velocities can be determined directly.

For free-surface flow simulations, it is important to numerically describe the moving boundary. Several methods have been successfully incorporated in the NSE, e.g., the marker and cell (MAC) method (Park et al., 1999), the volume of fluid (VOF) method (Hirt and Nichols, 1981; Shen et al., 2004; Nielsen and Mayer, 2004), and the Arbitrary Lagrangian–Eulerian (ALE) method (Zhou and Stansby, 1999). These methods can deal with complicated free surfaces (e.g., breaking waves), yet their major drawback is that they require strict stability requirements and are computationally expensive. The free surface elevation can be calculated using either the free surface equation or kinematic free surface boundary condition.

To better simulate the flow and turbulence fields at the time of wave breaking, all hydrodynamic governing equations should be investigated. In principle, Direct Numerical Simulation (DNS) can be implemented for the simulation of wave breaking. However, computational demands are high for DNS methods. Considering turbulent flows with a high Reynolds number, such as wave breaking and wave run-up, since the turbulence oscillations should be computed in very fine time steps, the computational process would be time consuming. Also, it remains the case that even as computers become more and more powerful, DNS is still possible only with low Reynolds numbers in the foreseeable future. Another framework for numerical simulation of wave breaking is the implementation of models based on the Reynolds-Averaged Navier-Stokes (RANS) equations. In the RANS equations, the average motion of flow is described, and the effects of turbulence on the average flow are considered by the Reynolds stresses. In order to compute the Reynolds stresses and the turbulence characteristics, turbulence closure models are used. One of the solutions to the analysis of the NSE and the closure problem is the use of Boussinesq's eddy viscosity. The eddy viscosity is a characteristic defined by the local conditions of turbulence and hence is variable with time and location. The linear eddy viscosity model considers the relation between the Reynolds stresses and the rate of flow shape change. In order to acquire an approximation of local turbulence conditions and the related parameters, one can obtain and solve the equations governing the transformation of turbulence parameters k and ε ($k-\varepsilon$ closure models). Liu and Lin (1997) and Lin and Liu (1998a,b) developed a VOF-RANS model including a $k-\varepsilon$ turbulence closure scheme based on the non-linear Reynolds stress model to model the

turbulence levels in the surf zone. They implemented the model to study the propagation, shoaling and breaking in the nearshore, up-rush and backwash of wave train under breaking waves and discussed the turbulence mechanism in the surf zone. Their results yielded strong correspondence with free surface displacement and turbulence intensity from a laboratory experiments. Lin and Liu (1999) proposed a new general method for generating essentially any waves in a numerical wave tank based on the NSE by using designed mass source functions for the equation of mass conservation. The precision of this method in comparison with theories is very good. Although these models are able to forecast free surface displacement, velocity and turbulent fields, Elfrink and Baldock (2002) revealed that the resolution of these studies was too coarse to simulate the physical processes like wave boundary layer in the swash zone.

Drago and Iovenitti (1995) used the eddy viscosity approach, evaluating the eddy viscosity by a $k - l$ equation model (where is k the turbulent kinetic energy (TKE) and l represents the turbulence eddy scale length). Though the parameters incorporated in these models needed calibration, all researchers found their results corresponding to laboratory data of wave height growth in the surf zone. They acquired good results for spilling breakers but not for plunging. A key point in better comprehending the swash zone hydrodynamics is finding the accurate velocity distribution in the inner surf and swash zones.

Kothe et al.(1991) presented the RIPPLE computer program for modeling a transient, 2D, incompressible fluid flow. The free surface was computed using the VOF method. Puleo et al. (2002) studied breaking waves and run-up using RBREAK2 and RIPPLE models and showed the RIPPLE model more accurately displays wave breaking and wave run-up. However, the velocity estimates from the RIPPLE models how lag relationships as compared to the laboratory measurements.

Bradford (2000) compared the performance of the k model, linear $k - \varepsilon$ model and a Renormalized Group extension of the $k - \varepsilon$ model (RNG model) in the surf zone. It was found that all these models predict wave breaking far earlier than that observed in experiments, while also underestimating the undertows. Pope (2000) used a large eddy

simulation (LES) approach, which results from the calculation of stresses at the resolvable scales and modeling them at the sub-grid scales (SGS), since complex flows and adverse pressure gradients cause difficulties for the $k-\varepsilon$ turbulence closure schemes. Their model considered the swash zone but, like other surf zones studies, emphasized wave breaking processes. Christensen and Deigaard (2001) developed the numerical model to simulate the large-scale wave motions and turbulence induced by the breaking process. Their hydrodynamic model has been combined with a free surface model based on the surface markers method to simulate the flow field in breaking waves, where the large turbulent eddies have been simulated by the LES method and the small-scale turbulence is represented by a simple Smagorinsky sub-scale model. Wood et al. (2003) incorporated a VOF technique in a FLUENT code to model run- up of steep non-breaking waves. While this model qualitatively explained the development of the wave and the fluid velocity and acceleration during the up-rush, maximum run-up heights could not be obtained owing to limited accuracy of the VOF algorithm. Puleo et al. (2003) used LES to describe the turbulent eddy viscosity. In the model improvement, the effects of the LES were neglected due to the small grid scales used, but there was an excellent agreement for both sea surface and velocities in the inner surf and swash zones. Zhao et al. (2004) used the multi- scale turbulence model to simulate breaking waves and found good agreement with the wave set-up; however, the shape of the undertow profile does not seem to follow the measured profiles in all cases. The turbulence level near the breaking point was too high in all these studies. Christensen (2006) studied the LES of spilling and plunging breakers based on a model solving the NSE and found that the turbulence levels in general were too high compared with measurements, especially in plunging breakers. Also, the model requires a very long computational time and a fine grid to predict the details of hydrodynamics. Zhang and Liu (2008) investigated numerically the swash flows generated by bores using RANS model equations. Their results showed that the weak bore does not break, while the strong bore breaks as a plunger before it reaches the still-water shoreline. Chopakatla1 et al. (2008) used FLOW3D code to simulate 2D wave transformation and wave breaking and found good agreement between modeled and observed wave height, mean cross-shore flow and wave breaking variability. However, their model has been applied in the surf zone and not in the swash zone. Bakhtyar et al. (2007, 2009) presented a 2D numerical model for the

simulation of wave breaking, run-up and turbulence in the surf and swash zones. The numerical simulations covered a range of incident wave conditions between spilling and plunging waves. Their model provides a precise and efficient tool for the simulation of the flow field and wave transformations in the nearshore area, especially the swash zone.

Drake and Calantoni (2001) presented a discrete particle model (DPM) for sheet flow sediment transport in the nearshore zone. Due to memory requirements, they used only 1600 particles. Calantoni et al. (2006) used a VOF NSE solver (RIPPLE) to simulate inner surf zone and swash zone flow with a 3-s wave period and wave height of 0.14m on a planar, 1:10 sloping beach. In their work, RIPPLE was used to provide high-resolution predictions of the pressure gradient and fluid velocity in the horizontal and vertical directions, which were linked to a DPM. Coupling between RIPPLE and the DPM was one-way such that particle– particle and fluid–particle interactions in the DPM did not provide feedback to alter the flow predicted by RIPPLE. RIPPLE was derived from the mean 2D NSE, and the governing equation used for translational particle motion was (Madsen, 1991)

$$\rho_s V_s \frac{du_s}{dt} = V_s(\rho_s - \rho)g + V_s \nabla P + \frac{1}{2}\rho C_D A|u - u_s| + F_\phi \tag{2.10}$$

where ρ_s and ρ are, respectively, the particle and fluid densities; V_s is the particle volume; u_s and u are the particle and fluid velocities, respectively; P is the fluid pressure; C_D is the drag coefficient; A is the projected area of the spherical particle and F_ϕ represents the forces from inter-particle collisions. The numerical simulation showed a significant amount of sediment suspended locally under vortices that reached the bed. They demonstrated the model's ability to simulate sediment suspension events, while producing high-resolution predictions of motions of each sediment particle in the simulation.

In this chapter, we have discussed mainly process-based flow models. Models of sediment transport can also be more sophisticated than those based on a parametric relationship between sediment transport rate and flow parameters. The above review of the current research status demonstrates that cross- shore beach processes are intrinsically

nonlinear, unsteady and coupled. Therefore, in developing an improved modelling approach, the key challenge is to resolve the temporal and spatial phase variations of the fluid and sediment parameters.

Among the main processes, the least well-understood and most difficult to predict are the dynamics of near-bed sediment motions on beaches. This is partly due to the lack of detailed measurements of the flow and sediment transport in this region, and also constrained by the weakness of the conventional local transport modelling approach in calculating beach evolution. As shown by recent experimental and numerical studies (Ribberink and Al-salem, 1995; Davies et al., 1997; Dong and Zhang, 1999), the local models, whether they are based on the turbulent diffusion concept making use of an empirically derived bottom reference concentration as the boundary condition or the energetics concept, are too simplistic to truly represent the unsteady, nonlinear and two-phase nature of the sediment motions.

Two-phase flow modelling is capable of simulating fluid and sediment phases separately although the interphase coupling needs to be considered with some care. For the two-phase flow model, the governing equations of fluid phase are generally described in Eulerian form; whereas, the governing equations of the sediment phase can be written in either Eulerian or Lagrangian form. Furthermore, by coupling the governing equations of both phases, a system of the Eulerian equations or Euler–Lagrange coupled ones, is obtained to analyze the sediment-laden flow.

In the Euler–Euler coupling model, the sediment phase is treated as a continuum, which follows different constitutive laws to those for the clear water. In these models mainly the fluid–particle interaction of bed-load is taken in to account; whereas, the fundamental characteristics of the sediment motion cannot be expressed well. For this model, four essential equations for the modelling of the mass and momentum fields and the sediment are required. These equations are valid for both phases; therefore two additional equations are required for the mass and momentum exchanges between the phases (Crowe,2006). The general form of the equations for phase l is as follows (Crowe, 2006):

$$mass: \frac{\partial \rho_l}{\partial t} + \nabla(\rho_l v_l) = 0 \tag{2.11}$$

$$\sum_{i=1}^{2} [\rho_l (v_l - v_i) \cdot \hat{n}_l] = 0 \tag{2.12}$$

$$momentum: \frac{\partial (\rho_l v_l)}{\partial t} + \nabla \cdot (\rho_l v_l v_l) = \nabla \cdot T + \rho_l g \tag{2.13}$$

$$\sum_{i=1}^{2} [(\rho_l v_l (v_l - v_i) - T) \cdot \hat{n}_l] = m_i \, . \tag{2.14}$$

In these equations, $T = -PI + \tau$ is the stress tensor, P is the thermodynamic pressure, I is the unit tensor, g is the gravity acceleration, m_i is the source of momentum between the phases, $\hat{n}_l$ is the unit normal to phase l, v_i is the velocity of the common interface and v_l is the velocity vector of each phase.

Sheet flows widely occur in the swash zones (Hughes et al., 1997). Since the sheet flow in the swash zone is a highly concentrated combined flow of fluid and sediments under high shear stress, the dominating mechanism is very complicated. The location of the particles in the sheet flow is defined by the collision and the contact of the grains which differs from the usual turbulence-generated suspension (Asano, 1990). Sheet flow is an unsteady flow regime since it yields a vertical distribution and sporadic variations in the velocity and concentration fields. Over the last two decades, the two-phase flow technique has been used by several researchers to model sediment transport in sheet flow conditions. Asano (1990) presented a two-phase flow model based on the principles of the Kobayashi and Seo (1985) model in which the vertical velocity of particles was approximated by empirical relations. Ono et al. (1996) devised a model where the horizontal velocities of the fluid and the particles where considered to be identical. Dong and Zhang (1999) presented a two-phase flow model capable of simulating the fluid and particle motions in the sheet flows and oscillatory conditions. Their model is based on the principles of eddy viscosity model which is very restricted for modelling this complex flow. Hsu et al. (2003, 2004) applied a two-phase flow model to steady open channel

flow and unsteady oscillatory flow. Liu and Sato (2006) applied a two-phase flow model to simulate the net transport rate under combined wave/ current flow and various asymmetric sheet flow conditions. Their turbulent enclosure model was based on the parabolic eddy viscosity distributions.

To improve the Eulerian models deficiency, a granular material model can be employed to simulate the inter-particle collision mechanism of the bed-load transport, in Euler–Lagrange coupling model. A major development in modelling two-phase flow was use of Discrete Element Method (DEM) (Cundall and Strack, 1979) to simulate sediment transport during sheet flow in the swash zone as the motion of granular materials. In this approach, inter- particle collisions and forces can be quantified in great detail. Gotoh and Sakai (1997) performed pioneering work on simulation of the bed-load from the viewpoint of granular material dynamics. In this model, the Lagrangian sediment behaviour is modelled based on the DEM. Yeganeh-Bakhtiary et al. (2000) presented an Euler–Lagrange coupling two-phase flow model to bed-load transport under high bottom shear. Although the predominant particle–particle interaction is described in their model, the sediment particle has been traced as moving disk in the 2D coordinates, which has different character than real sand grains.

To date, the existing two-phase flow approaches are focusing on describing time-dependent and time-averaged concentration distributions. For practical purposes, the magnitude and direction of net sand transport are more attractive and important. This review shows that none of the existing numerical models can describe the wave breaking satisfactorily and none of them studied the surf and swash zones mutually and comprehensively. In particular, none has been verified carefully for both the turbulent and mean velocity field.

CHAPTER 3

THE IH-2VOF NUMERICAL MODEL.

Numerical models of fluid/wave-structure interactions are increasingly becoming a viable tool in furthering our understanding of the complicated phenomena that govern the hydraulic response of breakwaters, including effects of permeability (Losada, 2003). These include Lagrangian models with particle-based approaches such as the Moving Particle Semi-Implicit method (Koshizuka et al., 2004) and Smooth Particle Hydrodynamics (Dalrymple et al., 2009). For reasons ranging from computational efficiency to an accurate representation of the physical processes, Reynold Averaged Navier Stokes-Volume Of Fluid (Rans-Vof) models have become an attractive choice to model wave interactions with both solid as well as porous structures. This kind of models solves the 2DV Reynolds Average Navier–Stokes (RANS) equations, based on the decomposition of the instantaneous velocity and pressure fields, into mean, and turbulent components and the free surface movement is tracked by the Volume of Fluid (VOF) method.

Lin and Liu (1998), based on a previously existing model called RIPPLE (Kothe et al., 1991; originally designed to provide a solution of two-dimensional versions of the Navier-Stokes equations in a vertical plane with a free surface), presented COBRAS (Cornell Breaking Waves and Structures) for simulating breaking waves and wave interaction with coastal structures. The model has been under a continuous development process based on an extensive validation procedure, carried out for low-crested structures (Garcia et al., 2004, Losada et al., 2005; Lara et al., 2006a), wave breaking on permeable slopes (Lara et al., 2006b), surf zone hydrodynamics on natural beaches (Torres-Freyermuth et al., 2010) and overtopping on rubble mound breakwaters and low-mound breakwaters (Losada et al., 2008; Lara et al., 2008). In this work, a modified and improved version of COBRAS, named IH-2VOF (Lara et al., 2011), is used.

In this chapter a synthetic description of the main features of the IH-2VOF (mathematical formulation, boundary and initial conditions, computational domain, wave generation method, free surface tracking method and numerical resolution) are presented. The description is mostly based in Liu and Lin (1997), Lin and Liu (1998), Hsu et al. (2002) and Lara et al. (2011).

3.1 Governing equations in the fluid domain: the Reynolds Averaged Navier-Stokes (RANS) equations

The governing Reynolds Averaged Navier-Stokes (RANS) equations of the IH-2VOF model represent the general principle of mass and momentum conservation. Due to the less assumption involved in the governing equations, RANS models are able to simulate the frequency dispersive nature of gravity waves in deep waters as well as the nonlinear wave transformations in shallow waters over a sloping bottom. With the inclusion of a proper turbulent model, they are able to describe difficult wave problems such as breaking waves, energy transfer between wave components, wave-current interactions and wave-structure interactions. The refined information on the velocity, pressure and turbulence field makes them suitable to study surf zone hydrodynamics. Wave breaking and its evolution along the surf zone are directly solved without any imposed forcing.

The IH-2VOF model solves the two-dimensional Reynolds Averaged Navier-Stokes (RANS) equations base on the assumption that in a turbulent flow the instantaneous velocity field u_i and the pressure field p can be split in two parts, the ensemble-averaged (mean) velocity and pressure components, $\bar{u}_i$ and $\bar{p}$, and the turbulent velocity and pressure fluctuations, $u_i^{'}$ and $p^{'}$:

$$u_i = \bar{u}_i + u_i^{'}, \qquad p = \bar{p} + p^{'} \tag{3.1}$$

where $i = 1, 2$ for a bidimensional flow.
Applying the former decomposition to the Navier-Stokes equations and assuming incompressible fluid, the RANS equations are derived:

$$\frac{\partial \bar{u}_i}{\partial x_i} = 0 \tag{3.2}$$

$$\frac{\partial \bar{u}_i}{\partial t} + \bar{u}_j \frac{\partial \bar{u}_i}{\partial x_j} = -\frac{1}{\rho}\frac{\partial \bar{p}}{\partial x_i} + g_i + \frac{1}{\rho}\frac{\partial \bar{\tau}_{ij}}{\partial x_i} \tag{3.3}$$

where g_i is the i-th component of the gravitational acceleration, ρ is the density of the fluid, $\bar{\tau}_{ij}$ is the sum of the viscous stress tensor of the mean flow and the Reynolds stress tensor. For a Newtonian fluid

$$\bar{\tau}_{ij} = 2\mu\bar{\sigma}_{ij} + R_{ij} \tag{3.4}$$

where μ is the molecular viscosity, R_{ij} is the Reynolds stress tensor and $\bar{\sigma}_{ij}$ is the rate of strain tensor of mean flow given by:

$$\bar{\sigma}_{ij} = \frac{1}{2}\left(\frac{\partial \bar{u}_i}{\partial x_j} + \frac{\partial \bar{u}_j}{\partial x_i}\right). \tag{3.5}$$

The Reynolds stress term R_{ij} in the momentum equation represents the influence of turbulent fluctuations on the mean flow

$$R_{ij} = \rho\left(\bar{u}_i'\bar{u}_j'\right). \tag{3.6}$$

In the IH-2VOF model, the Reynolds stress tensor is assumed to be related to the strain rate of the mean flow through the algebraic non-linear $k - \varepsilon$ model (Shih *et al.*, 1996; Lin and Liu, 1998):

$$\overline{u_i}'\overline{u_j}' = \frac{2}{3}k\delta_{ij} - C_d\frac{k^2}{\varepsilon}\left(\frac{\partial \overline{u}_i}{\partial x_j} + \frac{\partial \overline{u}_j}{\partial x_i}\right) + \\ -\frac{k^3}{\varepsilon^2}\begin{bmatrix} C_1\left(\frac{\partial \overline{u}_i}{\partial x_l}\frac{\partial \overline{u}_l}{\partial x_i} + \frac{\partial \overline{u}_j}{\partial x_l}\frac{\partial \overline{u}_l}{\partial x_i} - \frac{2}{3}\frac{\partial \overline{u}_l}{\partial x_k}\frac{\partial \overline{u}_k}{\partial x_l}\delta_{ij}\right) + \\ +C_2\left(\frac{\partial \overline{u}_i}{\partial x_k}\frac{\partial \overline{u}_j}{\partial x_k} - \frac{1}{3}\frac{\partial \overline{u}_l}{\partial x_k}\frac{\partial \overline{u}_k}{\partial x_l}\delta_{ij}\right) + \\ +C_3\left(\frac{\partial \overline{u}_k}{\partial x_i}\frac{\partial \overline{u}_k}{\partial x_j} - \frac{1}{3}\frac{\partial \overline{u}_l}{\partial x_k}\frac{\partial \overline{u}_l}{\partial x_k}\delta_{ij}\right) \end{bmatrix} \tag{3.7}$$

in which C_d, C_1, C_2 and C_3 are empirical coefficients, δ_{ij} is the Kronecker delta, k is the turbulent kinetic energy and ε is the dissipation rate of turbulent kinetic energy.

$$k = \frac{1}{2}\left(\overline{u_i}'\overline{u_j}'\right) \tag{3.8}$$

$$\varepsilon = v\left(\frac{\partial \overline{u_i}'}{\partial x_j}\right)^2 \tag{3.9}$$

where v is the molecular kinematic viscosity.
The condition:

$$C_1 = C_2 = C_3 = 0 \tag{3.10}$$

in equation (3.7) leads to the conventional linear (isotropic) eddy viscosity model for the Reynolds stresses closure:

$$\overline{u_i}'\overline{u_j}' = -2v_t\bar{\sigma}_{ij} + \frac{2}{3}k\delta_{ij} \tag{3.11}$$

with v_i is the eddy viscosity expressed as:

$$v_t = C_d\left(\frac{k^2}{\varepsilon}\right). \tag{3.12}$$

Contrary to the conventional eddy viscosity models as expressed by equation (3.12), valid for the description of isotropic-eddy-viscosity turbulent flows, the non-linear Reynolds stress model implemented in the IH-2VOF model and expressed by equation (3.7) can be applied to general anisotropic turbulent flows.

The values for the coefficients C_2 and C_3 are obtained from experimental results on turbulent shear flow by Champagne *et al.* (1970). A value for C_d is proposed by Rodi (1980). Finally, the C_1 coefficient is deduced from the assumption by Shih *et al.* (1996): $C_1 = 2C_3$. The whole set of coefficients are summarized as follows:

$$C_d = 0.09\,, C_1 = 0.0054\,, C_2 = -0.0171\,, C_3 = 0.0027. \tag{3.13}$$

However, considering constant values for these coefficients may lead under some extreme circumstances to inconsistent physical situations in equation (3.7), such as negative turbulence energy or infinite non-linear contributions. Hence, modified expressions for the empirical coefficients have been implemented in the IH-2VOF model:

$$\begin{aligned} C_d &= \frac{2}{3}\left(\frac{1}{7.4 + S_{max}}\right), C_1 = \frac{1}{185.2 + D_{max}^2}, \\ C_2 &= -\frac{1}{58.5 + D_{max}^2}, C_3 = \frac{1}{370.4 + D_{max}^2} \end{aligned} \tag{3.14}$$

where

$$S_{max} = \frac{k}{\varepsilon} max\left[\left|\frac{\partial \overline{u}_\iota}{\partial x_i}\right|\right] \quad D_{max} = \frac{k}{\varepsilon} max\left[\left|\frac{\partial \overline{u}_\iota}{\partial x_i}\right|\right] \tag{3.15}$$

all coefficients take their originally proposed values when S_{max} and D_{max} are zero.
The governing equation for k and ε are (Rodi, 1980; Lin and Liu, 1998):

$$\frac{\partial k}{\partial t} + \overline{u}_j \frac{\partial k}{\partial x_j} = \frac{\partial}{\partial x_j}\left[\left(\frac{v_t}{\sigma_k} + v\right)\frac{\partial k}{\partial x_j}\right] - \left(\overline{u}_i^{'}\overline{u}_j^{'}\right)\frac{\partial \overline{u}_i}{\partial u_j} - \varepsilon \tag{3.16}$$

$$\frac{\partial \varepsilon}{\partial t} + \bar{u}_j \frac{\partial \varepsilon}{\partial x_j} = \frac{\partial}{\partial x_j}\left[\left(\frac{v_t}{\sigma_\varepsilon} + v\right)\frac{\partial \varepsilon}{\partial x_j}\right] + C_{1\varepsilon}\frac{\varepsilon}{k} v_t \left(\frac{\partial \bar{u}_i}{\partial x_j} + \frac{\partial \bar{u}_j}{\partial x_i}\right)\frac{\partial \bar{u}_i}{\partial x_j} - C_{2\varepsilon}\frac{\varepsilon^2}{k} \tag{3.17}$$

In equation (3.16), the first and second terms of the left-hand side represent convection and diffusion respectively. The second and third terms of the right-hand side represent production and dissipation of kinetic turbulent energy respectively. The Reynolds stress only appears as the turbulence production term. The empirical coefficients in equation (3.17) have been determined by performing many simple experiments. Recommended values for these coefficients are (Rodi, 1980; Lin and Liu, 1998):

$$C_{1\varepsilon} = 1.44\,, C_{2\varepsilon} = 1.92\,, \sigma_k = 1.0\,, \sigma_\varepsilon = 1.3 \tag{3.18}$$

As outlined by Lin and Liu (1998), the RANS equations along with the k −ε transport equations using the former values for the empirical coefficients were found to adequately simulate many complex turbulent flows.

3.2 Initial and boundary conditions

For the initial time and at boundary of the spatial domain, additional constrains or equations are required by the physics of the problem.

3.2.1 Initial conditions

The model considers as initial conditions for the mean flow in the whole domain still water with no wave or current motion, i.e. zero velocities and hydrostatic pressure. For the turbulence field, due to the fact that the production term in the k equation is proportional to k itself, no turbulence will be produced if the initial value for k is zero. Therefore, a finite but very small value of k is imposed. This initial value ("seed") for the turbulence energy produces a numerical perturbation:

$$k = \frac{1}{2}u_t^2 \tag{3.19}$$

with $u_t = \delta c_i$, where c_i is the wave celerity in the generation zone and δ is a constant equal to 0.0025 (Lin, 1998).

For the turbulent dissipation rate, the model considers the following expression:

$$\varepsilon = C_d \frac{k^2}{v_t} \tag{3.20}$$

where $v_t = \xi v$ and ξ is a constant equal to 0.1 (Lin, 1998).

Variation of the δ and ξ values were found to have a negligible effect on the final results of the computation (Lin, 1998). Numerical simulations performed by Lin and Liu (1998) showed that the influence of δ on the flow conditions reduces to a slight delay in the initiation of breaking for smaller values of δ.

3.2.2 Boundary conditions

As regards boundary conditions, it is possible identify three different cases.

1. *Solid boundaries*

At the solid boundaries two types of conditions for the mean flow can be considered:

$$No\ slip: \overline{u_n} = 0, \overline{u_\tau} = 0 \tag{3.21}$$

$$Free\ slip: \overline{u_n} = 0, \frac{\partial \overline{u_\tau}}{\partial n} = 0 \tag{3.22}$$

with n and τ are the directions normal and parallel to the boundary respectively.

In the case of turbulent flows, the model considers a log-law distribution for the mean tangential velocity in the turbulent boundary layer:

$$\frac{\partial \bar{u}}{\partial y} = \frac{u_*}{\kappa y} \tag{3.23}$$

where κ is the von Karman constant ($\kappa = 0.41$), y is the distance from the solid domain and u_* is a friction velocity. Integrating equation (3.23) and assuming that production and dissipation are equivalent in the boundary layer leads to the following equations for k and ε at the solid boundary:

$$k = \frac{u_*}{\sqrt{C_d}} \tag{3.24}$$

$$\varepsilon = \frac{u_*^3}{\kappa y}. \tag{3.25}$$

The value of u_* is obtained from the values of mean flow:

$$\varepsilon = \upsilon \frac{\partial \bar{u}}{\partial y}\Big|_{y=0} \tag{3.26}$$

1. *Free surface*

The application of an appropriate boundary condition at the mean free surface in turbulent flows is quite complex as the mean free surface is not clearly defined (Brocchini and Peregrine, 1995; Lin and Liu, 1997; Lin and Liu, 1998). In the IH-2VOF model, the mean density fluctuations near the free surface due to mixing and air intrusion are neglected, and similarly to situations of laminar flow, the zero stress and zero pressure conditions are imposed at the free surface:

$$\bar{p} = 0, \qquad \frac{\partial \overline{u_\tau}}{\partial n} = 0\,. \tag{3.27}$$

For the turbulent field, the zero-gradient boundary condition is applied for both k and ε on the free surface:

$$\frac{\partial k}{\partial n} = 0, \qquad \frac{\partial \varepsilon}{\partial n} = 0 \tag{3.28}$$

with n the unit normal on the free surface, based on the assumption of no turbulence exchange between water and air.

With respect to the lateral conditions, the model can consider a closed boundary, regarded as a solid boundary, in which the conditions described before are applied, or allow the flow to go out of the domain, as an open boundary or radiation condition.

1. *Open boundaries*

The open boundary condition in the IH-2VOF model is expressed as:

$$\frac{\partial \phi}{\partial t} + c_0 \frac{\partial \phi}{\partial x} = 0 \tag{3.29}$$

where ϕ represents the variable to be evaluated ($\bar{u}, \bar{v}, k, \varepsilon, etc.$) and c_o the wave celerity at the considered position expressed as

$$c_0 = \sqrt{g(d+a)} \tag{3.30}$$

for long waves, and

$$c_0 = \sqrt{\frac{g\lambda}{2\pi} tanh\left(\frac{2\pi}{\lambda}(d+a)\right)} \tag{3.31}$$

for short waves, where a is the wave amplitude, d is the water depth and λ is the wave length for this depth. This radiation condition has been checked to adequately reproduce theoretical results for nonlinear waves at indefinite and intermediate depths ($H/d < 0.3$). More details on the boundary conditions can be found in Rodi (1980) and Liu and Lin (1997).

3.3 Free surface tracking trough the volume of fluid (VOF) method

In the COBRAS model, the free surface is tracked using the Volume Of Fluid (VOF) method. The method does not consist in pursuiting the exact location of the free surface, but in identifying the free surface location tracking the density change in each cell. The model identifies the different cell types: empty (E), surface (S) or interior (I) cells depending on the value of the VOF function defined as follows:

$$F = \frac{\rho}{\rho_f} \tag{3.32}$$

where

$$\rho = \frac{\rho_f V_f}{V_f + V_a} \tag{3.33}$$

being ρ_f the fluid density, V_f the volume of fluid in the cell and V_a the volume of air in the cell. Interior, empty and surface cells are defined as the $F = 1$, $F = 0$ and $F > 0$ cell respectively. Cell types are shown in the following figure.

The introduction of the VOF function in the equation of mass conservation yields the transport equation for $F(x, y, t)$:

$$\rho(x, y, t) = F(x, y, t)\rho_f \tag{3.34}$$

$$\frac{\partial F}{\partial t} + \frac{\partial}{\partial x}(\bar{u}F) + \frac{\partial}{\partial y}(\bar{v}F) = 0\,, \tag{3.35}$$

Hirt and Nichols (1981) developed an algorithm to avoid errors in the convection of F. Their method consists in evaluating F gradients in both directions in order to identify the free surface location. Lin (1998) improved the algorithm with a new method that solves the problem of the $F > 1$ cells. A detailed analysis of the VOF method can be found in Hirt and Nichols (1981) and Lin (1998).

3.4 Partial cell treatment

The IH-2VOF model allows the introduction in the computational domain of solid boundaries of arbitrary shape, using a partial cell treatment. This method avoids the potential spurious reflection at solid boundaries defined as sawtooth-shape surfaces fitting the cell boundaries (Lemos, 1992). It consists in modelling the solid object as a special case of fluid with an infinite density, introducing openness functions at the cell centre and at the cell faces. At the cell centre, θ_c is defined as the ratio of space not occupied by the solid object (thus open to the fluid) to the whole cell area. On the cell faces, θ_r (θ_t) is defined as the length open to the fluid to the whole length of the right (top) boundary. Therefore, similar to the VOF free surface tracking method, the model can identify whether the cell corresponds to the solid object or obstacle (O), the fluid (air)-solid boundary (FA-O) or the fluid (air) domain (FA). In order to solve the magnitudes defined at the right face of the cells, the parameter identifies whether the cell face belongs to a solid boundary or not. The only difference between the VOF function and the openness functions is that the former is time-varying and the latter are not.

3.5 Governing equations for the flow in porous media (VARANS equations)

To make the fluid/porous structure interaction modelling easier, a volume-averaging process has been applied to the RANS and the k and ε equations. The flow in porous media is obtained in the IH-2VOF model through the resolution of the Volume-Averaged Navier-Stokes (VARANS) equations. These equations are derived by integration of the RANS equations over a control volume. The size of the averaging volume is chosen much larger than the characteristic pore size but much smaller than the characteristic length scale of the flow, i.e. the scale of the spatial variation of the physical variables in the fluid domain.

The mathematical process of volume averaging of a certain quantity “a” is defined by the following expression:

$$\langle a \rangle = \frac{1}{V_f} \int_{V_f} a \, dV \tag{3.36}$$

where "⟨ ⟩" denotes the intrinsic volume averaging, V is the total averaging volume, V_f is the volume in V which is occupied by the fluid phase and $\langle a \rangle$ is the averaged magnitude. The intrinsic averaging operator defined by equation (3.36) can be related to the Darcy's volume averaging operator defined as follows:

$$\langle a \rangle_D = \frac{1}{V} \int_{V_f} a \, dV \tag{3.37}$$

through the simple relationship:

$$\langle a \rangle_D = n \langle a \rangle \tag{3.38}$$

where

$$n = \frac{V_f}{V} \tag{3.39}$$

is the porosity and is assumed for simplicity to be a constant in the present model. In terms of velocity, $\langle a \rangle_D$ would be the seepage velocity and $\langle a \rangle$ the filtration velocity. Hereafter, unless specified, volume averaging will be understood as intrinsic volume averaging, as defined by expression (3.36).

To quantify the flow within the porous medium, the pore Reynolds number is defined as:

$$Re_p = \frac{D_{50}|U|}{\upsilon} \tag{3.40}$$

where Re_p is the equivalent mean diameter of the porous material, υ is the fluid kinematic viscosity and $|U|$ is a typical velocity scale around the pore.

The VARANS equations are obtained by applying the intrinsic volume average to the RANS equations. The ensemble averaged velocity of the RANS equations is assumed to be:

$$\bar{u}_i = \langle \bar{u}_i \rangle + \bar{u}_i'' \tag{3.41}$$

where $\langle \bar{u}_i \rangle$ is the ensemble-volume averaged velocity field and $\bar{u}_i''$ is the fluctuation with respect to volume averaging, in other words the residual velocity field between ensemble-volume averaging and ensemble averaging.

Applying this decomposition to the equations of continuity (3.2) and momentum conservation (3.3), we obtain:

$$\frac{\partial \langle \bar{u}_i \rangle}{\partial x_i} = 0 \tag{3.42}$$

$$\begin{aligned} \frac{\partial \langle \bar{u}_i \rangle}{\partial t} + \frac{\partial \langle \bar{u}_i \rangle \langle \bar{u}_j \rangle}{\partial x_j} = -\frac{1}{\rho}\frac{\partial \langle \bar{P} \rangle}{\partial x_i} - \frac{\partial \langle \bar{u}_i' \bar{u}_j' \rangle}{\partial x_j} + \frac{1}{\rho}\frac{\partial \langle \bar{\tau}_{ij} \rangle}{\partial x_i} + g_i - \frac{\partial \langle \bar{u}_i'' \bar{u}_j'' \rangle}{\partial x_j} + \\ + \frac{1}{V_f}\int_{A_{int}} \left[-\bar{u}_i' \bar{u}_j' - \frac{\bar{P}}{\rho}\delta_{ij} + \frac{\bar{\tau}_{ij}}{\rho} \right] n_j dA \end{aligned} \tag{3.43}$$

A_{int} is the total fluid-solid interface and n_j the *j*th component of the unit vector pointing normally outward from the fluid to solid phase. The last term in equation (3.43) accounts for the jump at the interface and represents the interfacial momentum transfer between the fluid phase and the solid skeleton. This term is crucial in the modelling of the flow in porous media. The previous term in the equation (3.44) is the residual stress due to volume averaging: it results from the volume averaging of the convective term $\bar{u}_i \bar{u}_j$ as:

$$\langle \bar{u}_i \bar{u}_j \rangle = \langle \bar{u}_i \rangle \langle \bar{u}_j \rangle + \langle \bar{u}_i'' \bar{u}_j'' \rangle \tag{3.44}$$

analogously to the stress term in the Reynolds decomposition of the product $u_i u_j$. These last two terms are unclosed and need to be modelled. Inside the porous media, these

terms are modelled collectively using the Forchheimer's relationship with the inclusion of unsteady effects (Liu et al., 1999a):

$$-\frac{\partial\langle\bar{u}_i''\bar{u}_j''\rangle}{\partial x_j}+\frac{1}{V_f}\int_{A_{int}}\left[-\bar{u}_i'\bar{u}_j'-\frac{\bar{P}}{\rho}\delta_{ij}+\frac{\bar{\tau}_{ij}}{\rho}\right]n_j dA = \\ =-\left[\frac{\alpha v(1-n)^2}{n^2 D_{50}^2}\langle\bar{u}_i\rangle+\frac{\beta(1-n)}{nD_{50}}\sqrt{\langle\bar{u}_1\rangle^2+\langle\bar{u}_2\rangle^2}\langle\bar{u}_i\rangle+c_A\frac{\partial\langle\bar{u}_i\rangle}{\partial t}\right] \tag{3.45}$$

where C_A is the added mass coefficient and α and β two empirical coefficients associated with the linear and nonlinear drag force respectively. The third term of the right-hand side of equation (3.45) accounts for the inertial effects.

The precise descriptions of the C_A, α and β coefficients are still not fully understood. They depend a priori on the pore Reynolds number and flow directions. In their recent study of wave motions and turbulent flows in front of a composite breakwater using the COBRAS model, Hsu *et al.* (2002) propose the following values for these coefficients, based on previous works by van Gent (1994), Liu *et al.* (1999a) or Nield and Bejan (1999):

$$c_A = 0.34\frac{1-n}{n}\,,\alpha = 200\,,\beta = 1.1 \tag{3.46}$$

Finally, given the former closure expression for the residual stress term due to volume averaging and the momentum transfer at the interface of equation (3.38), the complete VARANS equations (3.38) and (3.39) can be rewritten as:

$$\frac{\partial\langle\overline{u_i}\rangle}{\partial x_i}=0 \tag{3.47}$$

$$\frac{\partial\langle\overline{u_i}\rangle}{\partial t}+\frac{\langle\overline{u_j}\rangle}{1+c_A}\frac{\partial\langle\overline{u_i}\rangle}{\partial x_j}=\frac{1}{\rho(1+c_A)}\left[-\frac{\partial\langle\bar{P}\rangle}{\partial x_i}-\frac{\partial\rho\langle\overline{u_i'u_j'}\rangle}{\partial x_j}+\frac{\partial\langle\overline{\tau_{ij}}\rangle}{\partial x_j}+\rho g_i\right] \\ -\frac{1}{1+c_A}\left[\frac{\alpha v(1-n)^2}{n^2 D_{50}^2}\langle\overline{u_i}\rangle+\frac{\beta(1-n)}{nD_{50}^2}\sqrt{\langle\overline{u_i}\rangle^2+\langle\overline{u_2}\rangle^2}\langle\overline{u_i}\rangle\right] \tag{3.48}$$

In the free fluid region, i.e. with $n = 1$ and $C_A = 0$, the VARANS equations obviously return to the original RANS equations.

The volume-averaged Reynolds stress is closed using an assumption similar to Shih *et al.* (1996):

$$\begin{aligned}\langle \bar{u}_i' \bar{u}_j' \rangle = \frac{2}{3}\langle k \rangle \delta_{ij} - \langle v_t \rangle \left(\frac{\partial \bar{u}_i}{\partial x_j} + \frac{\partial \bar{u}_j}{\partial x_i} \right) + \\ -\frac{\langle k \rangle^3}{\langle \varepsilon \rangle^2} \left[\begin{array}{c} C_1 \left(\frac{\partial \bar{u}_i}{\partial x_l}\frac{\partial \bar{u}_l}{\partial x_j} + \frac{\partial \bar{u}_j}{\partial x_l}\frac{\partial \bar{u}_l}{\partial x_i} - \frac{2}{3}\frac{\partial \bar{u}_l}{\partial x_k}\frac{\partial \bar{u}_k}{\partial x_l}\delta_{ij} \right) + \\ + C_2 \left(\frac{\partial \bar{u}_i}{\partial x_k}\frac{\partial \bar{u}_j}{\partial x_k} - \frac{1}{3}\frac{\partial \bar{u}_l}{\partial x_k}\frac{\partial \bar{u}_l}{\partial x_k}\delta_{ij} \right) + \\ + C_3 \left(\frac{\partial \bar{u}_k}{\partial x_i}\frac{\partial \bar{u}_k}{\partial x_j} - \frac{1}{3}\frac{\partial \bar{u}_l}{\partial x_k}\frac{\partial \bar{u}_l}{\partial x_k}\delta_{ij} \right) \end{array} \right]\end{aligned} \tag{3.49}$$

where $\langle v_t \rangle$ is the volume-averaged eddy viscosity, $\langle k \rangle$ is the volume-averaged turbulence kinetic energy and $\langle \varepsilon \rangle$ is the volume-averaged turbulent dissipation rate.

Similarly to the $k - \varepsilon$ model, the volume-averaged eddy viscosity is expressed as:

$$\langle v_t \rangle = C_D \frac{\langle k \rangle^2}{\langle \varepsilon \rangle} \tag{3.50}$$

with C_D a coefficient depending on the local strain rate.

Equations (3.49) and (3.50) can be regarded as the result of a first-order approximation of the volume averaging of the original nonlinear eddy viscosity model expressed by equations (3.7) and (3.12). Any higher correlations related to the volume averaging process have been ignored.

The governing equations for the turbulence in the porous media can be similarly obtained by taking the volume-averaged turbulent kinetic energy $\langle k \rangle$ and its dissipation rate $\langle \varepsilon \rangle$ can then be written as:

$$\frac{\partial\langle k\rangle}{\partial t}+\frac{\partial\langle k\rangle\langle\bar{u}_j\rangle}{\partial x_j}=\langle\overline{u_i'u_i'}\rangle\frac{\partial\langle\bar{u}_i\rangle}{\partial x_j}+\frac{\partial}{\partial x_j}\left[\left(v+\frac{v_t}{\sigma_k}\right)\frac{\partial\langle k\rangle}{\partial x_j}\right]-\langle\varepsilon\rangle+ \\ +\langle\overline{u_i'u_j'}''\frac{\partial\bar{u}_i''}{\partial x_j}\rangle+\frac{1}{V_f}\int_{A_{int}}\left(v+\frac{v_t}{\sigma_k}\right)\frac{\partial k}{\partial x_j}n_j dA-\frac{\partial}{\partial x_j}\langle\bar{u}_j''k''\rangle \tag{3.51}$$

$$\frac{\partial\langle\varepsilon\rangle}{\partial t}+\frac{\partial\langle\varepsilon\rangle\langle\bar{u}_j\rangle}{\partial x_j}=C_{1\varepsilon}\frac{\langle\varepsilon\rangle}{\langle k\rangle}\langle\overline{u_i'u_j'}\rangle\frac{\partial\langle\bar{u}_i\rangle}{\partial x_j}+\frac{\partial}{\partial x_j}\left[\left(v+\frac{v_t}{\sigma_k}\right)\frac{\partial\langle\varepsilon\rangle}{\partial x_j}\right]+ \\ -C_{2\varepsilon}\frac{\langle\varepsilon\rangle^2}{\langle k\rangle}+C_{1\varepsilon}\frac{\langle\varepsilon\rangle}{\langle k\rangle}\langle\overline{u_i'u_j'}''\frac{\partial\bar{u}_i''}{\partial x_j}\rangle+\frac{1}{V_f}\int_{A_{int}}\left(v+\frac{v_t}{\sigma_k}\right)\frac{\partial\varepsilon}{\partial x_j}n_j dA-\frac{\partial}{\partial x_j}\langle\bar{u}_j''\varepsilon''\rangle \tag{3.52}$$

in which the following decompositions related to volume averaging have been assumed:

$$k=\langle k\rangle+k'' \tag{3.53}$$

$$\varepsilon=\langle\varepsilon\rangle+\varepsilon'' \tag{3.54}$$

$$\overline{u_i'u_j'}=\overline{\langle u_i'u_j'\rangle}+\overline{u_i'u_j'}'' \tag{3.55}$$

In both (3.51) and (3.52) equations, the fourth term on the right-hand side represents an additional source term due to volume averaging. These terms describe the effects of turbulence at a scale smaller than the volume-averaging scale, for instance the turbulence generation in the wake region around the solid skeleton in high pore Reynolds number conditions.

The fifth term represents the interfacial exchange of turbulence and is viewed as an additional source or sink of turbulence due to the presence of solid materials. These two terms are modelled collectively according to Nakayama and Kuwahara (1999), substituted by ε_∞ in the ⟨k⟩ transport equations and by the term:

$$C_{2\infty}\frac{\varepsilon_\infty^2}{k_\infty} \tag{3.56}$$

in the $\langle\varepsilon\rangle$ transport equation.

The last term on both $\langle k \rangle$ and $\langle \varepsilon \rangle$ equations is the additional diffusion term due to the volume averaging and can be combined with the existing diffusion terms in the $\langle k \rangle$ and $\langle \varepsilon \rangle$ equations. The overall effect can be modelled by adjusting the values of σ_k and σ_ε. However, due to a lack of experimental information, the values of σ_k and σ_ε are kept unchanged in the IH-2VOF model. Therefore, the equations (3.51) and (3.52) can be rewritten as:

$$\frac{\partial \langle k \rangle}{\partial t} + \frac{\partial \langle k \rangle \langle \bar{u}_j \rangle}{\partial x_j} = \langle \overline{u_i' u_j'} \rangle \frac{\partial \langle \bar{u}_i \rangle}{\partial x_j} + \frac{\partial}{\partial x_j}\left[\left(\nu + \frac{\nu_t}{\sigma_k}\right)\frac{\partial \langle k \rangle}{\partial x_j}\right] - \langle \varepsilon \rangle + \varepsilon_\infty \tag{3.57}$$

$$\begin{aligned}\frac{\partial \langle \varepsilon \rangle}{\partial t} + \frac{\partial \langle \varepsilon \rangle \langle \bar{u}_j \rangle}{\partial x_j} = {} & C_{1\varepsilon}\frac{\langle \varepsilon \rangle}{\langle k \rangle}\langle \overline{u_i' u_j'} \rangle \frac{\partial \langle \bar{u}_i \rangle}{\partial x_j} + \frac{\partial}{\partial x_j}\left[\left(\nu + \frac{\nu_t}{\sigma_k}\right)\frac{\partial \langle \varepsilon \rangle}{\partial x_j}\right] + \\ & - C_{2\varepsilon}\frac{\langle \varepsilon \rangle^2}{\langle k \rangle} + C_{2\varepsilon}\frac{\varepsilon_\infty^2}{k_\infty}\end{aligned} \tag{3.58}$$

The values of the closure coefficients, due to a lack of information here again, are kept the same as those proposed by the standard $k - \varepsilon$ model equations and the nonlinear eddy viscosity model.

Expressions for the small-scale turbulence terms k_∞ and ε_∞ have been proposed by Nakayama and Kuwahara (1999), resulting from numerical simulations of flow passing an array of square rods for pore Reynolds numbers between 10^5 and 10^7. The work by Nakayama and Kuwahara (1999) for this range of Re_p values led to the following closure forms:

$$\varepsilon_\infty = 39.0\ (1-n)^{2.5} n^2 (\langle \overline{u_1} \rangle^2 + \langle \overline{u_2} \rangle^2)^{1.5} \frac{1}{D_{50}} \tag{3.59}$$

$$k_\infty = 3.7(1-n) n^{1.5} (\langle \overline{u_1} \rangle^2 + \langle \overline{u_2} \rangle^2)\,. \tag{3.60}$$

To date, no work on the effect of the small-scale turbulence and expressions of ε_∞ and k_∞ for small values of the pore Reynolds number is available in the literature. However, it can be verified that the small-scale turbulence represented by equations (3.59) and (3.60)

has a negligible effect when the pore Reynolds number becomes small. Equations (3.59) and (3.60) are thus expected to be still applicable in low pore Reynolds number conditions.

3.6 Schematics of computational domain

The computational domain in the IH-2VOF model is discretised in rectangular cells as sketched in Figure 3.1. The computing mesh can be divided into sub-mesh regions, which allows a variable cells spacing: a finer grid can be defined for the representation of specific study zones.

The different quantities in each of the cells are defined as follows: all scalar quantities, i.e. pressure (P), turbulent kinetic energy (k), dissipation rate (ε), VOF function (F) and the hereafter specified openness function (θ_c) are defined in the centre of the cells. The vector and vector-related quantities, i.e. the components of the mean velocity $\bar{u}$ and the additional openness functions (θ_r and θ_t), are defined on the cell faces as shown in Figure 3.2. The x-component of the mean velocity is defined at the left face, the y-component of the mean velocity is defined at the top face.

The IH-2VOF model allows the introduction in the computational domain of solid boundaries of arbitrary shape, using a partial cell treatment. This method avoids the potential spurious reflection at solid boundaries defined as sawtooth-shape surface4s fitting the cell boundaries (Lemos, 1992). It consists in modelling the solid object as a special case of fluid with an infinite density, introducing openness functions at the cell centre and at the cell faces. At the cell centre,

Figure 3.1 and Figure 3.2 illustrate the definition of the different cell types based on the information of the VOF function and openness functions.

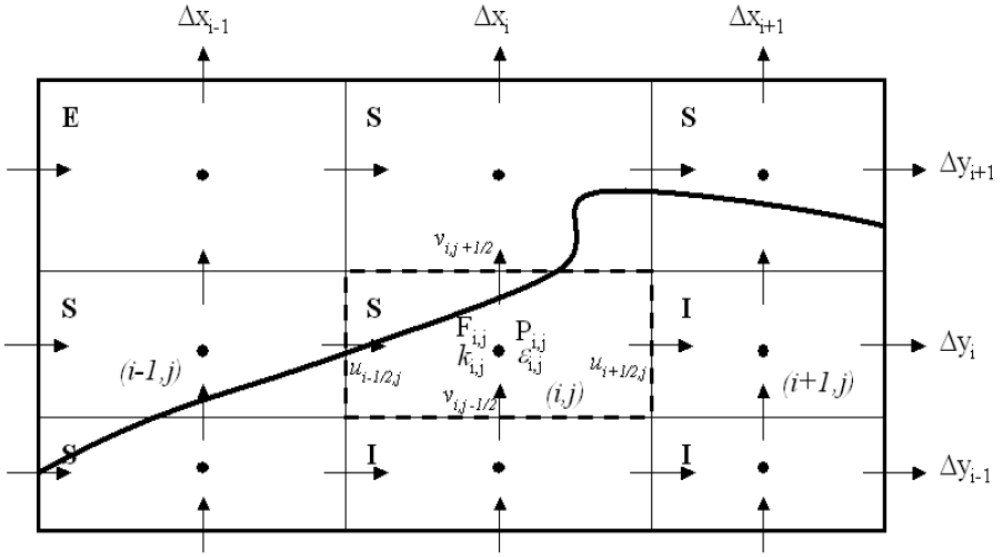

Figure 3.1. Schematics of computational domain with the different cell types on the information of the VOF function and definition of the computed magnitudes (Lin, 1998).

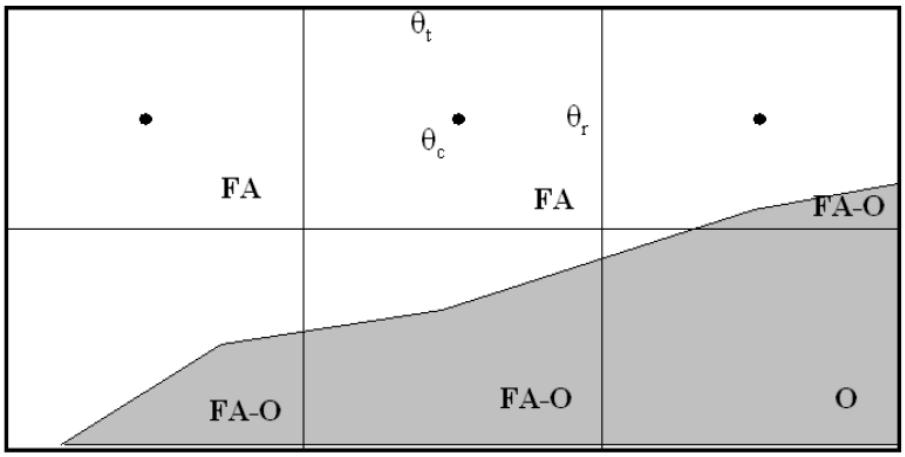

Figure 3.2. Schematics of solid boundaries definition through the partial cell treatment (Lin, 1998).

3.7 Numerical resolution

The finite difference method is used to solve the governing equations. A grid of points at fixed locations is introduced in the spatial domain and the dependent variables are initially defined and subsequently computed at these points. Approximate expressions for derivatives appearing in the governing equations are found. These approximations are formed using differences of dependent variables over finite space and time intervals. The time step used in advancement of the evolution equations is the time scale of the averaging of original Navier-Stokes equations. Then a system of algebraic equations that approximates the governing partial differential equations is constructed.

The RANS equations are solved using the finite differences two-step projection method.

1. The first step is to introduce an intermediate velocity $\widetilde{u}_i$ that does not satisfy the continuity equation

$$\frac{\tilde{u}_i - u_i^n}{\Delta t} = -u_j^n \frac{\partial u_j^n}{\partial x_j} + g_i + \frac{\partial \tau_{ij}}{\partial x_j} \tag{3.61}$$

   where the superscripts denote the time level. This is the forward time difference equation of the momentum equation in the RANS equation without the pressure gradient term.
2. The second step is to project the intermediate velocity into a divergence free plane to obtain the final velocity

$$\frac{u_i^{n+1} - \tilde{u}_i}{\Delta t} = -\frac{1}{\rho^n} \frac{\partial p^{n+1}}{\partial x_i} \tag{3.62}$$

$$\frac{\partial u_i^{n+1}}{\partial x_i} = 0. \tag{3.63}$$

Taking the sum of the first and second step equations, the RANS momentum equations are satisfied with the pressure gradient being evaluated at the (n+1)-th time level

$$\frac{\tilde{u}_i^{n+1} - u_i^n}{\Delta t} + u_j^n \frac{\partial u_j^n}{\partial x_j} = -\frac{1}{\rho}\frac{\partial p^{n+1}}{\partial x_i} + g_i + \frac{\partial \tau_{ij}^n}{\partial x_j} \tag{3.64}$$

Taking the divergence of second step equation and applying continuity equation yields we have

$$\frac{\partial}{\partial x_i}\left(\frac{1}{\rho^n}\frac{\partial p^{n+1}}{\partial x_i}\right) = \frac{1}{\Delta t}\frac{\partial \tilde{u}_i}{\partial x_i} \tag{3.65}$$

which is called the Poisson Pressure Equation (PPE).

In the two-step projection method, the spatial derivations of the velocity components and the pressure field need to be expressed in finite-difference forms. The convection terms are discretised by the combination of the central difference method and upwind method. The combination of both is aimed at preventing their respective drawbacks of significant numerical damping and numerical instability. A weighting factor is introduced in the spatial derivative discretisation expressions in order to adjust the influence of each one of the two schemes in the computation and to obtain stable and accurate solutions. Only the central difference method is employed to discretise the pressure gradient terms and stress terms.

Similarly to the Reynolds equations, the $k - \varepsilon$ equations are solved by discretising the convective terms with the combined central difference and upwind methods.

The detailed implementation of the numerical model can be found in Liu and Lin (1997) and Lin (1998).

3.8 Resolution procedure

The basic resolution procedure of IH-2VOF to update the field variables at a given time step is summarised as follows:

- compute intermediate velocities $\tilde{u}_i$ using equation (3.51);
- apply the boundary conditions at the free surface and definition of the source function;
- compute the pressure value from equation (3.55);
- obtain the final values of velocities from equation (3.54);
- apply newly the boundary conditions at the free surface;
- update VOF function values;
- apply the boundary conditions at the newly fluid cells (empty at the previous time step) consecutively to VOF function updating.

CHAPTER 4

REPRESENTATION OF THE WAVE OVERTOPPING PROCESS.

The goal of this chapter is to analyze the overtopping process, in particular the layer thicknesses and the velocities of the flow over the crest of a emerged/submerged structures, in order to extend the existing theoretical approaches and provide criteria for the design of structures close to mean sea level or overwashed. This analysis was carried out on a numerical database derived by running the Rans-Vof code (IH-2VOF) in presence of impermeable structures characterized by different slopes and freeboard.

In particular, we chose to investigate seadikes in order to compere our work with the extensive work that it is possible find in literature (Schüttrumpf, 2001; Van Gent,2002; Schüttrumpf and Van Gent, 2003; Schuttrumpf and Oumeraci, 2005; Eurotop, 2007). However, the analysis can be extended to other types of coastal defences, for example, breakwaters that are more frequently present in Italian coasts.

Figure 4.1. Severe wave overtopping at the Samphire Hoe seawall, UK (CLASH project, www.clash-eu.org, 2001).

4.1 Design criteria for coastal defences structures

Different types of coastal structures are built worldwide to protect low lying areas from coastal flooding in coastal areas. Steep sea walls (slopes between 1:1.5 and 1:3) are used in some coastal areas which are in general constructed of concrete, blocks or placed stones. In Belgium, the Netherlands, Denmark, Germany and Poland, smooth seadikes (slopes between 1:3 and 1:7) which are built of clay and sand are preferred. Thus, the failure mechanisms of seadikes and seawalls differ significantly and different design methods are used. At present, wave overtopping is the most important design criteria for seawalls, while wave run-up still represents the most important design criteria for seadikes.

The history of seadike design has recorded many heavy storm surges and dike breaches up to the middle of the last century. The heavy storm surges in the Netherlands in 1953, and in Germany in 1962, with many fatalities in both countries, have significantly changed the design philosophy of seadikes. The design of seadikes was essentially based on the highest water level ever observed plus a safety margin during previous centuries. This procedure was replaced by a deterministic design philosophy as a consequence of the storm surges in 1953 and 1962 and the crest level of seadikes are now determined using a design water level with specific exceedance frequencies and the corresponding wave run-up height. Nevertheless, a design water level with specific exceedance frequencies and the corresponding wave run-up height are subject to large uncertainties, so that wave overtopping cannot always be avoided. Therefore, wave overtopping has to be considered for the design of seadikes and a deterministic design philosophy should be replaced by a probabilistic design philosophy for seadikes in the future.

Probabilistic design requires an improved under-standing of all physical processes responsible for dike failures. One important aspect is the determination of those wave overtopping parameters which are relevant for infiltration, erosion and consequently dike failures. The present design of seadikes does not consider the interaction of wave overtopping flow and soil mechanic properties. The design water level is calculated from measured water levels and extrapolated by fitted statistical distributions including an exceedance frequency which is specified as a function of the local conditions and the

vulnerability of the flood prone area. The corresponding wave run-up height is calculated from the incoming wave parameters at the design water level. Important investigations about the determination of the wave run-up height were carried out by Wassing (1957), Hunt (1959), Battjes (1974), Owen (1980), Tautenhain (1981) and Van der Meer and Janssen (1995). The wave run-up and wave overtopping formulas by Van der Meer and Janssen (1995) have now been adopted in many national recommendations for the design of seadikes.

As mentioned above, a wave run-up height and an average overtopping rate are inappropriate parameters for the determination of infiltration and erosion. Therefore, all processes relevant to the wave overtopping flow parameters have to be determined. These processes must be understood to describe the overtopping flow which will provide the hydraulic boundary conditions for erosion, infiltration and slip failure analysis.

Empirical equations describing wave overtopping processes in terms of incident wave conditions, structure geometry, and crest freeboard have been developed based on small- and large-scale physical model tests of common structure geometries. In particular, in literature it is possible to find some theories that describe flow depths and velocities over the dike crest for emerged conditions, whereas for zero freeboard and submerged conditions a theoretical approach that allows to know the flow characteristics over the dike crest is not available. Economic constraints and environmental and aesthetic impact often impose more practical levee designs having lower crown elevations with the associated risk that some wave/surge overtopping will occur during extreme events. In addition, the increase of frequency and intensity of storms, combined with the uncertainties related to extreme events and climate change, pose serious challenges in the long term design of defences from coastal flooding. Therefore it is more likely that in the next future many dikes will operate for longer times at lower crest freeboards, i.e. close to mean sea level or even overwashed. For design purposes, accurate estimates of the statistics of overtopping waves in terms of flow depths, duration and especially velocities for a set of climate conditions are needed and have to be combined with consolidated criteria for identifying tolerable overtopping threshold. At the moment, the information

available for overwashed dikes can be derived from the (limited) set of tests performed by Hughes et al. (2012).

As regards emerged structures, recently formulae have been derived for maximum flow depth and velocities on the crest and inner slope. These formulae are based on the difference fictive wave run-up and the crest freeboard. This is a good measure to determine the flow depths and velocities on the dike. These formulae have been calibrated by two independent physical model test programs in different wave flumes. One of the studies has been carried out by Schüttrumpf in Germany (Schüttrumpf, 2001). He performed large and small scale model tests and determined the empirical coefficients. The other study has been carried out on small scale by Van Gent (Van Gent, 2002). He calibrated the formulae and determined the empirical coefficients as well. When these two studies are compared appears a large difference. In fact, the empirical coefficient of the flow depth equation was determined to be a factor 2.2 higher by Schuttrumpf than by Van Gent, whereas they agreed about the empirical coefficient of the velocity equation. They collectively wrote a paper (Schuttrumpf and Van Gent, 2003) and found the test set-up as primary cause for the discrepancy in the flow depth coefficient (see also Schuttrumpf and Oumeraci, 2005). Bosman et al. (2008) used the raw data of Schüttrumpf (2001) and van Gent (2002) and analyzed them using a new approach. He shown that the outer slope is of great importance in the flow depths and velocities on the crest. Whereas Schüttrumpf performed his tests on a dike model with an outer slope of 1:6, Van Gent used a dike model with outer slope of 1:4. Bosman verified that the empirical coefficients are depending on the outer slope steepness. Therefore formulae for maximum flow depth and velocity were adapted: the coefficients are written as a function of the outer slope angle.

Moreover full-scale testing of dike landward slopes under a given sequence of overtopping wave volumes through the Wave Overtopping Simulator (Van der Meer et al., 2006, 2008, 2009) significantly extended our knowledge of landward-side dike resiliency (Hoffmans et al., 2008; Van der Meer et al., 2010). However, the WOS requires an accurate estimate of the wave overtopping volumes and related statistics to

allow in cascade an accurate reproduction of flow depths and velocities on landward slopes.

All formulae reported in this chapter are proposed by Eurotop manual (2007) which summarizes all the existing theories.

4.2 Overtopping over a seadikes

Wave overtopping occurs if the crest level of the dike is lower than the highest wave run-up level. In that case, the freeboard R_c, defined as the vertical difference between the still water level (wd) and the crest height, becomes important. Hence wave overtopping depends on the freeboard R_c and increases for decreasing freeboard height R_c.

An exact mathematical description of the wave run-up and wave overtopping process for coastal dikes is not possible due to the stochastic nature of wave breaking and wave run-up and the various factors influencing the wave run-up and wave overtopping process. Therefore, wave run-up and wave overtopping for coastal dikes are mainly determined by empirical formulas derived from experimental investigation. The influence of roughness elements, wave wall, berms, etc. is taken into account by introducing influence factors.

4.2.1 Wave overtopping discharge

In the case of emerged structures (**positive freeboard**) the Eurotop 2007 suggests the following distinction (Figure 4.2).

- **Probabilistic design and prediction or comparison of measurements** $(\boldsymbol{\xi_{m-1,0} < 5})$**.** The following overtopping formulae for breaking and non-breaking waves describes the average overtopping discharge:

$$\frac{q}{\sqrt{gH_{m0}^3}} = \frac{0.067}{\sqrt{tan\alpha}}\gamma_b \cdot \xi_{m-1,0} \cdot exp\left(-4.75\frac{R_c}{\xi_{m-1,0} \cdot H_{m0} \cdot \gamma_b \cdot \gamma_f \cdot \gamma_\beta \cdot \gamma_v}\right) \quad (4.1)$$

with a maximum of:

$$\frac{q}{\sqrt{gH_{m0}^3}} = 0.2 \cdot exp\left(-2.6 \frac{R_c}{H_{m0} \cdot \gamma_f \cdot \gamma_\beta}\right) \quad (4.2)$$

The reliability of Equations 4.1 and 4.2 are described by taking the coefficients 4.75 and 2.6 as normally distributed stochastic parameters with means of 4.75 and 2.6 and standard deviations $\sigma = 0.5$ and 0.35 respectively. For probabilistic calculations Equations 4.1 and 4.2 should be taken together with these stochastic coefficients. For predictions of measurements or comparison with measurements also Equations 4.1 and 4.2 should be taken with, for instance, 5% upper and lower exceedance curves.

- **Deterministic design or safety assessment $(\xi_{m-1,0} < 5)$.** For deterministic calculation in design or safety assessment it is strongly recommended to increase the average discharge by about one standard deviation. Thus, Equation 4.3 should be used for deterministic calculations in design and safety assessment:

$$\frac{q}{\sqrt{gH_{m0}^3}} = \frac{0.067}{\sqrt{tan\alpha}} \gamma_b \cdot \xi_{m-1,0} \cdot exp\left(-4.3 \frac{R_c}{\xi_{m-1,0} \cdot H_{m0} \cdot \gamma_b \cdot \gamma_f \cdot \gamma_\beta \cdot \gamma_v}\right) \quad (4.3)$$

with a maximum of:

$$\frac{q}{\sqrt{gH_{m0}^3}} = 0.2 \cdot exp\left(-2.3 \frac{R_c}{H_{m0} \cdot \gamma_f \cdot \gamma_\beta}\right). \quad (4.4)$$

In the case of very heavy breaking on a shallow foreshore the wave spectrum is often transformed in a flat spectrum with no significant peak. In that case, long waves are present and influencing the breaker parameter $\xi_{m-1,0}$. Other wave overtopping formulae are recommended for shallow and very shallow foreshores to avoid a large underestimation of wave overtopping by using formulae 4.1, 4.2,

4.3 and 4.4. Since those formulae are valid for breaker parameters $\xi_{m-1,0} < 5$ a linear interpolation is recommended for breaker parameters $5 < \xi_{m-1,0} < 7$.

- **Deterministic design or safety assessment $(\xi_{m-1,0} < 5)$.** The following formula is recommended including a safety margin for deterministic design and safety assessment.

$$\frac{q}{\sqrt{gH_{m0}^3}} = 0.21 \cdot exp\left[-\frac{R_c}{\gamma_f \cdot \gamma_\beta \cdot H_{m0} \cdot (0.33 + 0.022 \cdot \xi_{m-1,0})}\right]. \qquad (4.5)$$

- **Probabilistic design and prediction or comparison of measurements $(\xi_{m-1,0} > 7)$.** The following formula was derived from measurements with a mean of -0.92 and a standard deviation of 0.24:

$$\frac{q}{\sqrt{gH_{m0}^3}} = 10^c \cdot exp\left[-\frac{R_c}{\gamma_f \cdot \gamma_\beta \cdot H_{m0} \cdot (0.33 + 0.022 \cdot \xi_{m-1,0})}\right]. \qquad (4.6)$$

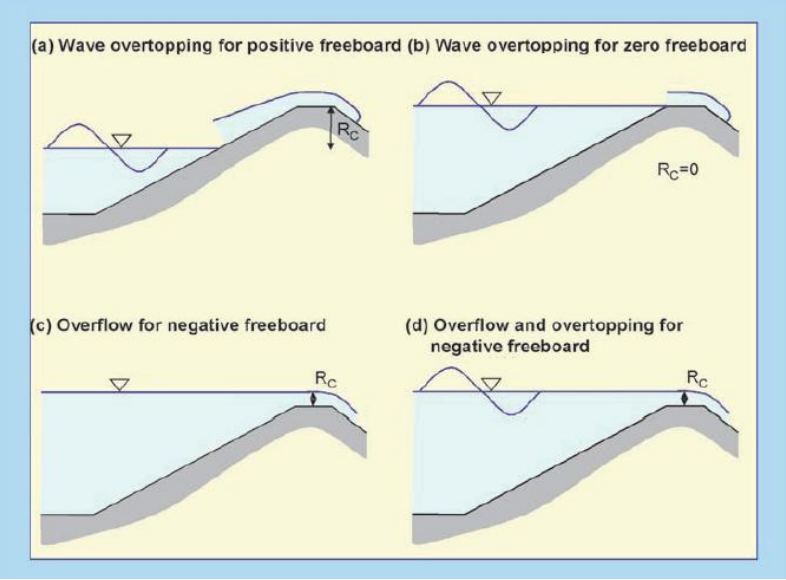

Figure 4.2. Wave overtopping and overflow for positive, zero and negative freeboard (by Eurotop 2007).

Wave overtopping for **zero freeboard** (Figure 4.2) becomes important if a dike is overtopping resistant (for example a low dike of asphalt) and the water level comes close to the crest. Schüttrumpf (2001) performed model tests for different straight and smooth slopes in between 1:3 and 2:6 to investigate wave overtopping for zero freeboard and derived the following formula ($\sigma' = 0.14$), which should be used for probabilistic design and prediction and comparison of measurements:

$$\frac{q}{\sqrt{gH_{m0}^3}} = 0.0537 \cdot \xi_{m-1,0} \qquad for\ \xi_{m-1,0} < 2 \tag{4.7}$$

$$\frac{q}{\sqrt{gH_{m0}^3}} = 0.0136 - \frac{0.226}{\xi_{m-1,0}^3} \qquad for\ \xi_{m-1,0} \geq 2 \tag{4.8}$$

If the water level is higher than the dike crest, large overtopping quantities overflow/overtop the structure. In this situation, the amount of water flowing to the landward side of the structure is composed by a part which can be attributed to overflow (q_s) and a part which can be attributed to overtopping (q_w). The part of overflowing water can be calculated by the well known formula for a broad crested structure:

$$q_s = 0.6 \cdot \sqrt{g \cdot |-R_c^3|} \tag{4.9}$$

where R_c is the (negative) relative crest height and $-R_c$ is the overflow depth.
The effect of wave overtopping (q_w) is accounted for by the overtopping discharge at zero freeboard ($R_c = 0$) in Equations 4.7 and 4.8 as a first guess. The effect of combined wave run-up and wave overtopping is given by the superposition of overflow and wave overtopping as a rough approximation for $\xi_{m-1,0} < 2$:

$$q = q_s + q_w = 0.6 \cdot \sqrt{g \cdot |-R_c^3|} + 0.0537 \cdot \xi_{m-1,0} \cdot \sqrt{g \cdot H_{m0}^3} \tag{4.10}$$

4.2.2 Overtopping flow velocities and overtopping flow depth

Average overtopping rates are not appropriate to describe the interaction between the overtopping flow and the failure mechanisms (infiltration and erosion) of a clay dike. Therefore, research was carried out recently in small and large scale model tests to investigate the overtopping flow velocities and the related flow depth on the seaward slope, the dike crest and the landward slope. Results are summarized in Schüttrumpf and Van Gent (2003). Empirical and theoretical functions were derived and verified by experimental data in small and large scale. These parameters are required as boundary conditions for geotechnical investigations, such as required for the analysis of erosion, infiltration and sliding.

The parameters of overtopping flow velocities and overtopping flow depth will be described separately for the seaward slope, the dike crest and the landward slope. Here only the considerations about the flow over the dike crest is reported.

The overtopping tongue arrives as a very turbulent flow at the dike crest. Maximum flow depth and overtopping velocities were measured in this overtopping phase over the crest. The overtopping flow separation occurs at the middle and at the dike surface at the front edge of the crest. No flow separation occurs at the middle and at the rear edge of the crest. In the second overtopping phase, the overtopping flow has crossed the crest. Less air in the overtopping flow but the flow itself is still very turbulent with waves in flow direction and normal to flow direction. In the third overtopping phase, a second peak arrives at the crest resulting in nearly the same flow depth as the first peak. In the fourth overtopping phase, the air has disappeared from the overtopping flow and both overtopping velocity and flow depth are decreasing. Finally, the overtopping flow nearly stops on the dike crest for small overtopping flow depths. Few air is in the overtopping water. At the end of this phase, the overtopping water on the dike crest starts flowing seaward.

The overtopping flow depth on the dike crest depends on the width of the crest B and the co-ordinate on the crest x_c (Figure 4.4) and the flow depth decreases due to the fact that

the overtopping water is deformed. Thus, the decrease of the overtopping flow depth over the dike crest can be described by an exponential function:

$$\frac{h_c(x_c)}{h_c(x_c = 0)} = exp\left(-c_2 \frac{x_c}{B_c}\right) \tag{4.11}$$

with h_c the overtopping flow depth on the dike crest, x_c the horizontal coordinate on the dike crest with $x_c = 0$ at the beginning of the dike crest, c_2 the dimensional coefficient $= 0.89$ for TMA spectra ($\sigma' = 0.06$) and 1.11 for natural wave spectra ($\sigma' = 0.09$), and B_c the width of the dike crest (for $B_c = 2$ to 3 m in prototype scale).

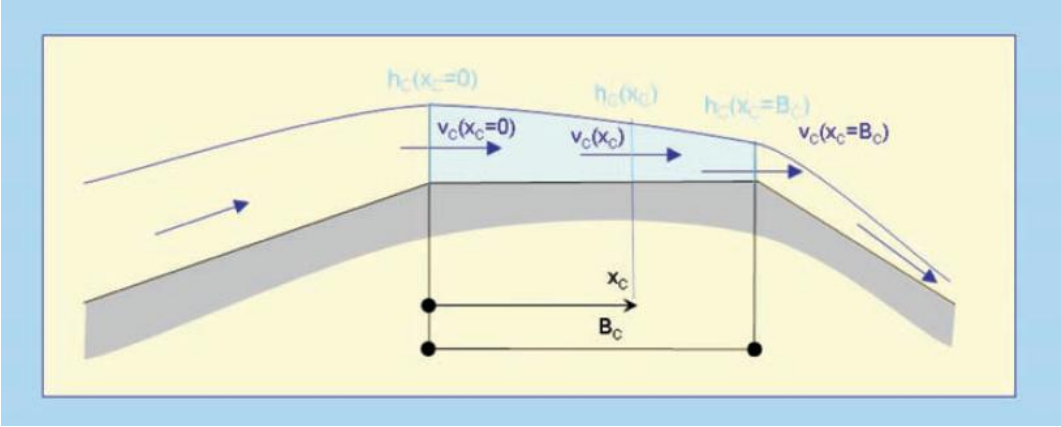

Figure 4.3. Definition sketch for overtopping flow parameters on the dike crest (by Eurotop 2007).

A theoretical function for overtopping flow velocities on the dike crest has been developed by using the simplifies Navier-Stokes equations and the following assumptions: the dike crest is horizontal; velocities vertical to the dike slope can be neglected; the pressure term is almost constant over the dike crest; viscous effects in flow direction are small; bottom friction is constant over the dike crest.

The following formula was derived from the Navier-Stokes equations and verified by small and large scale model tests (Figure 4.4):

$$v_c = v_{c(x_c=0)} exp\left(-\frac{x_c \cdot f}{2 \cdot h_c}\right) \tag{4.12}$$

with v_c the overtopping flow velocity on the dike crest; $v_{c(x_c=0)}$ the overtopping flow velocity at the beginning of the dike crest ($x_c = 0$); x_c the coordinate along the dike crest; f the friction coefficient; and h_c the flow depth at x_c. From the Equation (4.12) it is obviously that the overtopping flow velocity decreases from the beginning to the end of the dike crest and this decrease is more marked for increasing surface roughness (Figure 4.6). But for flow depth larger than about 0.1 m and dike crest widths around 2-3 m, the flow depth and velocity hardly change over the crest.

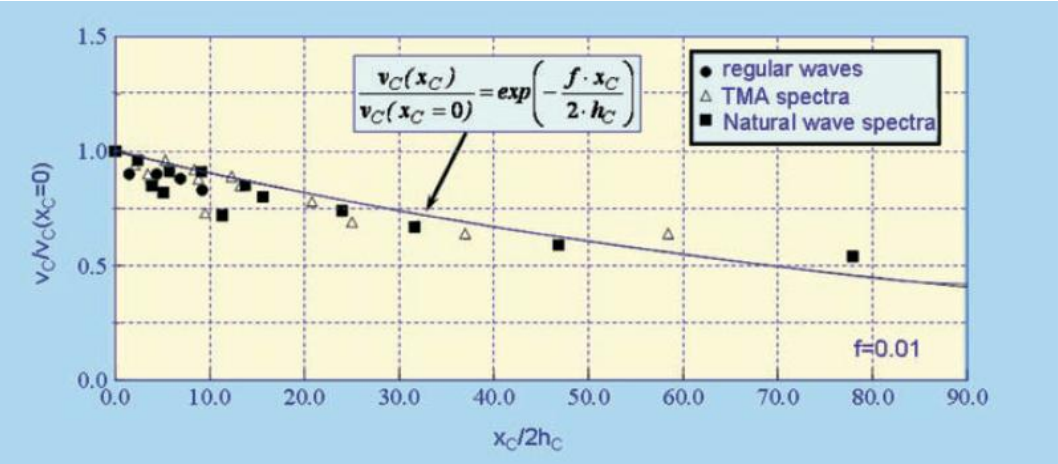

Figure 4.4. Overtopping flow velocity data vs overtopping flow velocity formulae (by Eurotop 2007).

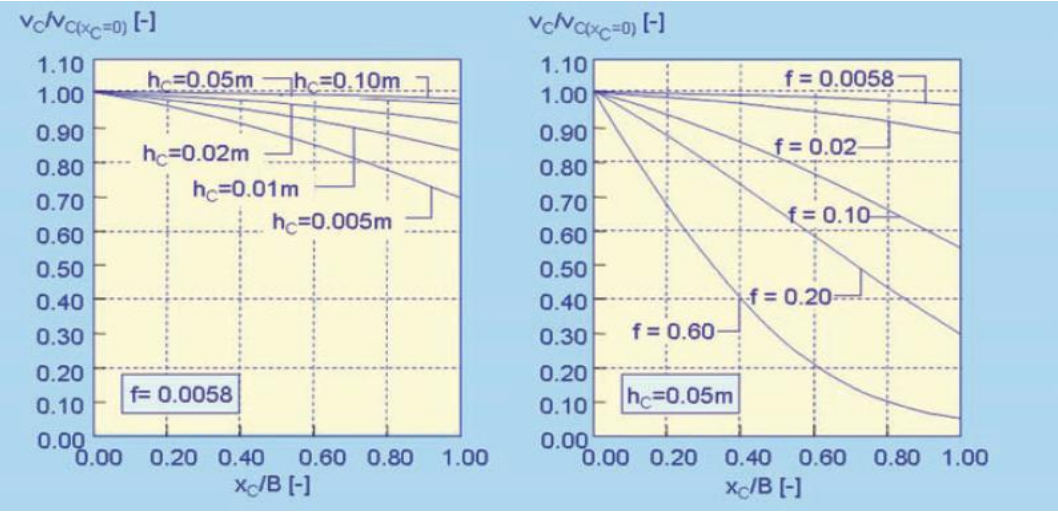

Figure 4.5. Left side: influence of overtopping flow depth on overtopping flow velocity; right side: influence of bottom friction on overtopping flow velocity (by Eurotop 2007)

4.3 The numerical database

The simulations were performed in 1:10 scale in a numerical flume 52.3 m long and 1.5 m deep under irregular waves with different significant wave heights H_s and peak period T_p characterized by Jonswap spectrum (Table 4.1).

Table 4.1. Characteristics of simulated tests.

	α_{off} = 1:4 ; α_{in} = 1:3				α_{off} = 1:4 ; α_{in} = 1:2				α_{off} = 1:6 ; α_{in} = 1:3			
R_c/H_s	**Tests**	H_s [m]	T_p [s]	wd [m]	**Tests**	H_s [m]	T_p [s]	wd [m]	**Tests**	H_s [m]	T_p [s]	wd [m]
-1	**T1A**	0.10	1.74	0.80	**T1E**	0.10	1.74	0.80	**T1I**	0.10	1.74	0.80
	T2A		2.18		**T2E**		2.18		**T2I**		2.18	
	T3A		1.58		**T3E**		1.58		**T3I**		1.58	
	T4A		2.25		**T4E**		2.25		**T4I**		2.25	
	T5A	0.20	3.29	0.90	**T5E**	0.20	3.29	0.90	**T5I**	0.20	3.29	0.90
	T5A		3.10		**T5E**		3.10		**T5I**		3.10	
	T7A		4.36		**T7E**		4.36		**T7I**		4.36	
	T8A		4.43		**T8E**		4.43		**T8I**		4.43	
0	**T9B**	0.10	1.74	0.70	**T9F**	0.10	1.74	0.70	**T9J**	0.10	1.74	0.70
	T10B		2.18		**T10F**		2.18		**T10J**		2.18	
	T11B		1.58		**T11F**		1.58		**T11J**		1.58	
	T12B		2.25		**T12F**		2.25		**T12J**		2.25	
	T13B	0.20	3.29	0.70	**T13F**	0.20	3.29	0.70	**T13J**	0.20	3.29	0.70
	T14B		3.10		**T14F**		3.10		**T14J**		3.10	
	T15B		4.36		**T15F**		4.36		**T15J**		4.36	
	T16B		4.43		**T16F**		4.43		**T16J**		4.43	
0.5	**T17C**	0.10	1.74	0.65	**T17G**	0.10	1.74	0.65	**T17K**	0.10	1.74	0.65
	T18C		2.18		**T18G**		2.18		**T18K**		2.18	
	T19C		1.58		**T19G**		1.58		**T19K**		1.58	
	T20C		2.25		**T20G**		2.25		**T20K**		2.25	
	T21C	0.20	3.29	0.60	**T21G**	0.20	3.29	0.60	**T21K**	0.20	3.29	0.60
	T22C		3.10		**T22G**		3.10		**T22K**		3.10	
	T23C		4.36		**T23G**		4.36		**T23K**		4.36	
	T24C		4.43		**T24G**		4.43		**T24K**		4.43	
-1.5	**T25D**	0.10	1.74	0.85	**T25H**	0.10	1.74	0.85	**T25L**	0.10	1.74	0.85
	T26D		2.18		**T26H**		2.18		**T26L**		2.18	
	T27D		1.58		**T27H**		1.58		**T27L**		1.58	
	T28D		2.25		**T28H**		2.25		**T28L**		2.25	
	T29D	0.20	3.29	1.00	**T29H**	0.20	3.29	1.00	**T29L**	0.20	3.29	1.00
	T30D		3.10		**T30H**		3.10		**T30L**		3.10	
	T31D		4.36		**T31H**		4.36		**T31L**		4.36	
	T32D		4.43		**T32H**		4.43		**T32L**		4.43	

For each wave attack the wave steepness remains constant and close to 2%. All simulations were carried out without the implementation of the turbulent model. The model settings adopted are shown in Table 4.2.

Table 4.2. Model settings adopted for the numerical simulations.

Boundary Condition		**Mesh resolution**			
Seaward	Landward	cell width [m]	cell height [m]		
Hs - Tp (Jonswap spectrum)	absorption	0.02	Off-shore	Dike crest	In-shore
			0.02÷0.05	0.02	0.02÷0.04

The dimensions of the structure (crest width and height) are constant while crest freeboard R_c, seaward α_{off} and landward α_{in} slopes are variable (Figure 4.6).
By combining different geometries and wave attacks, a total of 96 tests were carried out.

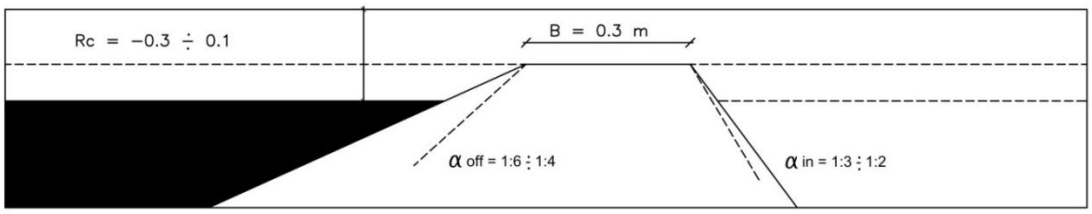

Figure 4.6. Tested levee cross section (model-scale units).

4.4 Validation of the model

In order to verify the numerical simulations, selected numerical results were compared against experimental data and consolidated theoretical formulae. In particular, it was verified that the wave reflection coefficients calculated numerically for each test were compatible with the experimental results obtained by Zanuttigh et al. (2006). Moreover, also the overtopping discharges were compared with the theoretical formula by Van der Meer (Eurotop, 2007).

4.4.1 Wave reflection coefficient

The reflection coefficients K_r obtained by the simulations were compared in Figure 4.7, 4.8 and 4.9 with the data for smooth straight slopes that are included in the reflection database by Zanuttigh and Van der Meer (2006). It is worthy to remark that this database includes structures in design conditions ($R_c/H_s > 0.5$, $H_s/D_{50} > 1$, sop>1%).

In these graphs all the numerical tests for the structures with different seaward and landward slopes are shown. The values of K_r for emerged and zero freeboard cases fall perfectly in the range of the experimental values. As expected, submerged conditions give lower values of K_r, falling under the range of the experimental data or at least in its bottom part. Notwithstanding the numerical values of K_r appear to be slightly greater than the experimental values. However, the numerical trends show two key issues in agreement with the physical process: the greater the submergence and/or the lower the wave height, the lower the reflection.

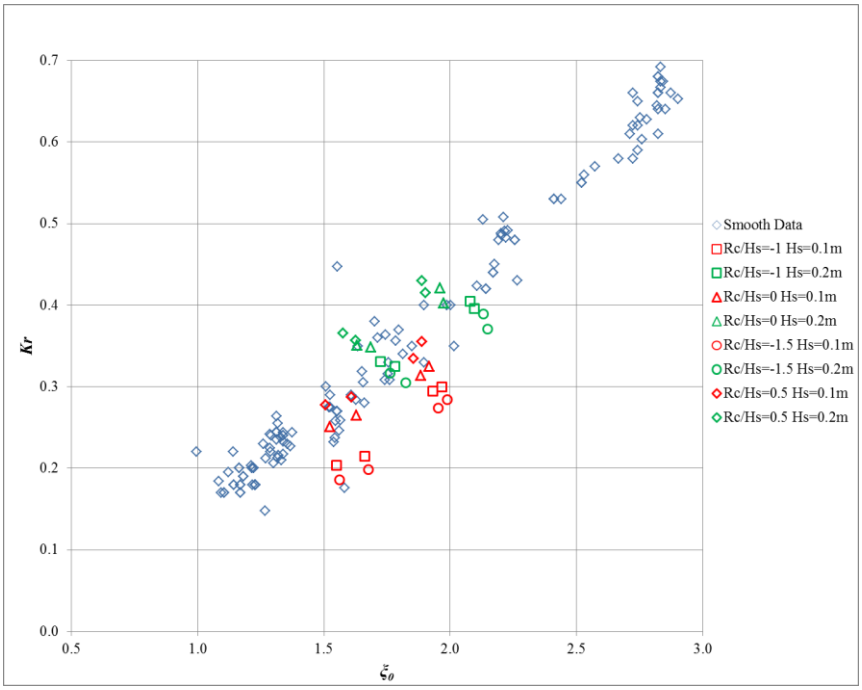

Figure 4.7. K_r obtained by the experimental database for smooth straight (Zanuttigh and Van der Meer, 2006) and the numerical simulation characterized by $\alpha_{off} = 1{:}4$ and $\alpha_{in} = 1{:}3$.

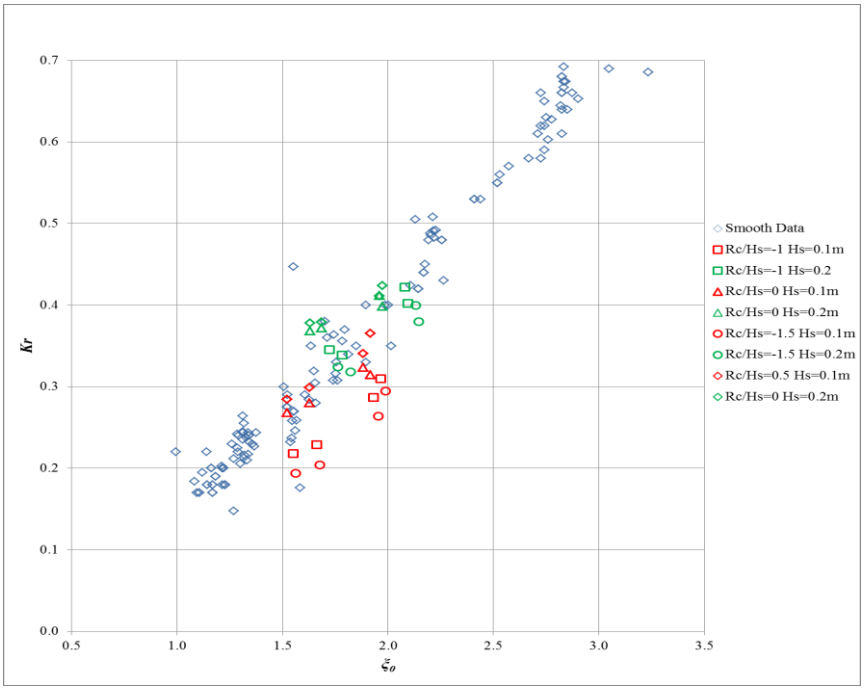

Figure 4.8. K_r obtained by the experimental database for smooth straight (Zanuttigh and Van der Meer, 2006) and the numerical simulation characterized by $\alpha_{off} = 1{:}4$ and $\alpha_{in} = 1{:}2$.

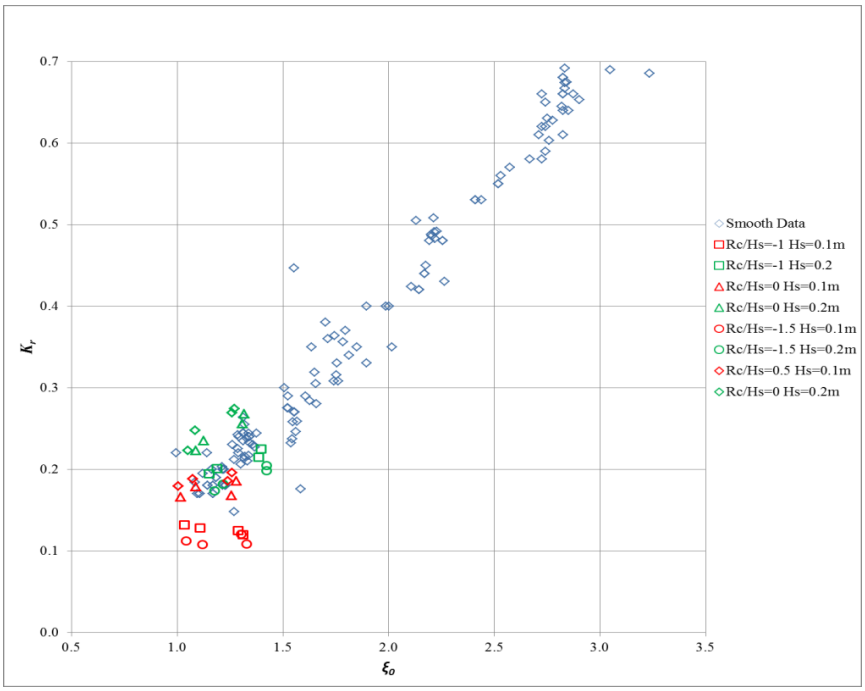

Figure 4.9. K_r obtained by the experimental database for smooth straight (Zanuttigh and Van der Meer, 2006) and the numerical simulation characterized by $\alpha_{off} = 1{:}6$ and $\alpha_{in} = 1{:}3$.

4.4.2 Overtopping discharge

Tables 4.3, 4.4 and 4.5 report the discharge calculated numerically and theoretically for emerged structures, structures with freeboard zero and submerged structures respectively. For emerged cases the theoretical discharge is calculated by Equation (4.3), for cases with freeboard zero the formulae used are Equations (4.7) and (4.8) and, finally, Equation (4.3) is used for submerged cases.

Both for emerged cases and cases with freeboard zero, the theoretical discharge is well represented and the relative error remains always under about 28%. The following figures (4.10 and 4.11) report this good agreement showing the theoretical discharge vs the numerical one.

Table 4.3. Emerged cases: theoretical total discharge qth, numerical total discharge qnum, relative error Err (%).

Tests	qth	qnum	Err(%)	Tests	qth	qnum	Err(%)	Tests	qth	qnum	Err(%)
T17C	0.005	0.005	8.81	**T17G**	0.005	0.004	21.99	**T17K**	0.002	0.003	26.56
T18C	0.007	0.009	24.21	**T18G**	0.007	0.008	15.44	**T18K**	0.003	0.003	10.62
T19C	0.004	0.005	25.89	**T19G**	0.004	0.005	28.31	**T19K**	0.002	0.002	25.89
T20C	0.007	0.008	5.43	**T20G**	0.007	0.009	27.92	**T20K**	0.003	0.004	23.81
T21C	0.014	0.015	6.01	**T21G**	0.014	0.017	16.61	**T21K**	0.006	0.008	20.60
T22C	0.013	0.015	17.89	**T22G**	0.013	0.016	20.19	**T22K**	0.006	0.007	17.60
T23C	0.020	0.022	11.22	**T23G**	0.020	0.022	8.74	**T23K**	0.010	0.010	3.75
T24C	0.020	0.024	17.66	**T24G**	0.020	0.022	4.97	**T24K**	0.010	0.010	4.59

Table 4.4. Cases with freeboard zero: theoretical total discharge qth, numerical total discharge qnum, relative error Err (%).

Tests	qth	qnum	Err(%)	Tests	qth	qnum	Err(%)	Tests	qth	qnum	Err(%)
T9B	0.009	0.008	12.19	**T9F**	0.009	0.010	15.53	**T17J**	0.006	0.005	8.15
T10B	0.010	0.010	1.88	**T10F**	0.010	0.011	4.88	**T18J**	0.007	0.007	7.87
T11B	0.008	0.010	17.33	**T11F**	0.008	0.010	17.33	**T19J**	0.005	0.006	13.01
T12B	0.010	0.011	3.08	**T12F**	0.010	0.012	18.78	**T20J**	0.007	0.008	14.86
T13B	0.025	0.021	16.69	**T13F**	0.025	0.030	16.47	**T21J**	0.017	0.016	6.43
T14B	0.025	0.027	8.50	**T14F**	0.025	0.022	9.45	**T22J**	0.016	0.017	0.96
T15B	0.029	0.034	16.76	**T15F**	0.029	0.031	5.90	**T23J**	0.020	0.023	18.12
T16B	0.030	0.030	1.06	**T16F**	0.030	0.033	10.83	**T24J**	0.020	0.022	11.67

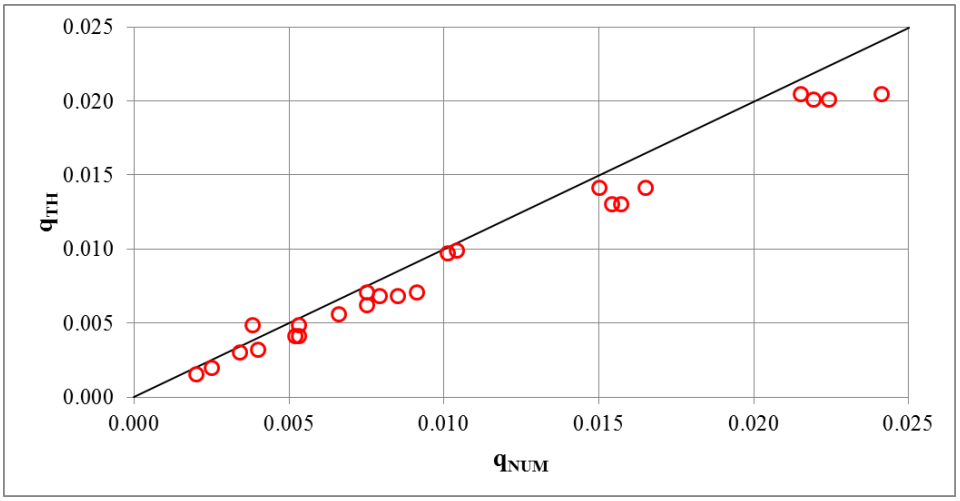

Figure 4.10. Total numerical discharge q_{NUM} versus total theoretical discharge q_{TH} for emerged cases.

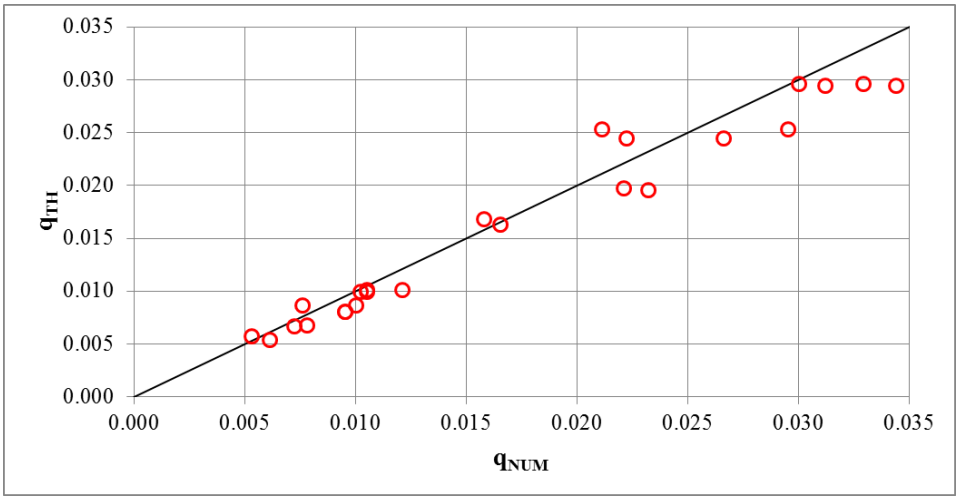

Figure 4.11. Total numerical discharge q_{NUM} versus total theoretical discharge q_{TH} for cases with zero freeboard.

As regards submerged cases, by calculating the relative error, we can observe that there is a good agreement between the numerical and theoretical overflow discharge, whereas the differences for the overtopping discharge are more marked. However, this contribute is very small and so it not affects too much the total results.

Table 4.5. Submerged cases: theoretical/numerical overtopping discharge q_wth/$q_w$num, theoretical/numerical overflow discharge q_sth/$q_s$num, relative error E(%).

Tests	q_wth	$q_w$num	E(%)	q_sth	$q_s$num	E(%)
T1A	0.009	0.011	21.12	1.879	1.787	4.89
T2A	0.010	0.011	6.13	1.879	1.724	8.25
T3A	0.008	0.009	12.14	1.879	1.812	3.59
T4A	0.011	0.011	5.21	1.879	1.764	6.15
T5A	0.027	0.019	27.60	1.879	1.877	0.10
T6A	0.026	0.022	13.94	1.879	1.865	0.76
T7A	0.003	0.004	23.78	1.879	1.873	0.32
T8A	0.003	0.004	16.28	1.879	1.907	1.48
T25D	0.009	0.010	11.10	3.452	3.121	9.61
T26D	0.010	0.012	11.69	3.452	3.307	4.21
T27D	0.008	0.009	4.83	3.452	3.316	3.95
T28D	0.011	0.011	4.02	3.452	3.398	1.57
T29D	0.027	0.028	2.85	3.452	3.298	4.47
T30D	0.027	0.030	13.57	3.452	3.320	3.83
T31D	0.003	0.003	11.01	3.452	3.182	7.84
T32D	0.003	0.003	16.65	3.452	3.247	5.95
T1E	0.009	0.010	8.67	1.879	1.771	5.74
T2E	0.010	0.011	8.08	1.879	1.739	7.49
T3E	0.008	0.009	4.37	1.879	1.912	1.73
T4E	0.01	0.012	12.87	1.879	1.788	4.85
T5E	0.027	0.024	9.68	1.879	1.873	0.33
T6E	0.026	0.022	15.10	1.879	1.748	6.99
T7E	0.003	0.004	20.08	1.879	1.858	1.11
T8E	0.003	0.003	20.65	1.879	1.844	1.89
T25H	0.009	0.008	9.10	3.452	3.290	4.70
T26H	0.010	0.012	11.69	3.452	3.187	7.69
T27H	0.008	0.009	12.06	3.452	3.278	5.06
T28H	0.011	0.010	7.33	3.452	3.303	4.33
T29H	0.027	0.023	15.02	3.452	3.081	10.77
T30H	0.027	0.024	8.31	3.452	3.208	7.09
T31H	0.003	0.003	9.19	3.452	3.126	9.45
T32H	0.003	0.003	16.27	3.452	3.247	5.96
T1I	0.006	0.0058	1.52	1.8793	1.8965	0.9176
T2I	0.007	0.0085	24.14	1.8793	1.8995	1.0773
T3I	0.005	0.0049	10.80	1.8793	1.9052	1.3806
T4I	0.007	0.0082	17.65	1.8793	1.9041	1.3221
T5I	0.018	0.0184	3.01	1.8793	1.8053	3.9353
T6I	0.017	0.0205	18.67	1.8793	1.9058	1.4125
T7I	0.021	0.0239	14.69	1.8793	1.8784	0.0455
T8I	0.021	0.0231	10.01	1.8793	1.9090	1.5828
T25K	0.006	0.0060	1.00	3.4524	3.4225	0.8664
T26K	0.007	0.0075	8.32	3.4524	3.4017	1.4689
T27K	0.006	0.0058	4.83	3.4524	3.3927	1.7296
T28K	0.007	0.0057	19.15	3.4524	3.2586	5.6138
T29K	0.018	0.0205	12.15	3.4524	3.2333	6.3466
T30K	0.018	0.0206	16.59	3.4524	3.6168	4.7615
T31K	0.021	0.0211	1.20	3.4524	3.5116	1.7144
T32K	0.021	0.0276	29.24	3.4524	3.1296	9.3503

4.5 Flow height evolution over the dike crest

In this paragraph the effects of the structure design parameters on the trend of depths of the flow over the crest are investigated. The values of $h_{2\%}$ (flow depth exceeded by 2% of the waves) and $T_{2\%}$ (wave period exceeded by 2% of the waves) at the dike off-shore edge are summarized in Table 4.6 for all the tests. All the numerical results are compared with the theory reported in the paragraph 4.2.

4.5.1 Influence of the dike submergence and geometry

Figure 4.12 shows the wave height trend over the crest structure for a test characterized by $H_s = 0.1\,m$, $T_p = 1.74$ s, $\alpha_{off} = 1{:}4$ and $\alpha_{in} = 1{:}3$. It appears that in case of $R_c/H_s = 0$ and $R_c/H_S = 0.5$, the evolution of the wave height is similar to the literature results in case of emerged structures (Schuttrumpf, 2001; Van Gent, 2002; Schuttrumpf and Van Gent, 2003; Schuttrumpf and Oumeraci, 2005; Bosman, 2008), i.e the wave height tends to decrease along the crest. By increasing the submergence, the decay of the wave height is less marked and it completely disappears when $R_c/H_s = -1.5$.

In Figure 4.13, the evolution of the overtopping flow depth on the dike crest is reported for the structures with different α_{in}. In the same graph the results obtained for the same wave attack and different submergences are shown. As expected, irrespectively of the submergence, the influence of the α_{in} appears to be negligible. This means that the flow remains always subcritical over the crest under a sufficient hydraulic head.

The same comparison is reported in Figure 4.14 between structures characterized by different α_{off}. As in Figure 4.14, the results obtained for the same wave attack and different submergences are reported. It is possible to observe that, only in case of $R_c/H_s = 0$ and $R_c/H_s = 0.5$ the variation of α_{off} affect the evolution on the dike crest of the overtopping flow depth and a slight discrepancy among the results is present. Hence for emerged structures the wave decay over the crest is less marked decreasing the seaward steepness.

Table 4.6. Flow characteristics at the dike off-shore edge (x_c=0).

Tests	$h_{2\%}$ (x_c=0)	$T_{2\%}$ (x_c=0)	$u_{2\%}$ (x_c=0)	Tests	$h_{2\%}$ (x_c=0)	$T_{2\%}$ (x_c=0)	$u_{2\%}$ (x_c=0)	Tests	$h_{2\%}$ (x_c=0)	$T_{2\%}$ (x_c=0)	$u_{2\%}$ (x_c=0)
T1A	0.114	1.200	0.319	**T1E**	0.116	1.187	0.315	**T1I**	0.114	1.158	0.332
T2A	0.142	1.529	0.391	**T2E**	0.146	1.468	0.373	**T2I**	0.114	1.178	0.334
T3A	0.099	1.103	0.284	**T3E**	0.100	1.108	0.286	**T3I**	0.100	1.064	0.298
T4A	0.143	1.589	0.385	**T4E**	0.147	1.535	0.365	**T4I**	0.139	1.552	0.408
T5A	0.279	2.156	0.607	**T5E**	0.277	2.147	0.614	**T5I**	0.284	2.122	0.611
T6A	0.265	2.086	0.574	**T6E**	0.262	2.024	0.583	**T6I**	0.271	1.991	0.574
T7A	0.261	2.533	0.639	**T7E**	0.260	2.520	0.656	**T7I**	0.275	2.410	0.656
T8A	0.261	2.507	0.624	**T8E**	0.258	2.426	0.643	**T8I**	0.272	2.474	0.634
T9B	0.043	0.958	0.672	**T9F**	0.043	0.959	0.665	**T9J**	0.039	1.032	0.667
T10B	0.054	1.197	0.765	**T10F**	0.043	0.959	0.678	**T10J**	0.048	1.254	0.771
T11B	0.039	0.929	0.616	**T11F**	0.039	0.899	0.624	**T11J**	0.036	0.958	0.619
T12B	0.114	2.784	0.992	**T12F**	0.114	2.785	0.904	**T12J**	0.096	3.144	0.963
T13B	0.116	1.855	1.162	**T13F**	0.117	1.859	1.131	**T13J**	0.093	1.960	1.257
T14B	0.111	1.737	1.137	**T14F**	0.112	1.725	1.105	**T14J**	0.090	1.837	1.223
T15B	0.149	2.097	1.148	**T15F**	0.150	2.077	1.142	**T15J**	0.137	2.132	1.256
T16B	0.154	2.012	1.131	**T16F**	0.153	1.996	1.130	**T16J**	0.142	2.102	1.229
T17C	0.029	1.284	0.679	**T17G**	0.023	2.055	0.679	**T17K**	0.026	1.644	0.553
T18C	0.037	1.300	0.679	**T18G**	0.034	1.364	0.680	**T18K**	0.032	1.385	0.679
T19C	0.035	1.294	0.676	**T19G**	0.033	1.250	0.679	**T19K**	0.016	1.300	0.679
T20C	0.050	1.342	0.680	**T20G**	0.040	1.342	0.681	**T20K**	0.040	1.342	0.681
T21C	0.073	1.594	1.001	**T21G**	0.073	1.594	1.001	**T21K**	0.073	1.594	1.002
T22C	0.069	1.579	1.174	**T22G**	0.069	1.582	1.130	**T22K**	0.069	1.582	1.140
T23C	0.093	1.735	1.104	**T23G**	0.095	1.730	1.110	**T23K**	0.093	1.735	1.110
T24C	0.095	1.725	1.121	**T24G**	0.091	1.725	1.132	**T24K**	0.093	1.712	1.532
T25D	0.112	1.177	0.265	**T25H**	0.115	1.163	0.256	**T25L**	0.112	1.141	0.279
T26D	0.142	1.512	0.307	**T26H**	0.147	1.480	0.288	**T26L**	0.144	1.479	0.319
T27D	0.097	1.047	0.242	**T27H**	0.099	1.048	0.239	**T27L**	0.098	1.045	0.255
T28D	0.150	1.500	0.327	**T28H**	0.155	1.441	0.308	**T28L**	0.153	1.458	0.338
T29D	0.270	2.098	0.465	**T29H**	0.268	2.048	0.473	**T29L**	0.286	2.044	0.472
T30D	0.275	2.036	0.449	**T30H**	0.274	1.981	0.455	**T30L**	0.288	1.948	0.453
T31D	0.263	2.314	0.552	**T31H**	0.258	2.315	0.572	**T31L**	0.276	2.284	0.558
T32D	0.254	2.567	0.541	**T32H**	0.250	2.571	0.559	**T32L**	0.264	2.525	0.544

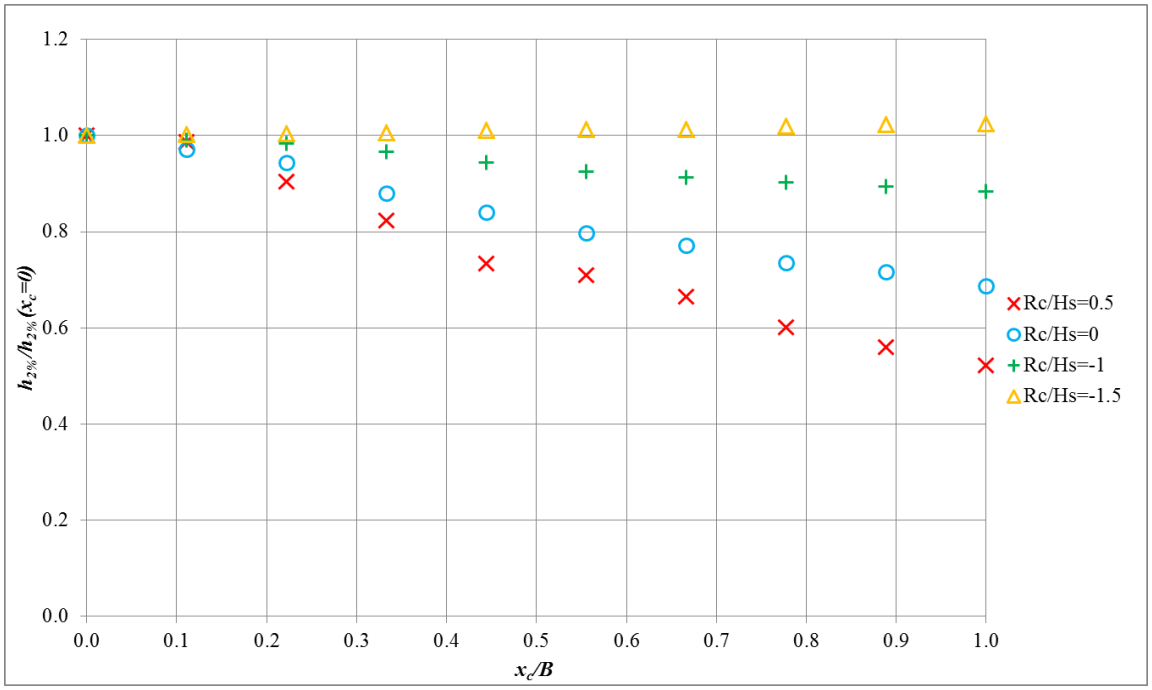

Figure 4.12. Wave height trend on the dike crest for test T17C ($R_c/H_s = 0.5$, red), T9B ($R_c/H_s = 0$, blue), T1A ($R_c/H_s = -1$, green), and T25D ($R_c/H_s = -1.5$, yellow).

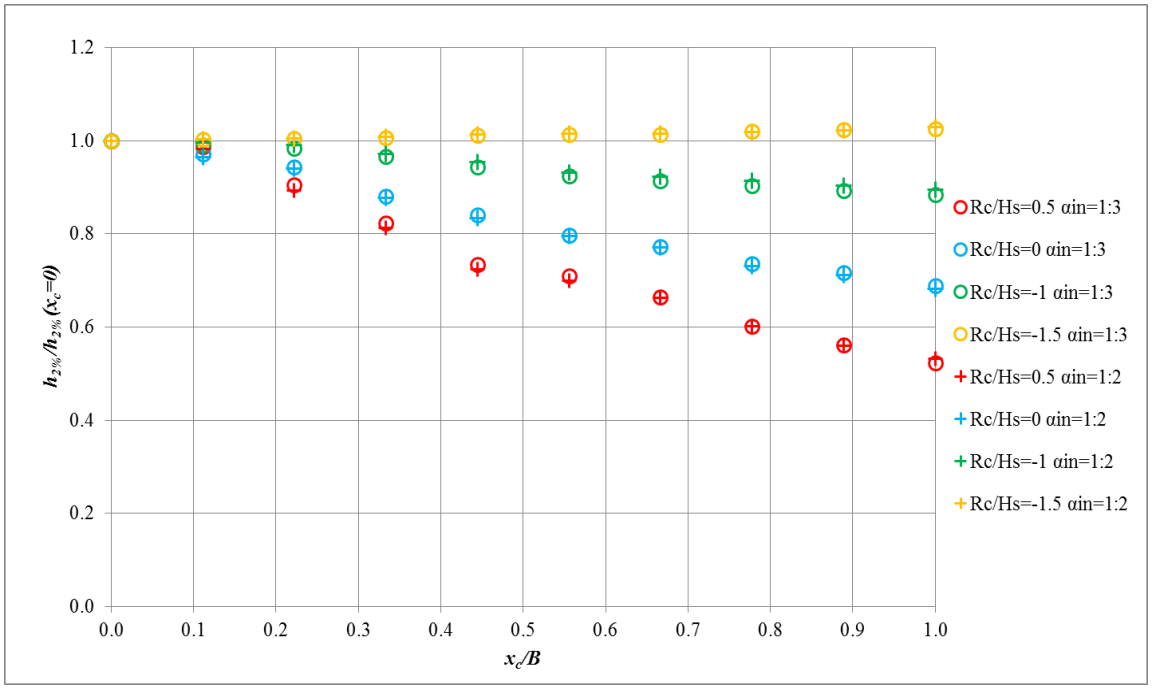

Figure 4.13. Wave height trend on the dike crest for tests characterized by landward slope 1:3 (circles) and 1:2 (crosses) and different freeboard.

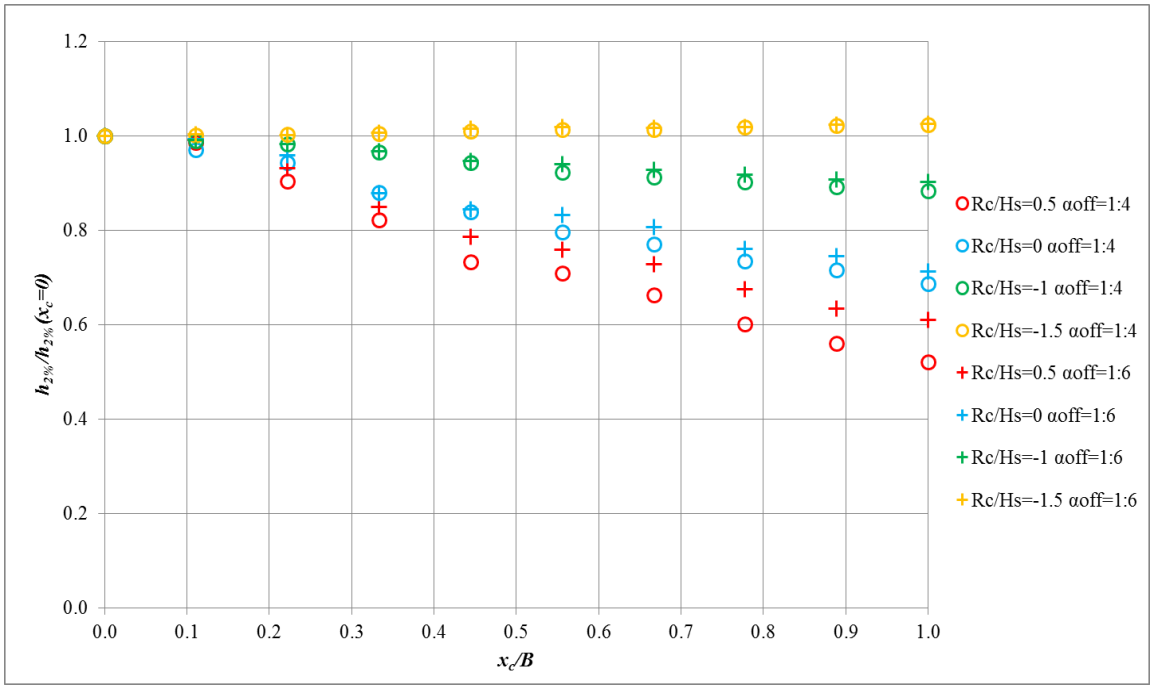

Figure 4.14. Wave height trend on the dike crest for tests characterized by seaward slope 1:4 (circles) and 1:6 (crosses) and different freeboard.

4.5.2 Comparison with the theory

The results obtained by the numerical analysis, i.e. wave height development on the dike crest, are presented in the same way in which are presented in the theoretical approach reported in Eurotop 2007 (Paragraph 4.2). The purpose of this analysis is to fit the variation of the wave height over the dike crest by means of an appropriate curve and identify the key parameters of such fitting.

The numerical results show that, as well as in semi-empirical formulation, the overtopping wave height on the crest of the structure tends to exponentially decrease.
The wave height decay for each test was therefore fitted with an exponential curve and the best fitting coefficient is reported in Table 4.7 for tests with $R_c/H_S = 0.5$, $R_c/H_S = 0$ and $R_c/H_S = -1$. Even if each test is characterized by a specific decay coefficient, it is possible to observe common trends of decay by grouping the tests with similar submergence and wave attacks.

The coefficients and the trend decay depend on the wave height whereas they do not depend on the seaward/landward slope, hence six different average coefficients were calculated for the three values of R_c/H_s and the two of H_s (see Table 4.8).

Table 4.7. Wave decay coefficients of the best fitting and relative standard deviation.

	Tests	c_h	σ'	Tests	c_h	σ'	Tests	c_h	σ'
	T17C	0.65	2.37	**T17G**	0.65	2.09	**T17K**	0.49	1.97
R_c/H_s=0.5	**T18C**	0.85	3.14	**T18G**	0.85	2.25	**T18K**	0.79	0.75
H_s=0.1m	**T19C**	0.64	1.79	**T19G**	0.65	3.34	**T19K**	0.49	1.79
	T20C	0.88	1.46	**T20G**	0.89	2.05	**T20K**	0.78	2.17
	T21C	0.36	2.97	**T21G**	0.37	2.87	**T21K**	0.32	3.51
R_c/H_s=0.5	**T22C**	0.36	0.60	**T22G**	0.39	3.37	**T22K**	0.32	4.21
H_s=0.2m	**T23C**	0.59	2.31	**T23G**	0.58	2.48	**T23K**	0.45	2.56
	T24C	0.61	2.37	**T24G**	0.61	2.62	**T24K**	0.48	2.21
	T9B	0.38	1.03	**T9F**	0.39	0.90	**T9J**	0.44	4.83
R_c/H_s=0	**T10B**	0.41	0.95	**T10F**	0.42	1.03	**T10J**	0.47	1.47
H_s=0.1m	**T11B**	0.36	0.80	**T11F**	0.37	0.60	**T11J**	0.43	0.95
	T12B	0.42	0.63	**T12F**	0.42	0.41	**T12J**	0.46	1.22
	T13B	0.25	1.76	**T13F**	0.24	1.82	**T13J**	0.30	0.67
R_c/H_s=0	**T14B**	0.24	1.57	**T14F**	0.24	1.83	**T14J**	0.29	2.49
H_s=0.2m	**T15B**	0.38	0.99	**T15F**	0.29	0.88	**T15J**	0.39	0.42
	T16B	0.28	1.49	**T16F**	0.29	1.62	**T16J**	0.33	3.98
	T1A	0.12	0.80	**T1E**	0.11	0.67	**T1I**	0.10	0.61
R_c/H_s=-1	**T2A**	0.17	0.32	**T2E**	0.17	0.36	**T2I**	0.13	0.42
H_s=0.1m	**T3A**	0.11	0.20	**T3E**	0.12	0.21	**T3I**	0.09	0.39
	T4A	0.17	0.21	**T4E**	0.27	0.28	**T4I**	0.15	0.23
	T5A	0.07	0.28	**T5E**	0.08	0.35	**T5I**	0.06	0.28
R_c/H_s=-1	**T6A**	0.06	0.23	**T6E**	0.06	0.27	**T6I**	0.05	1.07
H_s=0.2m	**T7A**	0.12	0.47	**T7E**	0.12	0.44	**T7I**	0.10	0.19
	T8A	0.12	0.37	**T8E**	0.12	0.39	**T8I**	0.10	5.21

In Figures 4.15 and 4.16 the tests with $R_c/H_s = 0.5$ and $H_s = 0.1$ m and $H_s = 0.2$ m are shown respectively. Figure 4.17 and 4.18 show the numerical results for tests with $R_c/H_s = 0$ and with $H_s = 0.1$ m and $H_s = 0.2$ m respectively. Finally, Figure 4.19 and 4.20 show the results for tests with $R_c/H_s = -1$ and with $H_s = 0.1$ m and $H_s = 0.2$. Black curves are the fitting curves (obtained by the average coefficients of

Table 4.8) that provides an overall fair approximation, with a decreasing of the quality (for both wave height) in the second half of the crest.

By observing these graph, it immediately appears that the decay is much more marked as the structure is emerged. For this reason this analysis has not been done for the cases with $R_C/H_s = 1.5$ because for those tests the decay is negligible.

Table 4.8. Average wave decay coefficients and relative standard deviation for each tests.

	Average coefficient	**Tests**	**σ'**	**Tests**	**σ'**	**Tests**	**σ'**
R_c/H_s=0.5 H_s=0.1m	0.72	**T17C**	3.79	**T17G**	3.42	**T17K**	8.62
		T18C	5.24	**T18G**	4.77	**T18K**	2.44
		T19C	3.50	**T19G**	4.21	**T19K**	9.13
		T20C	5.74	**T20G**	5.87	**T20K**	3.17
R_c/H_s=0.5 H_s=0.2m	0.45	**T21C**	4.21	**T21G**	3.93	**T21K**	5.45
		T22C	4.01	**T22G**	3.92	**T22K**	6.24
		T23C	6.05	**T23G**	6.37	**T23K**	2.55
		T24C	7.19	**T24G**	7.62	**T24K**	2.48
R_c/H_s=0 H_s=0.1m	0.38	**T9B**	1.04	**T9F**	0.95	**T9J**	2.72
		T10B	1.82	**T10F**	2.13	**T10J**	3.99
		T11B	1.17	**T11F**	0.82	**T11J**	2.53
		T12B	1.72	**T12F**	1.53	**T12J**	3.93
R_c/H_s=0 H_s=0.2m	0.28	**T13B**	2.47	**T13F**	2.78	**T13J**	1.05
		T14B	2.52	**T14F**	2.33	**T14J**	2.17
		T15B	0.94	**T15F**	0.92	**T15J**	2.81
		T16B	1.47	**T16F**	1.58	**T16J**	1.36
R_c/H_s=-1 H_s=0.1m	0.13	**T1A**	0.66	**T1E**	1.34	**T1I**	1.55
		T2A	1.89	**T2E**	2.03	**T2I**	0.43
		T3A	1.17	**T3E**	1.09	**T3I**	2.57
		T4A	1.88	**T4E**	2.02	**T4I**	0.90
R_c/H_s=-1 H_s=0.2m	0.09	**T5A**	0.95	**T5E**	1.00	**T5I**	1.69
		T6A	1.67	**T6E**	1.54	**T6I**	1.31
		T7A	1.72	**T7E**	1.80	**T7I**	0.73
		T8A	1.65	**T8E**	1.76	**T8I**	0.72

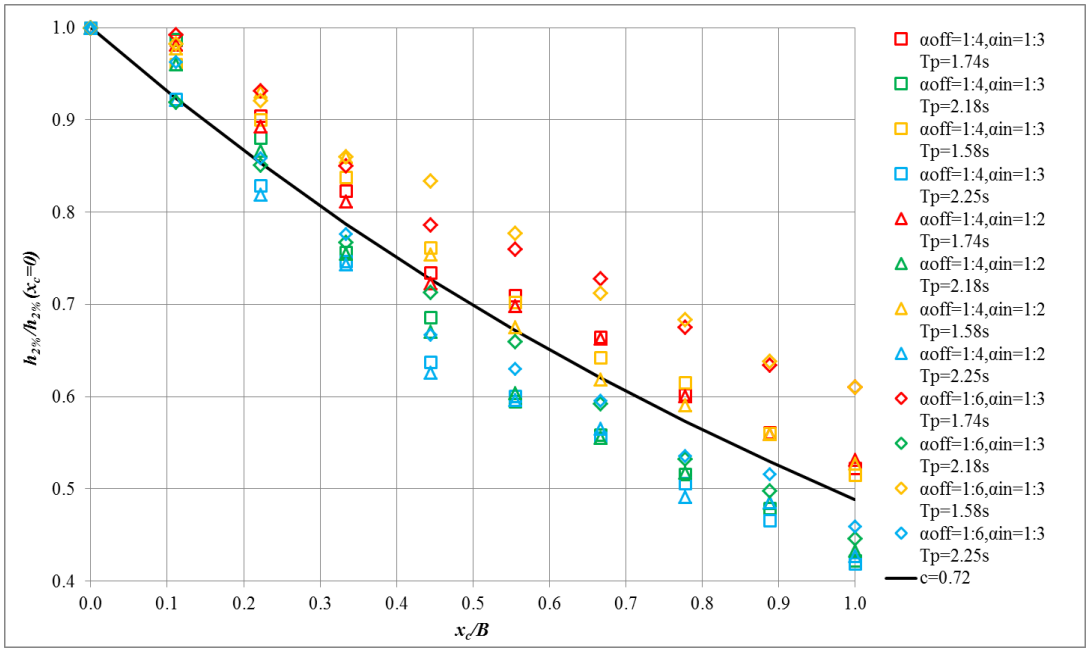

Figure 4.15. Wave height decay on the dike crest with Hs=0.1m and $R_c/H_s = 0.5$. Squares: cases with $\alpha_{off} = 1:4$ and $\alpha_{in} = 1:3$; triangles: cases with $\alpha_{off} = 1:4$ and $\alpha_{in} = 1:2$; diamonds: cases with $\alpha_{off} = 1:6$ and $\alpha_{in} = 1:3$.

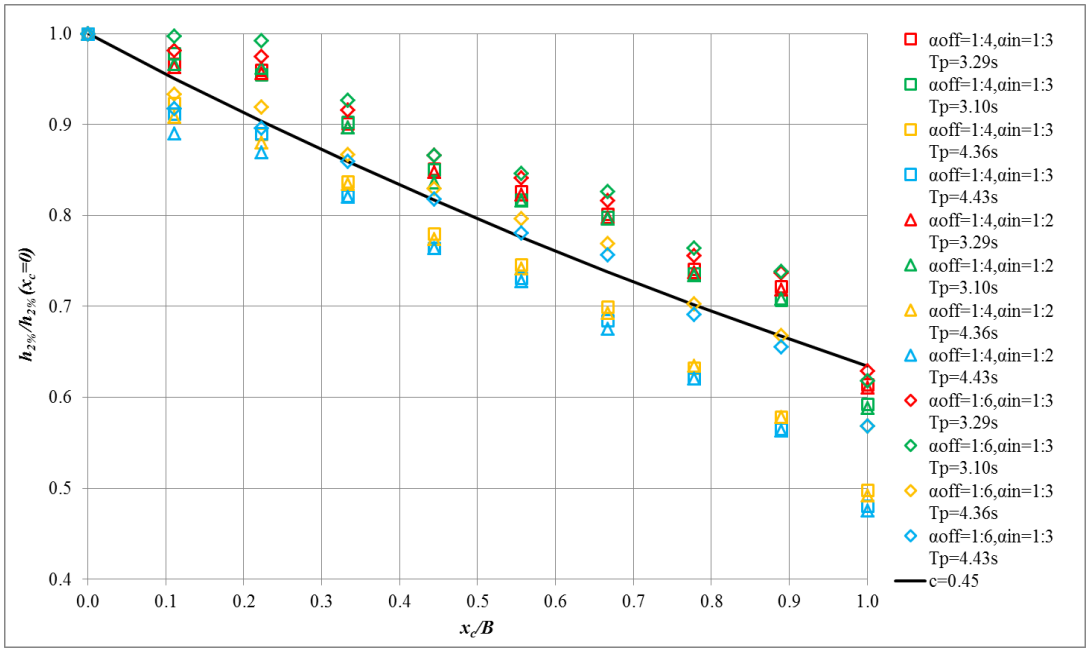

Figure 4.16. Wave height decay on the dike crest with $H_s = 0.2\ m$ and $R_c/H_s = 0.5$. Squares: cases with $\alpha_{off} = 1:4$ and $\alpha_{in} = 1:3$; triangles: cases with $\alpha_{off} = 1:4$ and $\alpha_{in} = 1:2$; diamonds: cases with $\alpha_{off} = 1:6$ and $\alpha_{in} = 1:3$.

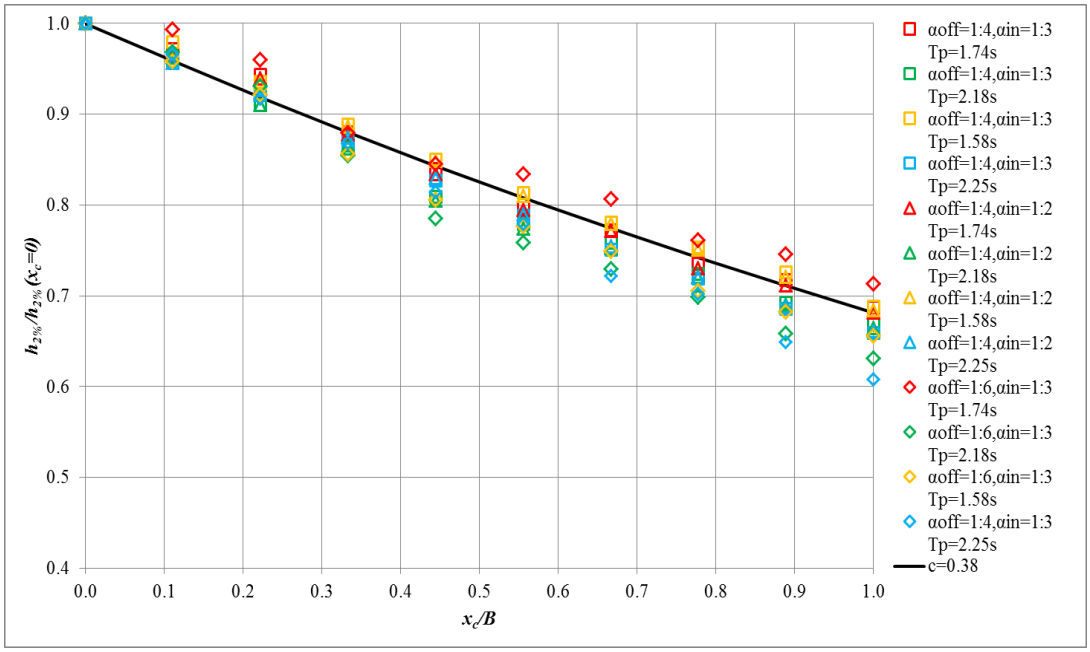

Figure 4.17. Wave height decay on the dike crest with $H_s = 0.1\,m$ and $R_c/H_s = 0$. Squares: cases with $\alpha_{off} = 1{:}4$ and $\alpha_{in} = 1{:}3$; triangles: cases with $\alpha_{off} = 1{:}4$ and $\alpha_{in} = 1{:}2$; diamonds: cases with $\alpha_{off} = 1{:}6$ and $\alpha_{in} = 1{:}3$.

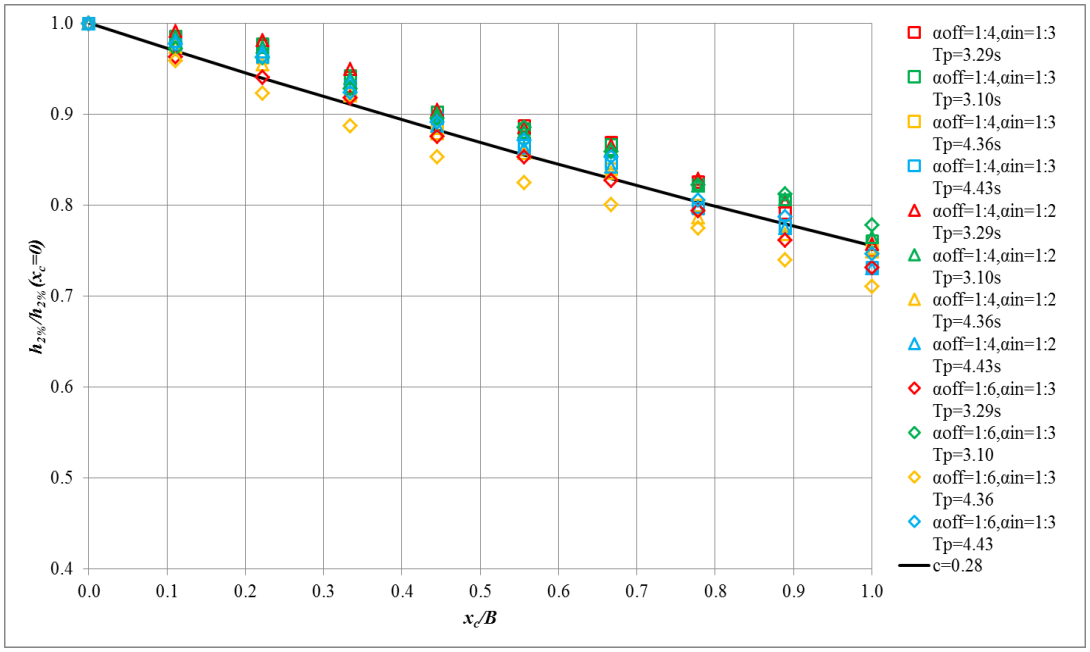

Figure 4.18. Wave height decay on the dike crest with $H_s = 0.2\,m$ and $R_c/H_s = 0$. Squares: cases with $\alpha_{off} = 1{:}4$ and $\alpha_{in} = 1{:}3$; triangles: cases with $\alpha_{off} = 1{:}4$ and $\alpha_{in} = 1{:}2$; diamonds: cases with $\alpha_{off} = 1{:}6$ and $\alpha_{in} = 1{:}3$.

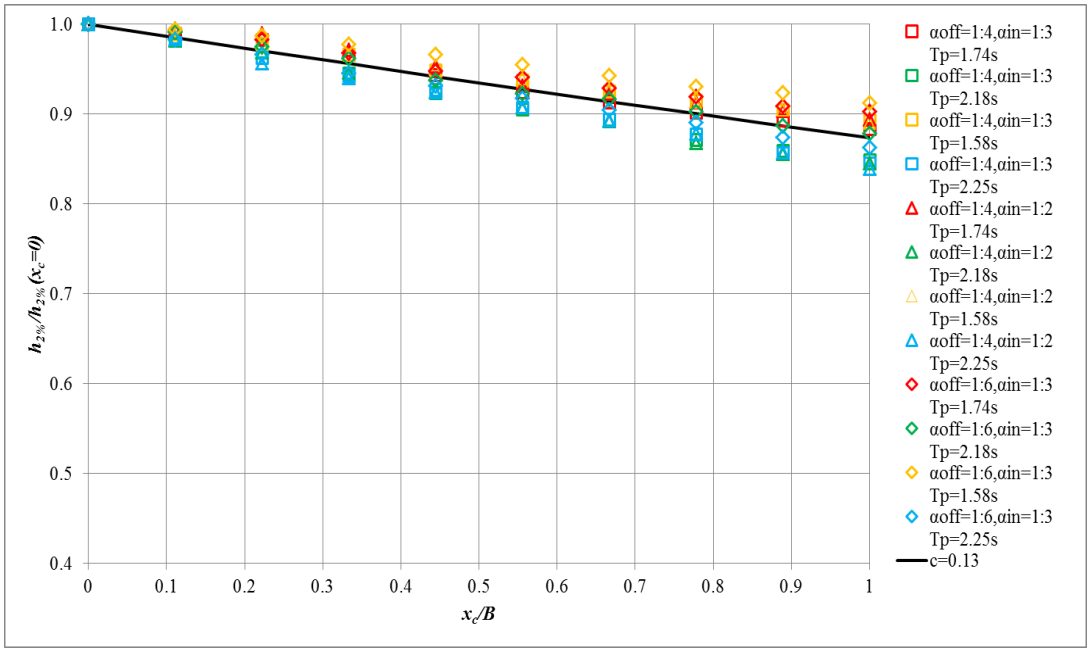

Figure 4.19. Wave height decay on the dike crest with $H_s = 0.1\ m$ and $R_c/H_s = -1$. Squares: cases with $\alpha_{off} = 1{:}4$ and $\alpha_{in} = 1{:}3$; triangles: cases with $\alpha_{off} = 1{:}4$ and $\alpha_{in} = 1{:}2$; diamonds: cases with $\alpha_{off} = 1{:}6$ and $\alpha_{in} = 1{:}3$.

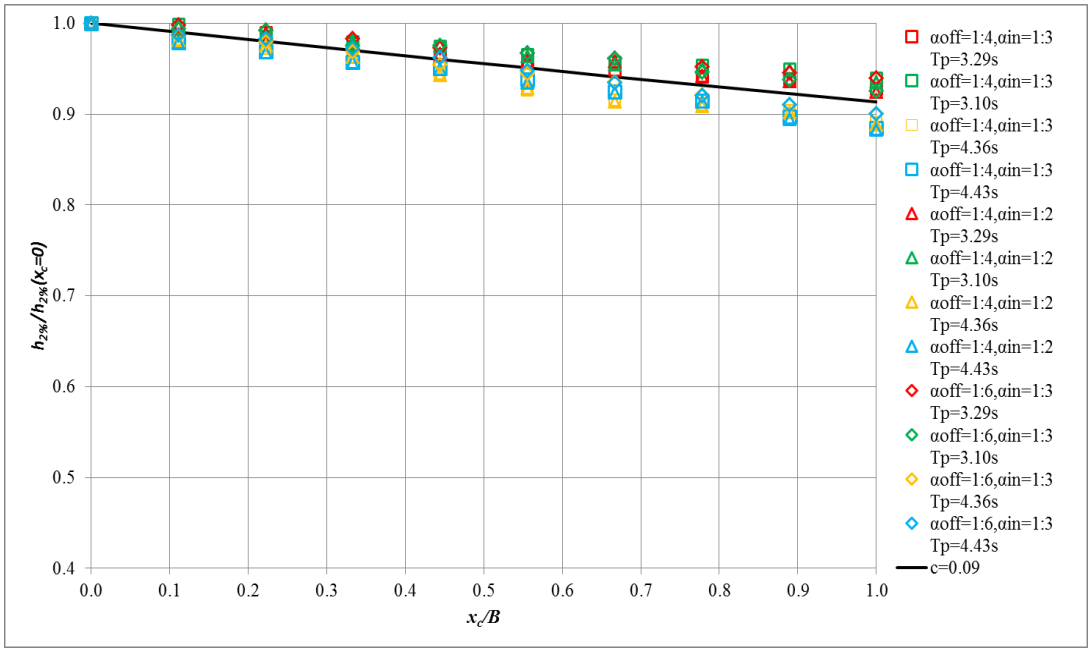

Figure 4.20. Wave height decay on the dike crest with $H_s = 0.1\ m$ and $R_c/H_s = -1$. Squares: cases with $\alpha_{off} = 1{:}4$ and $\alpha_{in} = 1{:}3$; triangles: cases with $\alpha_{off} = 1{:}4$ and $\alpha_{in} = 1{:}2$; diamonds: cases with $\alpha_{off} = 1{:}6$ and $\alpha_{in} = 1{:}3$.

To understand the degree of approximation at the fitted formulation to the numerical data, the standard deviation for each test was calculated (Table 4.5). The values of the standard deviation remains always under about 9% suggesting that the approximation is very good and in particular is more accurate for tests with H_s = 0.1 m.

It is possible to observe that by keeping in constant the submergence, the wave height decay tends to decrease, almost halved, when the significant wave height increases. Similarly, the numerical results show that the wave height decay increases with increasing the submergence when the significant wave height is constant.

4.5.3 Formula for the determination of the decay coefficient

The aim of this sub-paragraph is to understand if it is possible to predict the decay coefficient that controls the decrease of the wave height over the dike crest. For example it could exist a dependence on the wave attack, the characteristics structure and/or the submergence.

An equation describing the trend of the dimensionless coefficient c_h was derived. The formula (Equation 4.14) shows the dependency of c_h from:

- overtopping discharge;
- wave height;
- wave peak period;
- break parameter.

$$c_h = \frac{q}{gH_S T_p} \cdot \frac{H_s}{wd} \cdot \frac{1}{\sqrt{\xi_{m-1,0}}} \tag{4.14}$$

where q the total discharge (in case of submerged structures the sum for the contribute of overflow and the overtop), H_s is the wave height, T_p the peak period, wd the water depth and $\xi_{m-1,0}$ the Irribarren coefficient.

The three following Figures plot all data against Equation 4.14 and show that the trend is different for different submergences. In fact, in Figure 4.21 the cases characterized by $R_c/H_s = -1$ are reported, whereas in Figure 4.22 and 4.23 the cases with $R_c/H_s = 0$ and $R_c/H_s = 0.5$ are respectively represented. It is possible to approximate all points

with a negative exponentially curve and, overall, there is a modest scatter with a determination coefficient close to 0.95.

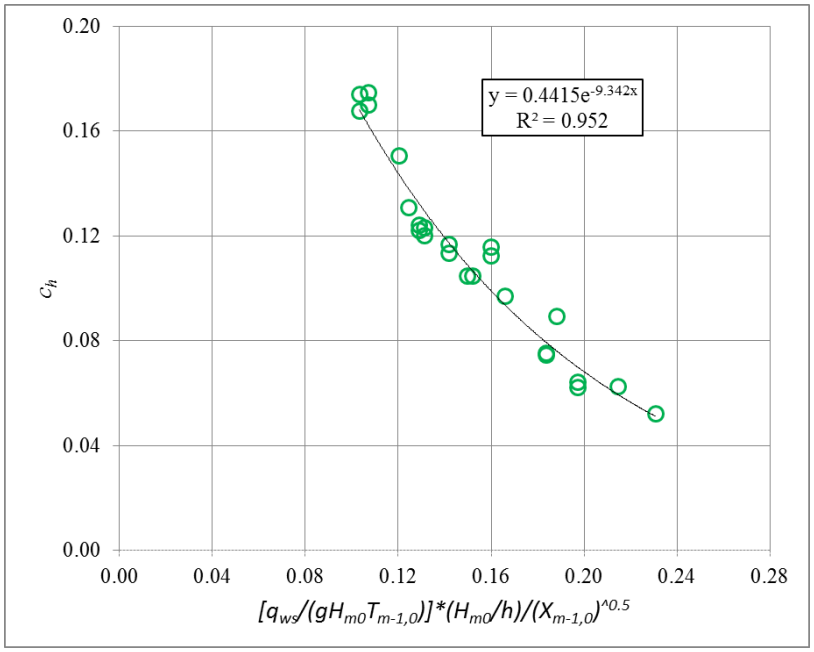

Figure 4.21. Wave decay coefficients against new Equation 4.14. Tests with $R_c/H_s = -1$.

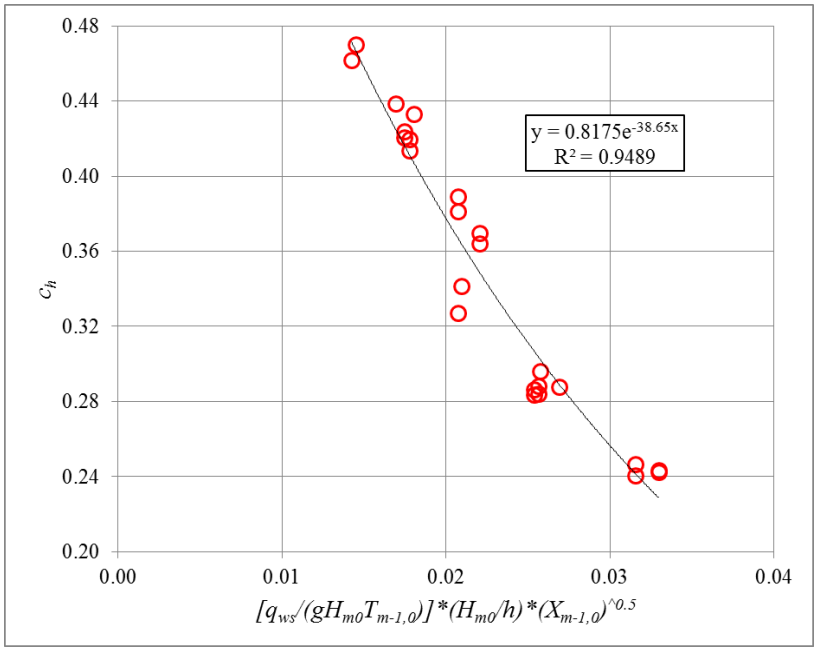

Figure 4.22. Wave decay coefficients against new Equation 4.14. Tests with $R_c/H_s = 0$.

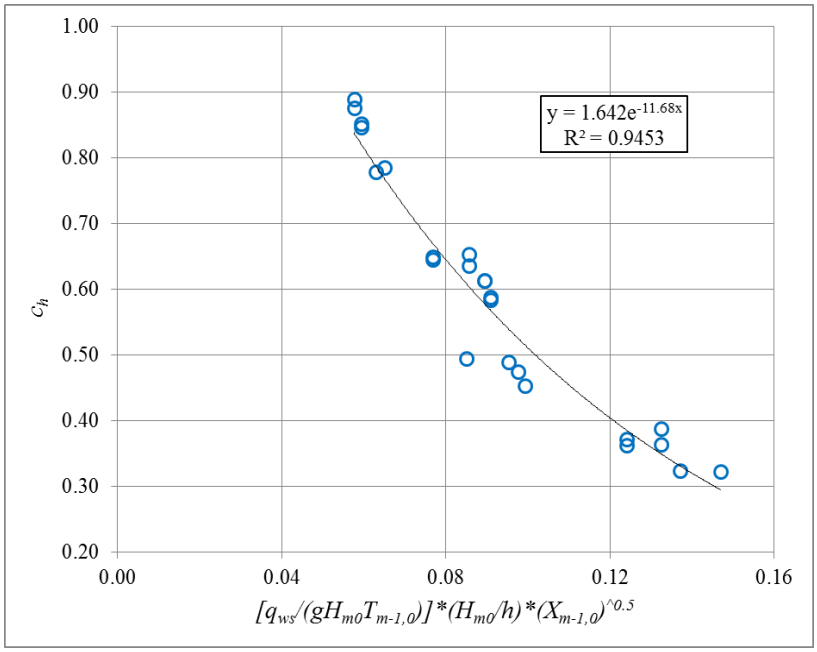

Figure 4.23. Wave decay coefficients against new Equation 4.14. Tests with $R_c/H_s = 0.5$.

4.6 Flow velocity evolution over the dike crest

In this paragraph the evolution of the flow velocity over the dike crest is described; in particular the effects of the structure design parameters on the trend of velocities are investigated. The values of $u_{2\%}$ (flow velocity exceeded by 2% of the waves) at the dike off-shore edge are summarized in Table 4.6 for all the tests. As for the wave height trend, also the numerical results relative to the velocity are compared with the theory reported in the paragraph 4.2.

4.6.1 Influence of the dike submergence and geometry

Figure 4.24 shows the evolution of the overtopping flow velocity by varying the submergence. It can be observed that the velocity increases while the wave travels over the crest, and specifically the growth rate decreases with increasing dike submergence. Moreover, in the submerged cases, the decrease of flow depth (see Figure 4.12) and the increase of velocity start from about the middle of the crest of the structure and however are very modest.

In Figure 4.25, the trends of the overtopping flow velocities on the dike crest are reported for the structures with both landward slope 1:3 (represented as void circles) and 1:2 (represented as crosses). In the same graph the results obtained for different submergence are shown. As regards the overtopping wave height, the influence of the landward slope appears to be negligible. Only in case of $R_c = 0$ (red color) a slight discrepancy among the velocity results obtained for different seaward slopes is present.

Figure 4.26 compares the evolution of the overtopping flow velocities on the dike crest for the 1:4 (represented as void circles) and 1:6 seaward slopes (represented as crosses). It is possible to observe that, irrespectively of the submergence, the seaward slope does not significantly affect the evolution on the dike crest of the overtopping flow velocity.

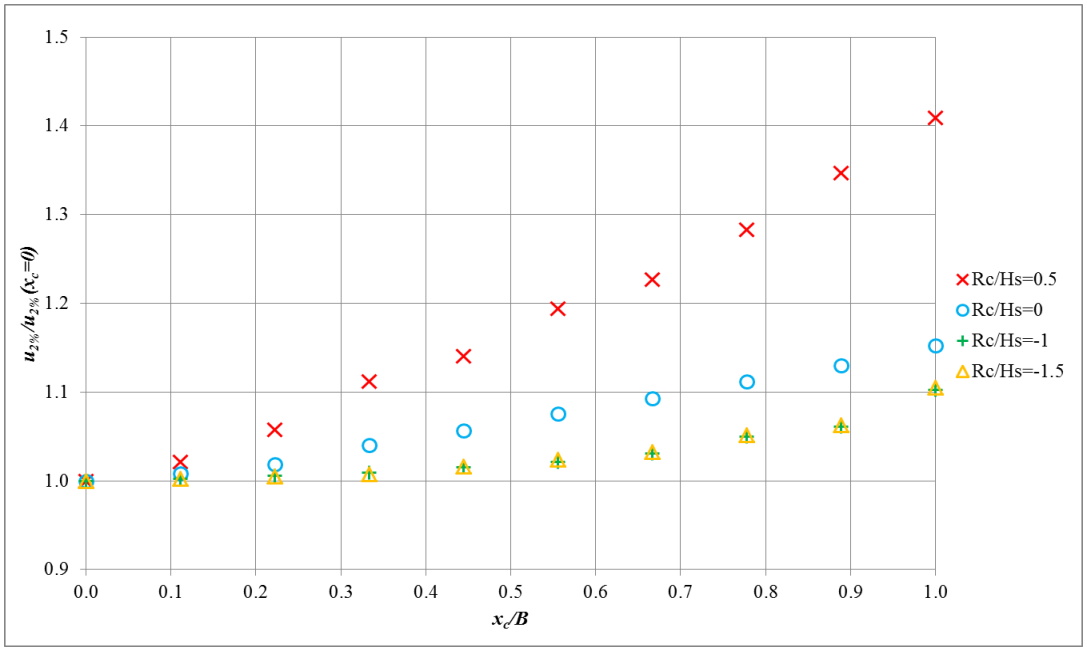

Figure 4.24. Flow velocity trend on the dike crest for test T17C ($R_c/H_s = 0.5$, red), T9B ($R_c/H_s = 0$, blue), T1A ($R_c/H_s = -1$, green) and T25D ($R_c/H_s = -1.5$, yellow).

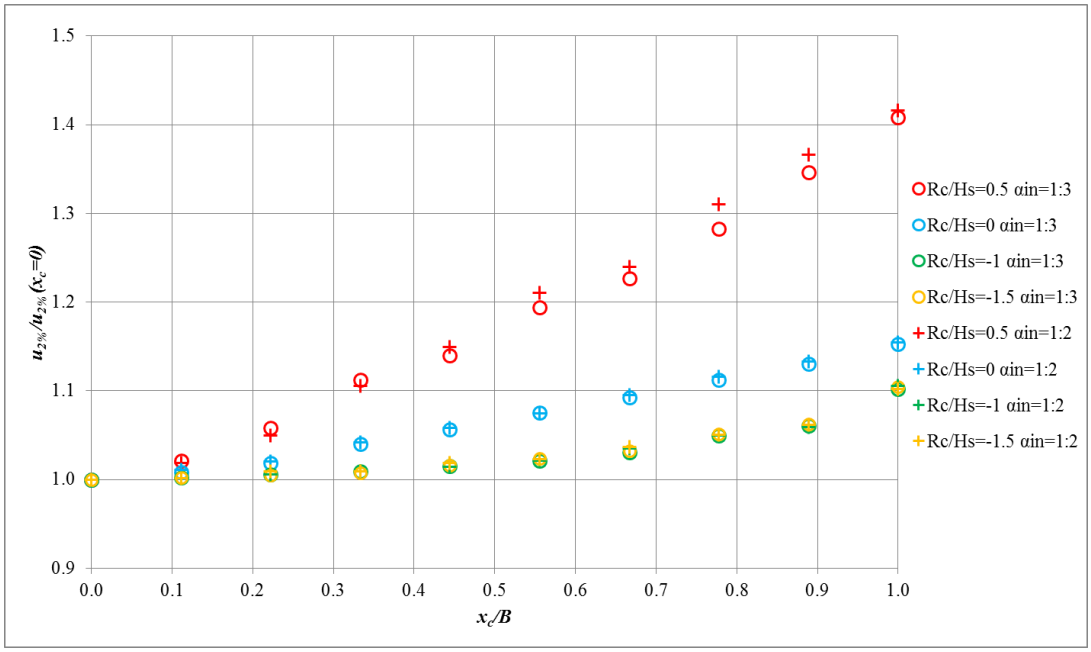

Figure 4.25. Flow velocity trend on the dike crest for tests characterized by landward slope 1:3 (circles) and 1:2 (crosses) and different freeboard.

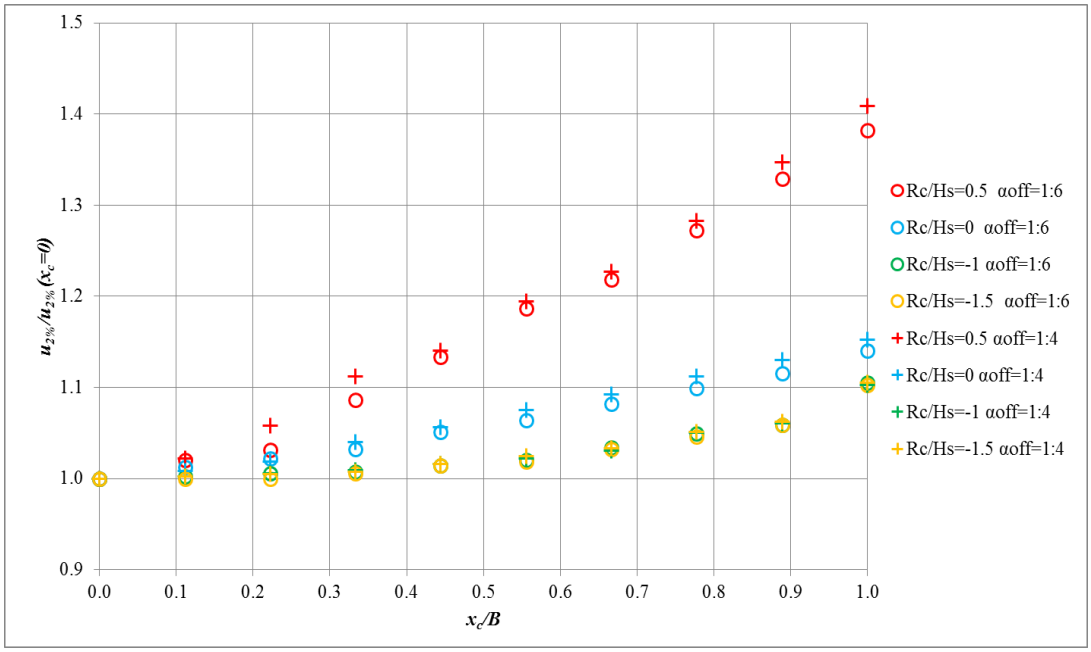

Figure 4.26. Flow velocity trend on the dike crest for tests characterized by seaward slope 1:3 (circles) and 1:6 (crosses) and different freeboard.

4.6.2 Approximation of the velocity trend with a fitting function

The numerical tests show a slight increase of the velocity over the dike crest that can be approximated with a second-order polynomial function. The best fitting coefficients for each tests are reported in Tables 4.9. As for the wave heights, also the coefficients of the velocity are found to be dependent on the wave height and not on the seaward/landward slope. Hence, the average coefficients are reported in Table 4.10.

In Figure 4.27 and 4.28 tests with $R_c/H_s = 0.5$ and the polynomial function obtained by the average coefficients of Table 4.10 are respectively shown. The trend of the velocity on the dike crest is very different for the tests with $H_s = 0.1$ m and $H_s = 0.2$ m. In the cases with $H_s = 0.1$ m the velocity tends to increase from the beginning of the crest, in the cases with $H_s = 0.2$ m there is a first phase of decrease and only after the middle of the crest width the velocity starts to increase. The values of the standard deviation reported (Table 4.10) remains under about 5% showing that the approximation is always very good (irrespectively of the wave height).

Figure 4.29 and 4.30 compares the numerical results for tests with $R_c/H_s = 0$ m and the polynomial function obtained by the average coefficients of Table 4.10. Tests with $H_s = 0.1$ and $H_s = 0.2$ m are respectively reported. Also in these cases, the trend of the velocity on the dike crest is very different for the tests with different wave height. In particular a continuous velocity growth is found for the tests with $H_s = 0.1$ m while for the tests with $H_s = 0.2$ m the velocity tends first to decrease and then to increase starting from the middle of the dike crest. By calculating the standard deviation for each test (Table 4.10), it appears that the discrepancy from the curve remains always very low. In particular, the approximation is better for tests with $H_s = 0.1$ m and the standard deviation remains always under about 2.4%.

In the submerged case (Figures 4.31-4.32), for both wave heights, the trend of the velocity on the dike crest tends to decrease and to increase starting from the middle of the crest. The standard deviation for each tests (Table 4.10) remains under about 5%.

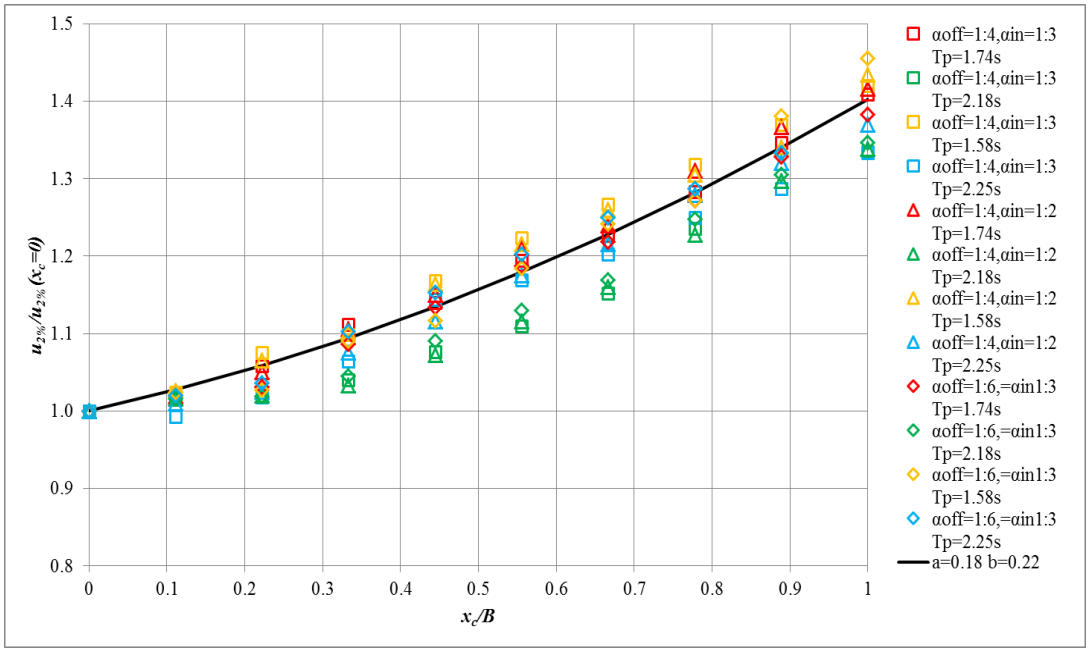

Figure 4.27. Wave velocity evolution on the crest of the structure for tests with $H_s = 0.1\,m$ and $R_c/H_s = 0.5$. Squares: cases with $\alpha_{off} = 1{:}4$ and $\alpha_{in} = 1{:}3$; triangles: cases with $\alpha_{off} = 1{:}4$ and $\alpha_{in} = 1{:}2$; diamonds: cases with $\alpha_{off} = 1{:}6$ and $\alpha_{in} = 1{:}3$.

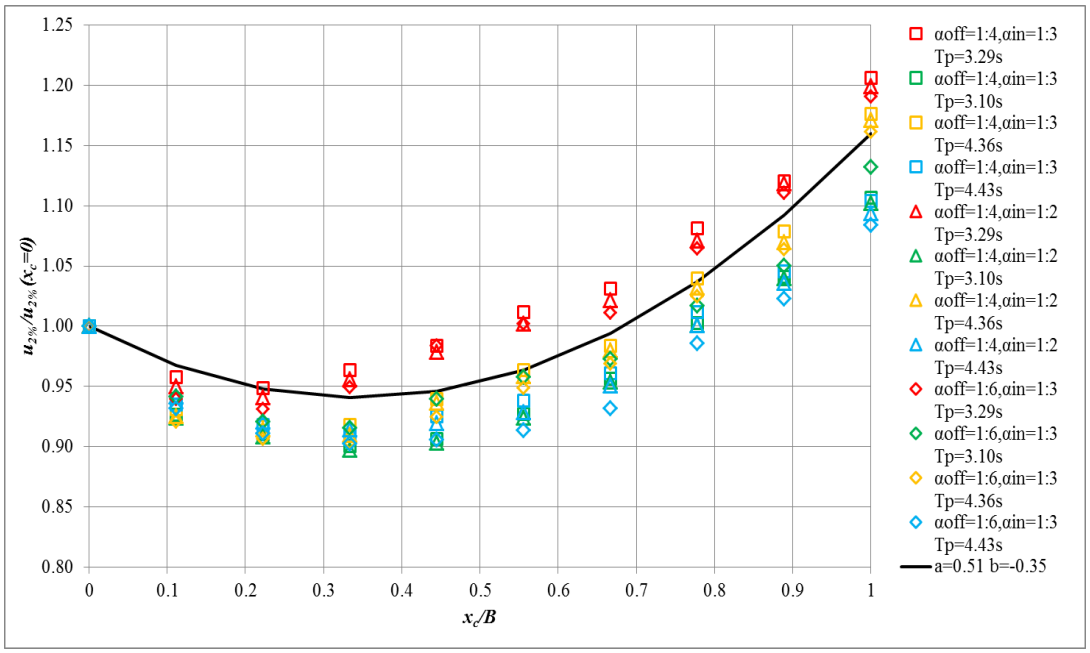

Figure 4.28. Wave velocity evolution on the crest of the structure for tests with $H_s = 0.2\,m$ and $R_c/H_s = 0.5$. Squares: cases with $\alpha_{off} = 1{:}4$ and $\alpha_{in} = 1{:}3$; triangles: cases with $\alpha_{off} = 1{:}4$ and $\alpha_{in} = 1{:}2$; diamonds: cases with $\alpha_{off} = 1{:}6$ and $\alpha_{in} = 1{:}3$.

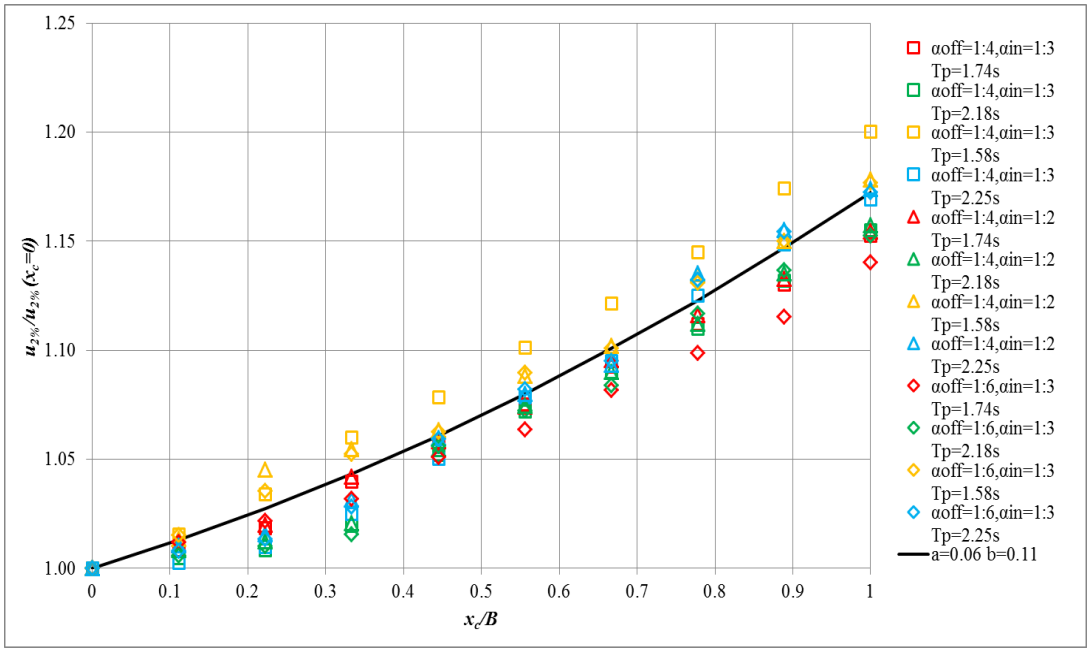

Figure 4.29. Wave velocity evolution on the crest of the structure for tests with $H_s = 0.1\ m$ and $R_c/H_s = 0$. Squares: cases with $\alpha_{off} = 1{:}4$ and $\alpha_{in} = 1{:}3$; triangles: cases with $\alpha_{off} = 1{:}4$ and $\alpha_{in} = 1{:}2$; diamonds: cases with $\alpha_{off} = 1{:}6$ and $\alpha_{in} = 1{:}3$.

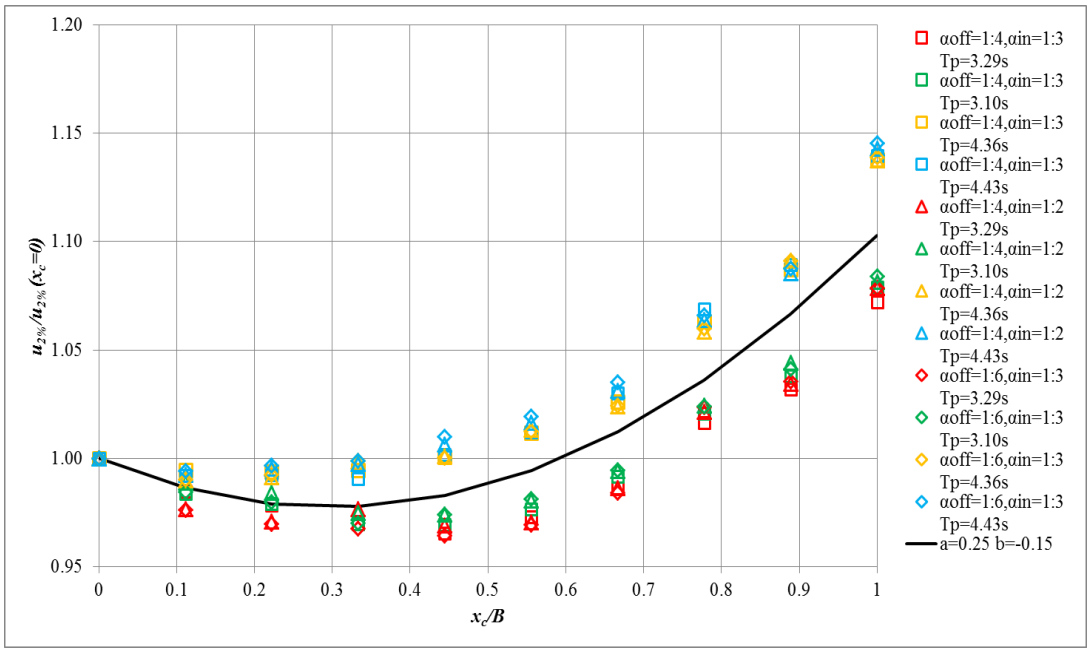

Figure 4.30. Wave velocity evolution on the crest of the structure for tests with $H_s = 0.2\ m$ and $R_c/H_s = 0$. Squares: cases with $\alpha_{off} = 1{:}4$ and $\alpha_{in} = 1{:}3$; triangles: cases with $\alpha_{off} = 1{:}4$ and $\alpha_{in} = 1{:}2$; diamonds: cases with $\alpha_{off} = 1{:}6$ and $\alpha_{in} = 1{:}3$.

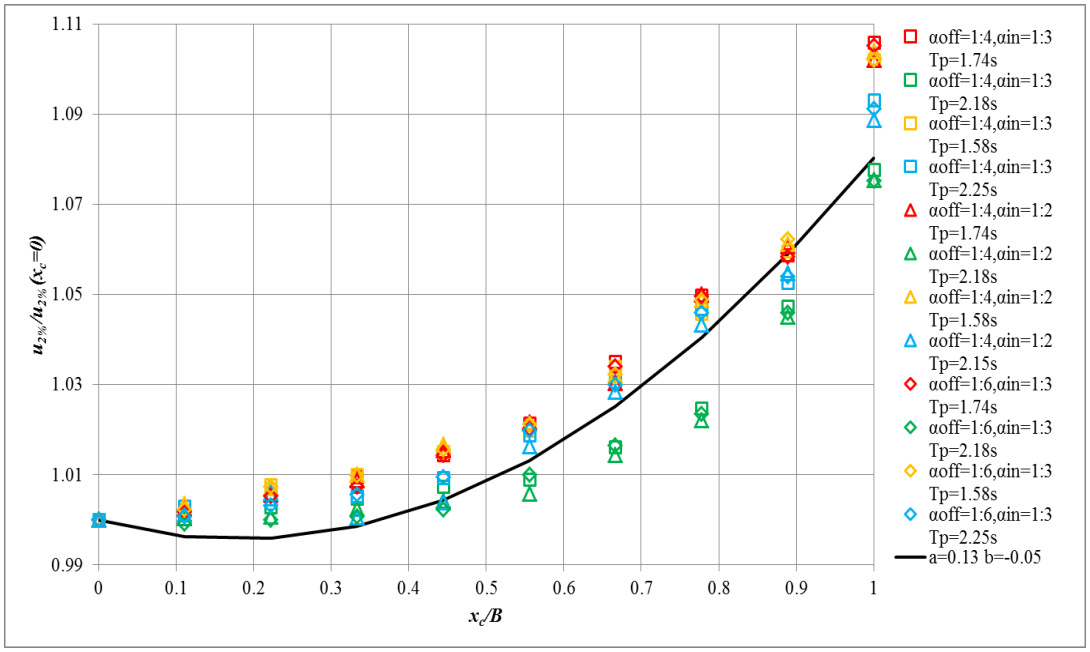

Figure 4.31. Wave velocity evolution on the crest of the structure for tests with $H_s = 0.1\,m$ and $R_c/H_s = -1$. Squares: cases with $\alpha_{off} = 1{:}4$ and $\alpha_{in} = 1{:}3$; triangles: cases with $\alpha_{off} = 1{:}4$ and $\alpha_{in} = 1{:}2$; diamonds: cases with $\alpha_{off} = 1{:}6$ and $\alpha_{in} = 1{:}3$.

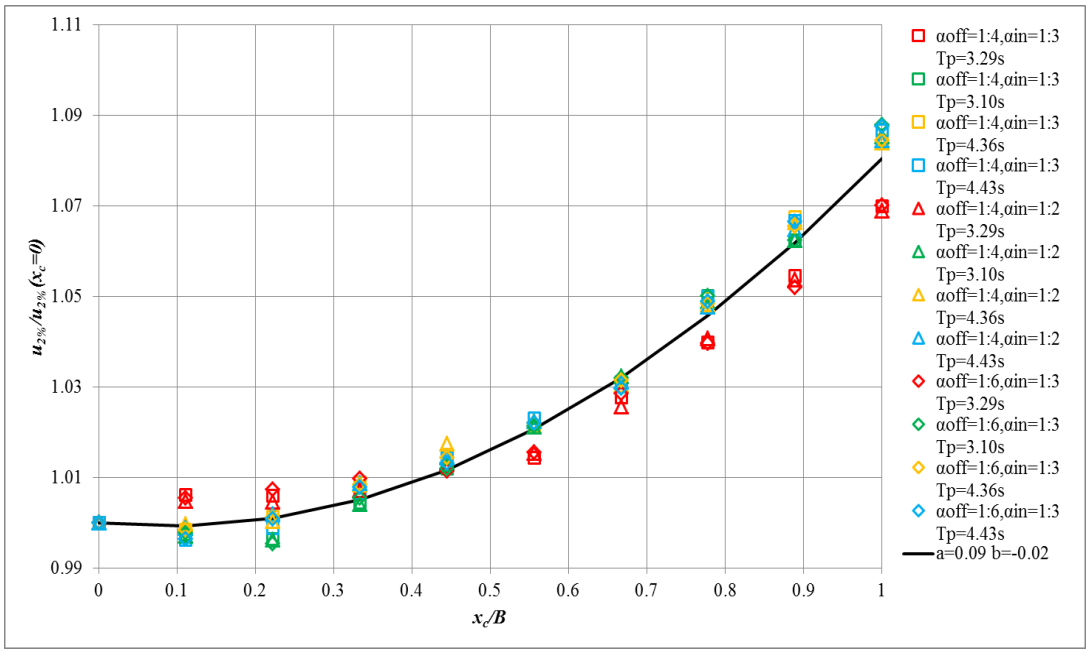

Figure 4.32. Wave velocity evolution on the crest of the structure for tests with $H_s = 0.2\,m$ and $R_c/H_s = -1$. Squares: cases with $\alpha_{off} = 1{:}4$ and $\alpha_{in} = 1{:}3$; triangles: cases with $\alpha_{off} = 1{:}4$ and $\alpha_{in} = 1{:}2$; diamonds: cases with $\alpha_{off} = 1{:}6$ and $\alpha_{in} = 1{:}3$.

Table 4.9. Coefficients obtained with the best fitting curve for the wave velocity on the dike crest and relative standard deviation.

	Tests	a_u	b_u	σ'	Tests	a_u	b_u	σ'	Tests	a_u	b_u	σ'
R_c/H_s=0.5 H_s=0.1m	**T17C**	0.15	0.26	0.68	**T17G**	0.13	0.30	1.32	**T17K**	0.09	0.34	3.92
	T18C	0.32	0.03	0.94	**T18G**	0.33	0.02	0.88	**T18K**	0.29	0.08	1.04
	T19C	0.08	0.36	1.28	**T19G**	0.11	0.32	1.18	**T19K**	0.32	0.14	1.23
	T20C	0.07	0.29	2.94	**T20G**	0.17	0.23	1.79	**T20K**	0.09	0.33	1.92
R_c/H_s=0.5 H_s=0.2m	**T21C**	0.43	-0.22	1.51	**T21G**	0.45	-0.24	1.73	**T21K**	0.44	-0.23	2.44
	T22C	0.54	-0.41	1.98	**T22G**	0.54	-0.41	2.17	**T22K**	0.49	-0.23	1.81
	T23C	0.55	-0.36	2.12	**T23G**	0.56	-0.37	2.34	**T23K**	0.58	-0.40	2.42
	T24C	0.49	-0.36	1.93	**T24G**	0.49	-0.38	1.33	**T24K**	0.53	-0.43	1.51
R_c/H_s=0 H_s=0.1m	**T9B**	0.04	0.11	0.41	**T9F**	0.04	0.12	0.34	**T9J**	0.04	0.11	0.36
	T10B	0.08	0.08	0.85	**T10F**	0.08	0.09	0.70	**T10J**	0.08	0.09	0.97
	T11B	0.04	0.16	0.21	**T11F**	0.04	0.13	0.60	**T11J**	0.05	0.13	0.36
	T12B	0.09	0.09	0.92	**T12F**	0.09	0.09	0.67	**T12J**	0.09	0.10	0.81
R_c/H_s=0 H_s=0.2m	**T13B**	0.26	-0.19	0.49	**T13F**	0.26	-0.19	0.57	**T13J**	0.28	-0.20	0.52
	T14B	0.26	-0.19	0.39	**T14F**	0.25	-0.18	0.55	**T14J**	0.26	-0.18	0.37
	T15B	0.25	-0.12	0.62	**T15F**	0.25	-0.12	0.54	**T15J**	0.25	-0.12	0.58
	T16B	0.25	-0.12	0.45	**T16F**	0.24	-0.11	0.63	**T16J**	0.23	-0.10	0.64
R_c/H_s=-1 H_s=0.1m	**T1A**	0.13	-0.04	0.68	**T1E**	0.13	-0.03	0.73	**T1I**	0.13	-0.04	0.73
	T2A	0.13	-0.07	0.76	**T2E**	0.14	-0.06	0.80	**T2I**	0.13	-0.06	0.60
	T3A	0.13	-0.04	0.77	**T3E**	0.13	-0.03	0.73	**T3I**	0.13	-0.04	0.69
	T4A	0.13	-0.05	0.56	**T4E**	0.12	-0.04	0.64	**T4I**	0.12	-0.04	0.48
R_c/H_s=-1 H_s=0.2m	**T5A**	0.08	-0.02	0.38	**T5E**	0.08	-0.02	0.47	**T5I**	0.08	-0.02	0.47
	T6A	0.10	-0.02	0.23	**T6E**	0.11	-0.02	0.21	**T6I**	0.11	-0.02	0.23
	T7A	0.10	-0.01	0.20	**T7E**	0.10	-0.02	0.20	**T7I**	0.10	-0.01	0.13
	T8A	0.10	-0.01	0.14	**T8E**	0.10	-0.02	0.22	**T8I**	0.11	-0.02	5.13

Table 4.10. Average coefficients for wave velocity evolution on the dike crest and relative standard deviation for each tests.

	Average coefficient		Tests	σ'	Tests	σ'	Tests	σ'
	a_u	b_u						
R_c/H_s=0.5 H_s=0.1m	0.18	0.22	**T17C**	0.82	**T17G**	1.80	**T17K**	1.27
			T18C	5.31	**T18G**	5.18	**T18K**	4.19
			T19C	2.71	**T19G**	2.20	**T19K**	2.48
			T20C	3.62	**T20G**	1.93	**T20K**	1.44
R_c/H_s=0.5 H_s=0.2m	0.51	-0.35	**T21C**	3.27	**T21G**	2.70	**T21K**	2.53
			T22C	3.94	**T22G**	4.20	**T22K**	2.34
			T23C	1.84	**T23G**	2.19	**T23K**	2.73
			T24C	3.30	**T24G**	3.83	**T24K**	5.02
R_c/H_s=0 H_s=0.1m	0.06	0.11	**T9B**	1.00	**T9F**	0.83	**T9J**	0.93
			T10B	1.38	**T10F**	1.18	**T10J**	1.40
			T11B	1.89	**T11F**	0.86	**T11J**	0.59
			T12B	0.95	**T12F**	0.74	**T12J**	0.78
R_c/H_s=0 H_s=0.2m	0.25	-0.15	**T13B**	2.01	**T13F**	1.86	**T13J**	1.94
			T14B	1.61	**T14F**	1.32	**T14J**	1.33
			T15B	1.93	**T15F**	1.92	**T15J**	1.97
			T16B	2.08	**T16F**	2.19	**T16J**	2.41
R_c/H_s=-1 H_s=0.1m	0.13	-0.05	**T1A**	1.23	**T1E**	1.39	**T1I**	1.33
			T2A	0.89	**T2E**	0.78	**T2I**	0.79
			T3A	1.33	**T3E**	1.23	**T3I**	1.25
			T4A	0.57	**T4E**	0.82	**T4I**	0.71
R_c/H_s=-1 H_s=0.2m	0.09	-0.02	**T5A**	4.96	**T5E**	4.92	**T5I**	4.93
			T6A	4.12	**T6E**	4.06	**T6I**	4.02
			T7A	4.10	**T7E**	4.07	**T7I**	4.09
			T8A	4.11	**T8E**	4.00	**T8I**	3.99

4.7 Statistical characterization of extreme overtopping wave volumes

In the design of coastal defences and in the estimate of their vulnerability a key aspect is the realistic prediction of the characteristics of the overtopping waves. In fact hydrodynamic forces on landward-side slopes largely depend on the distribution of instantaneous overtopping wave volumes, flow thicknesses and flow velocities (Van der Meer et al., 2010; Hughes et al., 2012). Overtopping wave volumes have been successfully approximated by a Weibull distribution, whose shape factor appears to be larger for very large overtopping and certainly for wave overtopping combined with overflow (Hughes and Nadal, 2009; Victor, et al., 2012). The larger shape factor results in lower maximum overtopping wave volumes.

The percent exceedance distribution of overtopping wave volumes is given by (Hughes et al., 2012):

$$P_{V\%}(V_i \geq V) = exp\left[-\left(\frac{V}{a}\right)^{b}\right] \tag{4.15}$$

where $P_{V\%}$ is the percentage of wave volumes that will exceed the specified volume (V_i). The two parameters of the Weibull distribution are the non-dimensional shape factor, b, that helps define the extreme tail of the distribution and the dimensional scale factor, a, that normalizes the distribution.

Hughes et al. 2012 valid the relationship of the Weibull shape factor b for smooth and impermeable structures like dikes and levees. The relationship is given as b versus R_c/H_{m0} to describe the distribution of overtopping wave volumes.

Zanuttigh et al. 2013 presents the analysis of the Weibull b-value for conventional rubble mound breakwaters as well as for low crested structures with the crest at or just above the water level. It is concluded that rubble mound structures show more scatter in the b-value than smooth impermeable structures and the combined data make even more sense

if the b-value is related to relative discharge instead of relative freeboard because the effects of slope angle and wave steepness are implicitly included.

In this analysis we compared our results with the new trend for the shape factor b found in Zanuttigh et al. 2013:

$$b = 0.73 + 55\left(\frac{q}{gH_{m0}T_{m-1,0}}\right)^{0.8} \tag{4.16}$$

and in the following Figures data for smooth structure, different submergence and seaward/landward steepness obtained by Hughes and Victor are reported.

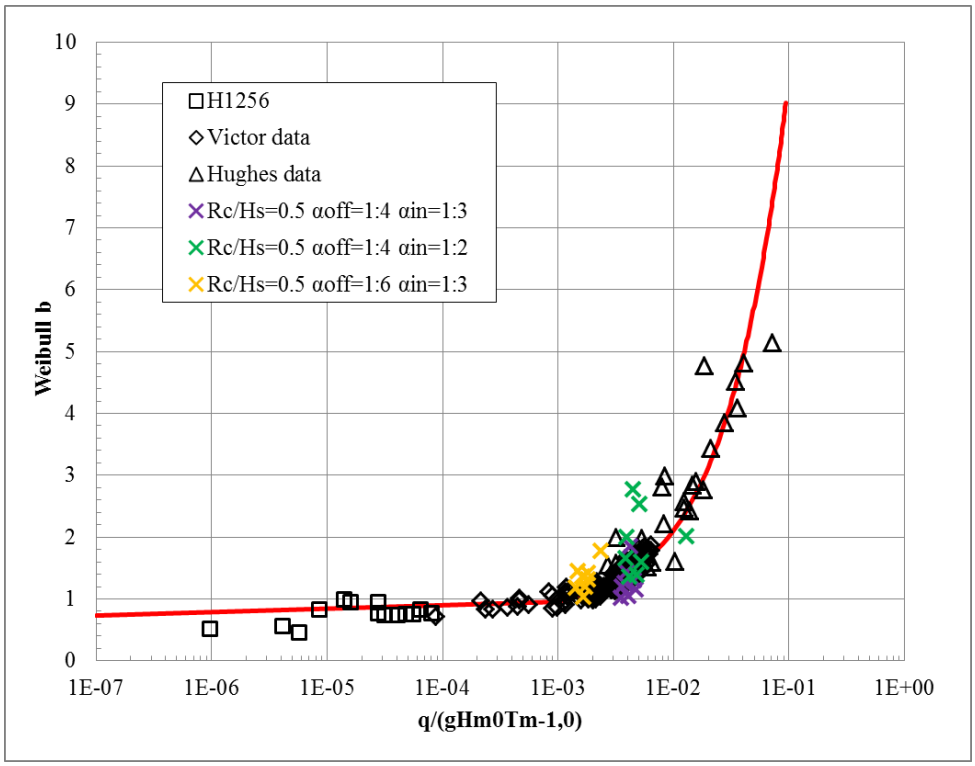

Figure 4.33. Comparison numerical results ($R_c/H_s = 0.5$) with smooth structures against formula 4.16.

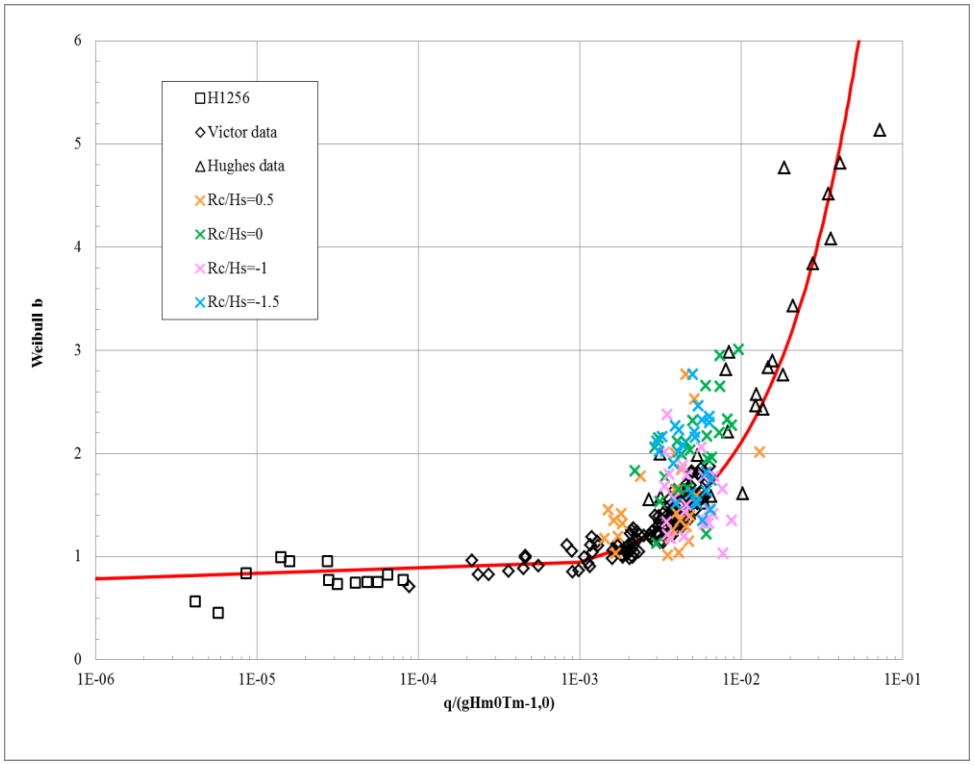

Figure 4.34. Comparison numerical results ($R_c/H_s = 0.5$, orange; $R_c/H_s = 0$, green; $R_c/H_s = -1$, pink; $R_c/H_s = -1.5$, blue) with smooth structures against formula 4.16.

CHAPTER 5

TWO-PHASE APPROACH FOR SEDIMENT TRANSPORT MODELLING.

The present chapter is devoted to the description of the modifications and improvements that have been made in the IH-2VOF code in order to implement the sediment transport. Most of these modifications have been carried out based on Hsu *et al.* 2004.

5.1 Governing equations for fluid and particle phase: RANS equations

Sediment transport involves a fluid phase and a particle phase. The fluid phase is water with mass density ρ^f and the particle phase is represented as a identical spheres of diameter d and mass density ρ^s. Assuming that the mixture can be treated as a continuum, the ensemble averaged two-phase equations of mass and momentum can be derived readily. In this averaging process, the definition of sediment concentration c is introduced. Because of the presence of the particle concentration, the two continuum phases are, essentially, compressible. For this reason, we implement Favre averaging (Favre 1965). For more details see Hsu *et al.* 2004.

The fluid and sediment phase continuity equations are:

$$\frac{\partial \rho_{fc}}{\partial t} + \frac{\partial \rho_{fc} u^f}{\partial x} + \frac{\partial \rho_{fc} v^f}{\partial y} = 0 \tag{5.1}$$

$$\frac{\partial \rho_{sc}}{\partial t} + \frac{\partial \rho_{sc} u^s}{\partial x} + \frac{\partial \rho_{sc} v^s}{\partial y} = 0 \tag{5.2}$$

where:

$$\rho_{fc} = \rho^f (1 - c) \tag{5.3}$$

and

$$\rho_{sc} = \rho^s c\,. \tag{5.4}$$

In these equations u^f and u^s represent, respectively, the *x*-components of the fluid and particle velocity and v^f and v^s the *y*-component of the fluid and particle velocity.
The *x*- and *y*- components of the fluid-phase momentum equations for the uniform flow can be expressed as:

$$\begin{aligned} &\frac{\partial \rho_{fc} u^f}{\partial t} + u^f \frac{\partial \rho_{fc} u^f}{\partial x} + v^f \frac{\partial \rho_{fc} u^f}{\partial y} = \\ &= -(1 - \bar{c}) \frac{\partial P}{\partial x} - \rho_{fc} g + \frac{\partial \tau_{xx}^f}{\partial x} + \frac{\partial \tau_{xy}^f}{\partial y} - \beta \bar{c} \left(u^f - u^s\right) + \beta \nu_{ft} \frac{\partial \bar{c}}{\partial x} \end{aligned} \tag{5.5}$$

and

$$\begin{aligned} &\frac{\partial \rho_{fc} v^f}{\partial t} + u^f \frac{\partial \rho_{fc} v^f}{\partial x} + v^f \frac{\partial \rho_{fc} v^f}{\partial y} = \\ &= -(1 - \bar{c}) \frac{\partial P}{\partial y} + \rho_{fc} g + \frac{\partial \tau_{yx}^f}{\partial x} + \frac{\partial \tau_{yy}^f}{\partial y} - \beta \bar{c} \left(v^f - v^s\right) + \beta \nu_{ft} \frac{\partial \bar{c}}{\partial x} \end{aligned} \tag{5.6}$$

where P is the fluid pressure, $\tau_{xx}^f, \tau_{xy}^f, \tau_{yx}^f, \tau_{yy}^f$ are the fluid phase stresses and g is the gravitational acceleration. The last two terms in equations (5.5) and (5.6) are the Favre averaged drag forces, with the drag coefficient β defined as:

$$\beta = \frac{\rho^f U_r}{d} \left(\frac{18.0}{Re_p} + 0.3 \right) \frac{1}{(1 - \bar{c})^n}. \tag{5.7}$$

In Eq. (5.7), Re_p is the particle Reynolds number and U_r is the magnitude of the relative velocity between the fluid and sediment phase:

$$Re_p = \frac{\rho^f U_r d}{\mu_f} \tag{5.8}$$

$$U_r = \sqrt{(u^f - u^s)^2 + (v^f - v^s)^2} \tag{5.9}$$

where μ_f is the fluid viscosity and n is a coefficient

$$n = 4.45 Re_p^{-1}, \quad 1 \leq Re_p < 500. \tag{5.10}$$

The concentration dependence in equation (5.7) is taken from the experimental results of Richardson and Zaki (1954). The drag force contribution in (5.5) and (5.6) is composed of two terms. The first is the averaged drag force due to the relative mean velocity between the two phases. The second, called fluid turbulent suspension, is the correlation between the concentration and the large-scale fluid velocity fluctuations. It is modelled here as a gradient transport (see McTigue, 1981).

The corresponding sediment-phase momentum equations are:

$$\begin{aligned} &\frac{\partial \rho_{sc} u^s}{\partial t} + u^s \frac{\partial \rho_{sc} u^s}{\partial x} + v^s \frac{\partial \rho_{sc} u^s}{\partial y} = \\ &= -\bar{c}\frac{\partial \bar{P}^f}{\partial x} - \rho_{sc} g + \frac{\partial \tau_{xx}^s}{\partial x} + \frac{\partial \tau_{xy}^s}{\partial y} + \beta \bar{c}\left(u^f - u^s\right) + \beta \nu_{ft} \frac{\partial \bar{c}}{\partial x} \end{aligned} \tag{5.11}$$

and

$$\begin{aligned} &\frac{\partial \rho_{sc} v^f}{\partial t} + u^s \frac{\partial \rho_{sc} v^s}{\partial x} + v^s \frac{\partial \rho_{sc} v^s}{\partial y} = \\ &= -\bar{c}\frac{\partial \bar{P}^f}{\partial y} + \rho_{sc} g + \frac{\partial \tau_{yx}^s}{\partial x} + \frac{\partial \tau_{yy}^s}{\partial y} + \beta \bar{c}\left(v^f - v^s\right) + \beta \nu_{ft} \frac{\partial \bar{c}}{\partial y} \end{aligned} \tag{5.12}$$

where $\tau_{xx}^s, \tau_{xy}^s, \tau_{yx}^s, \tau_{yy}^s$ are the stresses of the sediment phase, including the small-scale particle (inter-granular) stresses and the Reynolds stresses of the Favre averaged particle

velocities. Closures for fluid turbulence and sediment stresses are major issues of sheet flow modelling and are detailed in the next paragraph.

5.2 Closure of fluid stresses

Closures for fluid turbulence stresses in two-phase flows are very similar to the case of clear water, with the exception of the contribution of sediment - in terms of concentration and correlation between fluid and sediment velocities - in the governing equations for the turbulent kinetic energy and for the rate of turbulent energy dissipation.
The total stress of the fluid-phase in equation (5.5) and (5.6) can be written as:

$$\tau_{xx}^{f} = \tau_{xx}^{f0} + R_{xx}^{f} \tag{5.13}$$

$$\tau_{xy}^{f} = \tau_{xy}^{f0} + R_{xy}^{f} \tag{5.14}$$

$$\tau_{yy}^{f} = \tau_{yy}^{f0} + R_{yy}^{f} \tag{5.15}$$

$$\tau_{yx}^{f} = \tau_{yx}^{f0} + R_{yx}^{f} \tag{5.16}$$

where $\tau_{xx}^{f0}, \tau_{xy}^{f0}, \tau_{yx}^{f0}, \tau_{yy}^{f0}$ are the averaged small-scale stresses consisting of the viscous stress and the small-scale Reynolds stress of the turbulence generated in the fluid between the sediment particles or induced by fluctuations of the particles. The large-scale fluid Reynolds stresses, defined as the correlations between the concentration and fluid velocity fluctuations Δu^{f} and Δv^{f},

$$R_{xx}^{f} = -\rho^{f}\overline{(1-c)\Delta u^{f}\Delta u^{f}} \tag{5.17}$$

$$R_{xy}^{f} = -\rho^{f}\overline{(1-c)\Delta u^{f}\Delta v^{f}} \tag{5.18}$$

$$R_{yy}^{f} = -\rho^{f}\overline{(1-c)\Delta v^{f}\Delta v^{f}} \tag{5.19}$$

$$R_{yx}^{f} = -\rho^{f}\overline{(1-c)\Delta v^{f}\Delta u^{f}} \tag{5.20}$$

result from the Favre averaging process. They represent the transfer of momentum that occurs on the scale at which the concentration fluctuates.

The turbulent eddy viscosity hypothesis is used here to model the large-scale fluid Reynolds stresses:

$$\tau_{xy}^{f} = \rho^{f}\left(\nu_{ft} + \nu_{f}\right)\frac{\partial u^{f}}{\partial y} \tag{5.21}$$

$$\tau_{yx}^{f} = \rho^{f}\left(\nu_{ft} + \nu_{f}\right)\frac{\partial v^{f}}{\partial x} \tag{5.22}$$

and

$$\tau_{xx}^{f} = -\frac{2}{3}\rho_{c}k_{f} + \frac{4}{3}\rho^{f}\left(\nu_{ft} + \nu_{f}\right)\frac{\partial u^{f}}{\partial x} \tag{5.23}$$

$$\tau_{yy}^{f} = -\frac{2}{3}\rho_{c}k_{f} + \frac{4}{3}\rho^{f}\left(\nu_{ft} + \nu_{f}\right)\frac{\partial v^{f}}{\partial y} \tag{5.24}$$

where ν_f is the kinematic viscosity of the fluid and k_f is the fluid-phase turbulent kinetic energy, defined as

$$k_{f} = \frac{1}{2(1-c)}\overline{(1-c)\Delta u_{i}^{f}\Delta u_{i}^{f}}. \tag{5.25}$$

The second term on the right-hand side of equations (5.23) and (5.24) appears because the divergence of the fluid-phase velocity is not zero. We assume that the fluid phase eddy viscosity ν_{ft} is given by:

$$\nu_{ft} = C_\mu \frac{k_f^2(1-c)}{\varepsilon_f} \tag{5.26}$$

where C_μ is an empirical coefficient and

$$\varepsilon_f = \frac{1}{\rho_c}\overline{(1-c)\tau_{iJ}^f \frac{\partial \Delta u_i^f}{\partial x_j}} \tag{5.27}$$

is the fluid-phase turbulent dissipation rate. Because k_f and ε_f appear in the eddy viscosity, we need to introduce balance equations for both.

Following Hsu et al. (2004), the fluid phase turbulent kinetic energy equation in the uniform flow can be written as

$$\begin{aligned} &\frac{\partial \rho_c k_f}{\partial t} + u^f \frac{\partial \rho_c k_f}{\partial x} + v^f \frac{\partial \rho_c k_f}{\partial y} = \\ &= \tau_{xx}^f \frac{\partial u^f}{\partial x} + \tau_{yy}^f \frac{\partial v^f}{\partial y} + \tau_{xy}^f \frac{\partial u^f}{\partial y} + \tau_{yx}^f \frac{\partial v^f}{\partial x} + \\ &+ \frac{\partial}{\partial x}\left[\left(\nu_f + \frac{\nu_{ft}}{\sigma_k}\right)\frac{\partial \rho_c k_f}{\partial x}\right] + \frac{\partial}{\partial y}\left[\left(\nu_f + \frac{\nu_{ft}}{\sigma_k}\right)\frac{\partial \rho_c k_f}{\partial y}\right] - \rho_c \varepsilon_f + \\ &+ \beta \nu_f \frac{\partial \bar{c}}{\partial y}\left(v^f - v^s\right) - 2\rho^s \bar{c}\beta k_f(1-\alpha) + \beta \nu_{ft}\frac{\partial \bar{c}}{\partial x}\left(u^f - u^s\right). \end{aligned} \tag{5.28}$$

The last term in eq. (5.28), which originally involves correlations between fluctuations of fluid and sediment velocities, represents a dissipation mechanism for the turbulent energy, where α is a parameter that measures the degree of correlation between the fluid and sediment velocity fluctuations. It is determined by the relative magnitudes of a particle response time t_p, the time between collisions t_c, and the fluid turbulence time-scale t_L:

$$\alpha = \left(1 + \frac{t_p}{\min(t_L, t_c)}\right)^{-1} \tag{5.29}$$

The particle response time is defined as

$$t_p \equiv \frac{\rho^s}{\beta} \tag{5.30}$$

and it is a measure of the time needed to accelerate a single particle from rest to the velocity of surrounding fluid (Drew 1976). The time between collisions is estimated based on the mean free path l_c of colliding particles and the strength $k_s^{1/2}$ of sediment velocity fluctuations:

$$t_c = \frac{l_c}{k_s^{1/2}} \tag{5.31}$$

where

$$l_c = \frac{\sqrt{\pi} d}{24 c g_0(c)} \ . \tag{5.32}$$

The fluid turbulence time-scale is defined as (Elghobashi & Abou-Arab 1983)

$$t_L = 0.165 \frac{k_f}{\varepsilon_f}. \tag{5.33}$$

The rate of turbulent energy dissipation ε_f is assumed to be governed by an equation similar to that for a clear fluid (Elghobashi & Abou-Arab 1983):

$$\begin{gathered}
\frac{\partial \rho_c \varepsilon_f}{\partial t} + u^f \frac{\partial \rho_c \varepsilon_f}{\partial x} + v^f \frac{\partial \rho_c \varepsilon_f}{\partial y} = \\
= C_{1\varepsilon} \frac{\varepsilon_f}{k_f} \left(\tau_{xx}^{ft} \frac{\partial u^f}{\partial x} + \tau_{xy}^{ft} \frac{\partial u^f}{\partial y} + \tau_{yx}^{ft} \frac{\partial v^f}{\partial x} + \tau_{yy}^{ft} \frac{\partial v^f}{\partial y} \right) + \\
+ \frac{\partial}{\partial x} \left[\left(\nu_f + \frac{\nu_{ft}}{\sigma_\varepsilon} \right) \frac{\partial \rho_c \varepsilon_f}{\partial x} \right] + \frac{\partial}{\partial y} \left[\left(\nu_f + \frac{\nu_{ft}}{\sigma_\varepsilon} \right) \frac{\partial \rho_c \varepsilon_f}{\partial y} \right] - C_{2\varepsilon} \frac{\varepsilon_f}{k_f} \rho_c \varepsilon_f + \\
- C_{3\varepsilon} \frac{\varepsilon_f}{k_f} \left[2 \rho^s \bar{c} k_f \beta (1 - \alpha) \right] + C_{3\varepsilon} \frac{\varepsilon_f}{k_f} \left[\beta \nu_{ft} \frac{\partial \bar{c}}{\partial y} \left(v^f - v^s \right) \right] + \\
+ C_{3\varepsilon} \frac{\varepsilon_f}{k_f} \left[\beta \nu_{ft} \frac{\partial \bar{c}}{\partial x} \left(u^f - u^s \right) \right]
\end{gathered} \tag{5.34}$$

Due to the lack of information regarding the appropriate values of numerical coefficient in the present $k_f - \varepsilon_f$ model, we employ the same coefficients as those implemented in the standard $k - \varepsilon$ model for a clear fluid flow as already done by Hsu (see Hsu *et al*. 2004).

$$C_{1\varepsilon} = 1.44 \quad C_{2\varepsilon} = 1.92 \quad C_{3\varepsilon} = 1.2 \quad \sigma_\varepsilon = 1.3 \tag{5.35}$$

5.3 Closure of sediment stresses

In the sediment momentum equations, the two-scale averaging process results in a sediment stress, which can be written as

$$\tau_{xx}^s = \delta\tau_{xx}^{s0} + R_{xx}^s \tag{5.36}$$

$$\tau_{xy}^s = \delta\tau_{xy}^{s0} + R_{xy}^s \tag{5.37}$$

$$\tau_{yy}^s = \delta\tau_{yy}^{s0} + R_{yy}^s \tag{5.38}$$

$$\tau_{yx}^s = \delta\tau_{yx}^{s0} + R_{yx}^s \tag{5.39}$$

where $\tau_{xx}^{s0}, \tau_{xy}^{s0}, \tau_{yx}^{s0}, \tau_{yy}^{s0}$ are the mean particle shear and normal stresses due to small scale interactions, while $R_{xx}^s, R_{xy}^s, R_{yx}^s, R_{yy}^s$ are components of the large-scale sediment Reynolds stress.

The small-scale stresses $\tau_{xx}^{s0}, \tau_{xy}^{s0}, \tau_{yx}^{s0}, \tau_{yy}^{s0}$ are mainly due to granular interactions resulting from particle collisions or interstitial fluid effects. Here, we adopt the kinetic theory for collisional granular flow (Jenkins & Hanes 1998) for their closure.

Following this theory, the transport coefficients in the constitutive relations for $\tau_{xx}^{s0}, \tau_{xy}^{s0}, \tau_{yx}^{s0}, \tau_{yy}^{s0}$ are obtained from the kinetic theory of dense gases (Chapman & Cowling 1970). The particle normal and shear stresses due to collision are represented as:

$$\tau_{xx}^{s0} = -\frac{2}{3}\rho_{sc}(1+4G)K_s + AE\frac{\partial u^s}{\partial x} \tag{5.40}$$

$$\tau_{xy}^{s0} = \tau_{yx}^{s0} = AE\left(\frac{\partial u^s}{\partial y} + \frac{\partial v^s}{\partial x}\right) \tag{5.41}$$

$$\tau_{yy}^{s0} = -\frac{2}{3}\rho_{sc}(1+4G)K_s + AE\frac{\partial v^s}{\partial y} \tag{5.42}$$

where $G = cg_0(c)$, with $g_0(c)$ the radial distribution function at contact for identical spheres.

Torquato (1995) provides an accurate expression for this radial distribution function that is good for concentrations between 0.49, at which a phase transition between random and hexagonal packing is first possible, and the random close-packed concentration, $c^* = 0.635$, at which the mean distance between the edges' nearest neighbors is zero:

$$g_0(c) = \begin{cases} \dfrac{2-c}{2(1-c)^3} & if\ c < 0.49 \\ \dfrac{2-0.49}{2(1-0.49)^3}\dfrac{0.69-0.49}{(0.69-c)^p} & if\ 0.49 \le c \le 0.635 \end{cases} \tag{5.43}$$

where $p = 1$.

The product AE in eq. (5.40) and (5.42) is the sediment viscosity due to collisions and we have:

$$A = \frac{8d\rho^s\bar{c}G\left(\frac{2}{3}K_s\right)^{1/2}}{5\pi^{1/2}} \tag{5.44}$$

$$E = 1 + \frac{\pi}{12}\left(1 + \frac{5}{8G}\right)^2. \tag{5.45}$$

We model the large-scale sediment Reynolds stresses $R_{xx}^s, R_{xy}^s, R_{yx}^s, R_{yy}^s$ using an eddy viscosity. The shear stresses are written as

$$R_{xy}^s = R_{yx}^s = -\rho^s \sqrt{c\Delta u^s \Delta v^s} = \rho^s \nu_{st} \left(\frac{\partial u^s}{\partial y} + \frac{\partial v^s}{\partial x} \right) \tag{5.46}$$

and the normal stresses as

$$R_{xx}^s = -\rho^s \sqrt{c\Delta u^s \Delta u^s} = -\frac{2}{3}\rho_{sc} K_s + \frac{4}{3}\rho^s \nu_{st} \frac{\partial u^s}{\partial x} \tag{5.47}$$

$$R_{yy}^s = -\rho^s \sqrt{c\Delta v^s \Delta v^s} = -\frac{2}{3}\rho_{sc} K_s + \frac{4}{3}\rho^s \nu_{st} \frac{\partial v^s}{\partial y}. \tag{5.48}$$

The sediment viscosity ν_{st} is related to the sediment fluctuation energy through a sediment mixing length l_s,

$$\nu_{st} = C_s c l_s \sqrt{K_s} \tag{5.49}$$

where C_s is a numerical coefficient, assumed to be equal to 0.55 based on the value used in the one-equation turbulence model for clear fluid. We assume that the sediment mixing length can be related to the turbulent fluid flow mixing length l_f through α,

$$l_s = \alpha l_f \tag{5.50}$$

α is a parameter that measures the degree of correlation between the fluid and sediment velocity fluctuations. It is determined by the relative magnitudes of a particle response time.

The fluid turbulent mixing length is calculated from the fluid turbulent kinetic energy and its dissipation rate:

$$l_f = 0.165 \frac{k_f^{3/2}}{\varepsilon_f} \tag{5.51}$$

For massive particles with a long particle response time, $\alpha \approx 0$, the fluid turbulent eddies cannot induce any sediment velocity fluctuations, and $l_s \approx 0$. For fine particles with small particle response time, $\alpha \approx 1.0$, the fine particles follow the turbulent eddies, and $l_s \approx l_f$.

The kinetic theory of dense gases is based on the fundamental assumption of a significant number of collisions. Therefore, when the sediment concentration becomes very dilute, the validity of the collisional grain flow theory becomes questionable. Therefore, we introduce a damping parameter δ for the small-scale sediment stress defined in terms of the mean free path l_c of the sediment particles and the fluid turbulent mixing length l_f,

$$\delta = \frac{l_f}{l_f + l_c}. \tag{5.52}$$

When the mean free path of collision becomes much larger than the fluid turbulent mixing length, the small-scale collisional transport is reduced through a diminishing δ.

The constitutive relations for particle collisions based on the kinetic theory of dense molecular gases have been successfully implemented to study problems of rapid granular flow at concentrations smaller than the random loose packing c_*. The primary reason for the close similarity between particle and molecular collisions is that they are of relatively short duration, compared with the time between collisions. However, for granular shearing flows at concentrations greater than c_*, particles are in enduring contact. Therefore, the analogy between the particles and molecules is no longer valid.

Here, we model the sediment transport above the stationary bed, where the concentration is near random close packing. Therefore, modifications to the collisional grain flow theory for the closure of particle stress are needed. The discrete particle simulations of Zhang & Campbell (1992) indicate that between the random close-packed concentration c^* and the random loose-packed concentration c_*, the granular material is in a transitional state between solid-like and fluid-like behavior. Bocquet et al . (2001) carried out experiments on the Couette flow of grains in this regime and observed that the viscosity of the particle shear stress increased dramatically as the concentration approached c^*. They suggested that in the viscosity, the power p in equation (33) should be changed

from 1.00 to 1.75. That is, in our numerical implementation, p is taken to be 1.00 when $c < c^*$ and 1.75 when $c \geq c_*$. Therefore, as far as the particle shear stress is concerned, the region involving enduring contacts is modelled by taking the granular material to be an extremely viscous fluid. As the concentration increases above c^*, the collisional contribution to the particle normal stress diminishes, because the shearing of the particle phase that is the source of the collisional fluctuations becomes very small. However, in this range of concentration, the contribution to particle normal stress due to enduring contacts becomes important. Therefore, we further assume that the small-scale particle normal stress τ_{xx}^{s0} and τ_{yy}^{s0} is the sum of the collisional normal stress (τ_{xx}^{sc} and τ_{yy}^{sc}) and the normal stress (τ_{xx}^{se} and τ_{yy}^{se}) due to enduring contact:

$$\tau_{xx}^{s0} = \tau_{xx}^{sc} + \tau_{xx}^{se} \tag{5.53}$$

$$\tau_{yy}^{s0} = \tau_{yy}^{sc} + \tau_{yy}^{se}. \tag{5.54}$$

We model the collisional stress using equations (12) and (14), while for the normal stress due to enduring contacts we adopt a Hertz contact relation. For a homogeneously packed, dry granular material consisting of identical spheres in Hertzian contact, the normal stress is (Jenkins et al . 1989)

$$\tau_{xx}^{se} = \tau_{yy}^{se} = \frac{m}{\pi d^2} Kc \left(\frac{\Delta}{d}\right)^{\frac{3}{2}} \tag{5.55}$$

where Δ is the average compressive volume strain, m is given in terms of the shear modulus μ e and Poisson's ratio ν of the material of the particles

$$m = \frac{2}{9\sqrt{3}} \frac{\mu_e d^2}{1-\upsilon} \tag{5.56}$$

and K is the average number of contacts per particle or coordination number. We do not solve Eq. (5.50) for Δ, but assume that Δ/d can be related to the difference between the local average concentration and that of random loose-packing c^* by

$$\frac{\Delta}{d} = (c - c_*)^{2\chi/3} \tag{5.57}$$

in which χ is a coefficient. Based on numerical experiments for plastic particles implement ted by Sumer et al . (1996), $\chi = 5.5$ gives a failure concentration of ca. 62%. Therefore, this value is adopted.

Then

$$\tau_{xx}^{se} = \tau_{yy}^{se} = \begin{cases} 0, & c < c_* \\ \dfrac{m}{\pi d^2} K(c) c (c - c_*)^{\chi}, & c_* \le c \le c^* \end{cases} \tag{5.58}$$

where the coordination number K is taken to be a function of concentration.

$$K(\bar{c}) = 3 + 3sin\left[\frac{\pi}{2}\left(2\frac{\bar{c} - c_*}{c^* - c_*} - 1\right)\right] \quad for\ c_* \le \bar{c} \le c^* \tag{5.59}$$

Because K_s appears both in the sediment viscosity ν_{st} and in the normal-shear stresses, we need to introduce the transport equation for it (see Hsu 2002).

$$\begin{aligned} &\frac{\partial \rho_{sc} K_s}{\partial t} + u^s \frac{\partial \rho_{sc} K_s}{\partial x} + v^s \frac{\partial \rho_{sc} K_s}{\partial y} = \tau_{xx}^s \frac{\partial u^s}{\partial x} + \tau_{yy}^s \frac{\partial v^s}{\partial y} + \\ &+\tau_{xy}^s \frac{\partial u^s}{\partial y} + \tau_{yx}^s \frac{\partial v^s}{\partial x} - \frac{\partial Q}{\partial y} - \frac{\partial Q}{\partial x} - \gamma + 2\beta\bar{c}\left(\alpha k_f - K_s\right) \end{aligned} \tag{5.60}$$

with Q the flux of the fluctuation energy and γ the dissipation. The last term in the above equation describes the interaction between the two phases. Therefore, there is an additional source term, $2\beta\bar{c}\alpha k_f$, due to the fluid turbulent kinetic energy. This term models the influence of fluid turbulent eddies on the random motions of sediment particles and permits turbulent eddies to enhance the sediment fluctuation energy.

Moreover, an additional dissipation mechanism, $2\beta\bar{c}K_s$, also appears due to the drag of the interstitial fluid.

The flux of sediment fluctuation energy Q is taken to be the sum of the small-scale Q_0 and the large-scale Q_1 components:

$$Q = \delta Q_0 + Q_1 \tag{5.61}$$

where:

$$Q_0 = -\frac{5}{3} AM \left(\frac{\partial K_s}{\partial y} + \frac{\partial K_s}{\partial x} \right) \tag{5.62}$$

and

$$Q_1 = -\rho^s \frac{\nu_{st}}{\sigma_s} \left(\frac{\partial K_s}{\partial y} + \frac{\partial K_s}{\partial x} \right) \tag{5.63}$$

being σ_s a numerical coefficient (1.0).

Based on the kinetic theory for collisional granular flow, M in eq. (5.57) is:

$$M = 1 + \frac{9\pi}{32} \left(1 + \frac{5\pi}{12G} \right)^2 \tag{5.64}$$

Finally, we take the dissipation rate γ in equation (5.60) to be the collisional dissipation associated with the inelasticity of the particles. Based on the analysis of Jenkins & Savage (1983), and considering e as the coefficient of restitution (0.8), we can write:

$$\gamma = \left[\frac{10A}{d^2} - 4\rho^s \bar{c} G \left(\frac{\partial u^s}{\partial x} + \frac{\partial v^s}{\partial y} \right) \right] (1 - e) k_s \tag{5.65}$$

5.4 Model implementation

In order to solve the RANS equations both for fluid and sediment phase a method very similar to the two-step projection method used in the original IH-2VOF has been implemented. In the follow the method is described in detail.

1. An intermediate velocity both for fluid and sediment phase is introduced. These velocities ($\tilde{u}^f$, $\tilde{v}^f$, $\tilde{u}^s$, $\tilde{v}^s$) does not, in general, satisfy the continuity equation and derive from the momentum equation without the pressure gradient term.
   For the x-direction is possible write

$$\frac{\left(\tilde{u}^f\right)^{n+1}-\left(u^f\right)^n}{\Delta t}=-\left(u^f\right)^n\frac{\partial\left(u^f\right)^n}{\partial x}-\left(v^f\right)^n\frac{\partial\left(u^f\right)^n}{\partial y}+$$
$$-\frac{\left(u^f\right)^n}{\rho_{fc}^n}\left[\left(u^f\right)^n\frac{\partial\rho_{fc}^n}{\partial x}+\left(v^f\right)^n\frac{\partial\rho_{fc}^n}{\partial y}\right]+\frac{1}{\rho_{fc}^n}\left[\frac{\partial\left(\tau_{xx}^f\right)^n}{\partial x}+\frac{\partial\left(\tau_{xy}^f\right)^n}{\partial y}\right]+ \tag{5.66}$$
$$-g_x-\frac{\beta^n}{\rho_{fc}^n}\left[c^n\left(\left(u^f\right)^n-\left(u^s\right)^n\right)-v_{ft}^n\frac{\partial c^n}{\partial x}\right]$$

$$\frac{\left(\tilde{u}^s\right)^{n+1}-\left(u^s\right)^n}{\Delta t}=-\left(u^s\right)^n\frac{\partial\left(u^s\right)^n}{\partial x}-\left(v^s\right)^n\frac{\partial\left(u^s\right)^n}{\partial y}+$$
$$-\frac{\left(u^s\right)^n}{\rho_{sc}^n}\left[\left(u^f\right)^n\frac{\partial\rho_{sc}^n}{\partial x}+\left(v^s\right)^n\frac{\partial\rho_{sc}^n}{\partial y}\right]+\frac{1}{\rho_{sc}^n}\left[\frac{\partial\left(\tau_{xx}^s\right)^n}{\partial x}+\frac{\partial\left(\tau_{xy}^s\right)^n}{\partial y}\right]+ \tag{5.67}$$
$$-g_x-\frac{\beta^n}{\rho_{sc}^n}\left[c^n\left(\left(u^f\right)^n-\left(u^s\right)^n\right)-v_{st}^n\frac{\partial c^n}{\partial x}\right]$$

   and for the y-direction

$$\frac{\left(\tilde{v}^f\right)^{n+1}-\left(v^f\right)^n}{\Delta t}=-\left(u^f\right)^n\frac{\partial\left(v^f\right)^n}{\partial x}-\left(v^f\right)^n\frac{\partial\left(v^f\right)^n}{\partial y}+$$
$$-\frac{\left(v^f\right)^n}{\rho_{fc}^n}\left[\left(u^f\right)^n\frac{\partial\rho_{fc}^n}{\partial x}+\left(v^f\right)^n\frac{\partial\rho_{fc}^n}{\partial y}\right]+\frac{1}{\rho_{fc}^n}\left[\frac{\partial\left(\tau_{yx}^f\right)^n}{\partial x}+\frac{\partial\left(\tau_{yy}^f\right)^n}{\partial y}\right]+ \tag{5.68}$$
$$+g_y-\frac{\beta^n}{\rho_{fc}^n}\left[c^n\left(\left(v^f\right)^n-\left(v^s\right)^n\right)-v_{ft}\frac{\partial c^n}{\partial y}\right]$$

$$\frac{(\tilde{v}^s)^{n+1}-(v^s)^n}{\Delta t}=-(u^s)^n\frac{\partial(v^s)^n}{\partial x}-(v^s)^n\frac{\partial(v^s)^n}{\partial y}+$$
$$-\frac{(v^s)^n}{\rho_{sc}^n}\left[(u^s)^n\frac{\partial\rho_{sc}^n}{\partial x}+(v^s)^n\frac{\partial\rho_{sc}^n}{\partial y}\right]+\frac{1}{\rho_{sc}^n}\left[\frac{\partial\left(\tau_{yx}^s\right)^n}{\partial x}+\frac{\partial\left(\tau_{yy}^s\right)^n}{\partial y}\right] \tag{5.69}$$
$$+g_y-\frac{\beta^n}{\rho_{sc}^n}\left[c^n\left(\left(v^f\right)^n-\left(v^s\right)^n\right)-v_{st}\frac{\partial c^n}{\partial y}\right]$$

2. The next step is to project the intermediate velocity field into a divergence free plane to obtain the final velocity. In x-direction we have

$$\frac{\rho_{fc}^n\left(u^f\right)^{n+1}-\rho_{fc}^n\left(\tilde{u}^f\right)^{n+1}}{\Delta t}=-(1-c^n)\frac{\partial P^{n+1}}{\partial x} \tag{5.70}$$

and in y- direction

$$\frac{\rho_{fc}^n\left(v^f\right)^{n+1}-\rho_{fc}^n\left(\tilde{v}^f\right)^{n+1}}{\Delta t}=-(1-c^n)\frac{\partial P^{n+1}}{\partial y}. \tag{5.71}$$

Combining (5.70) and (5.71) with the continuity equation (5.72)

$$\frac{\partial\rho_{fc}}{\partial t}+\frac{\partial\rho_{fc}^n\left(u^f\right)^{n+1}}{\partial x}+\frac{\partial\rho_{fc}^n\left(v^f\right)^{n+1}}{\partial y}=0 \tag{5.72}$$

the Poisson Pressure Equation (PPE) for the two-phase approach is obtained:

$$\frac{\partial}{\partial x}\left((1-c^n)\frac{\partial P^{n+1}}{\partial x}\right)+\frac{\partial}{\partial y}\left((1-c^n)\frac{\partial P^{n+1}}{\partial y}\right)=\frac{\rho_{fc}^n-\rho_{fc}^{n-1}}{\Delta t^2}+ \\ +\frac{\rho_{fc}^n}{\Delta t}\left[\frac{\partial\left(\tilde{u}^f\right)^{n+1}}{\partial x}+\frac{\partial\left(\tilde{v}^f\right)^{n+1}}{\partial y}\right]+\frac{\left(\tilde{u}^f\right)^{n+1}}{\Delta t}\frac{\partial\rho_{fc}^n}{\partial x}+\frac{\left(\tilde{v}^f\right)^{n+1}}{\Delta t}\frac{\partial\rho_{fc}^n}{\partial y} \tag{5.73}$$

By solving (5.73) with the appropriate boundary conditions, the correct pressure information at the n+1-th time step will be obtained.

3. Substituting the updated pressure information into (5.70) and (5.71), the new velocity field for the fluid at the n+1-th time step, which satisfies the continuity equation, is obtained. In the same way, by substituting the updated pressure information into the following equations

$$\frac{\rho_{sc}^n(u^s)^{n+1}-\rho_{sc}^n(\tilde{u}^s)^{n+1}}{\Delta t}=-(1-c^n)\frac{\partial P^{n+1}}{\partial x} \tag{5.74}$$

$$\frac{\rho_{sc}^n(v^s)^{n+1}-\rho_{sc}^n(\tilde{v}^s)^{n+1}}{\Delta t}=-(1-c^n)\frac{\partial P^{n+1}}{\partial y} \tag{5.75}$$

also the new velocity field for the sediment at the n+1-th time step is obtained.

4. Finally, the new value of the concentration can be calculated on the base of the continuity equation of the sediment phase at the n+1-th time step.

$$\frac{\partial\rho_{sc}}{\partial t}+\frac{\partial\rho_{sc}^n(u^s)^{n+1}}{\partial x}+\frac{\partial\rho_{sc}^n(v^s)^{n+1}}{\partial y}=0 \tag{5.76}$$

$$c^{n+1}=\frac{\rho_{sc}^{n+1}}{\rho^f f^{n+1}} \tag{5.77}$$

5.5 Spatial discretization in finite different form

In the equations presented in the previous paragraph, spatial derivatives need to be specified. The nonlinear advection terms are discretized by using a combination of the upwind scheme and the central difference scheme to achieve an accurate numerical solution. The central difference method is employed to discretize the pressure gradient terms and stress gradient terms. Introducing the discretization of spatial derivatives into the Poisson pressure equation yields a set of linear algebraic equations for the pressure field that is solved using conjugate gradient method with the preconditioned of incomplete Cholesky decomposition.

Stability of finite difference scheme is performed by Heuristic analysis. Implicit discretization of the pressure term in the momentum equation leads to a linear system of equations that needs considerable computational effort to be solved. However this kind of discretization avoids any stability condition related to pressure term. On the other hand, the explicit discretization of the advection and diffusion terms in the momentum equation leading to a time step constraints such that

$$\Delta t \leq min\left\{\frac{\alpha\Delta x}{|u|}, \frac{\alpha\Delta y}{|v|}\right\} \tag{5.78}$$

$$\Delta t \leq min\left\{\frac{\Delta x^2}{6(v_t + v)}, \frac{\Delta y^2}{6(v_t + v)}\right\} \tag{5.79}$$

are required.

The scheme implemented in the two-phase approach, as in the original IH-2VOF, is a finite-different scheme. As shown in Figure 3.1, the scheme calculates the velocity components of the fluid/sediment, u^f/u^s and v^f/v^s, on the vertical and horizontal cell faces, respectively, whereas the pressure and other scalars such k^f, ε^f, the volume of fluid function F and the sediment concentration c, are defined at the cell center.

It is noted that in the finite difference form, some variables are needed at the place where they are not originally defined, for example, the horizontal velocity at the top face of the cell or the vertical velocity at the right face of the cell. In such circumstances, the linear interpolation is used. In the follow the most commonly used interpolation variables are

given and it is not specified the superscript f or s because the interpolation is the same both for the fluid phase and the sediment phase.

$$u_{i,j} = \frac{1}{2}\left(u_{i+\frac{1}{2},j} + u_{i-\frac{1}{2},j}\right) \tag{5.80}$$

$$v_{i,j} = \frac{1}{2}\left(v_{i,j+\frac{1}{2}} + v_{i,j-\frac{1}{2}}\right) \tag{5.81}$$

$$u_{i,j+\frac{1}{2}} = \frac{u_{i,j+1}\Delta y_j + u_{i,j}\Delta y_{j+1}}{\Delta y_j + \Delta y_{j+1}} \tag{5.82}$$

$$v_{i+\frac{1}{2},j} = \frac{u_{i+1,j}\Delta x_i + u_{i,j}\Delta x_{i+1}}{\Delta x_i + \Delta x_{i+1}} \tag{5.83}$$

$$\rho_{i+\frac{1}{2},j} = \frac{\rho_{i+1,j}\Delta x_i + \rho_{i,j}\Delta x_{i+1}}{\Delta x_i + \Delta x_{i+1}} \tag{5.84}$$

$$\rho_{i,j+\frac{1}{2}} = \frac{\rho_{i,j+1}\Delta y_j + \rho_{i,j}\Delta y_{j+1}}{\Delta y_j + \Delta y_{j+1}} \tag{5.85}$$

$$\Delta x_{i+\frac{1}{2}} = \frac{1}{2}(\Delta x_i + \Delta x_{i+1}) \tag{5.86}$$

$$\Delta y_{j+\frac{1}{2}} = \frac{1}{2}\left(\Delta y_j + \Delta y_{j+1}\right) \tag{5.87}$$

5.5.1 Advection terms

Both for sediment and fluid equations, in equations (5.66), (5.67), (5.68) and (5.69) all the advection terms will be evaluated at the n-th time step. The advection terms in the x-momentum equation $u\frac{\partial u}{\partial x}+v\frac{\partial u}{\partial y}$ are evaluated at the right face of the cell. The advection terms in the y-momentum equation $u\frac{\partial v}{\partial x}+v\frac{\partial v}{\partial y}$ are evaluated at the top face of the cell.

$$u\frac{\partial u}{\partial x}+v\frac{\partial u}{\partial y}=u_{i+\frac{1}{2},j}\left(\frac{\partial u}{\partial x}\right)_{i+\frac{1}{2},j}+v_{i+\frac{1}{2},j}\left(\frac{\partial u}{\partial y}\right)_{i+\frac{1}{2},j} \tag{5.88}$$

$$u\frac{\partial v}{\partial x}+v\frac{\partial v}{\partial y}=u_{i,j+\frac{1}{2}}\left(\frac{\partial v}{\partial x}\right)_{i,j+\frac{1}{2}}+v_{i,j+\frac{1}{2}}\left(\frac{\partial v}{\partial y}\right)_{i,j+\frac{1}{2}}. \tag{5.89}$$

As in Lin and Liu (1998), also here to calculate the spatial derivatives of the velocity the combination of the upwind scheme and the central difference scheme is used. The upwind scheme is represented by

$$\left(\frac{\partial u}{\partial x}\right)_{i+\frac{1}{2},j}=\begin{cases}\left(\frac{\partial u}{\partial x}\right)_{i+1,j} & if\ u_{i+\frac{1}{2},j}<0\\ \left(\frac{\partial u}{\partial x}\right)_{i,j} & if\ u_{i+\frac{1}{2},j}>0\end{cases} \tag{5.90}$$

and the center difference scheme is represented by

$$\left(\frac{\partial u}{\partial x}\right)_{i+\frac{1}{2},j}=\frac{\left(\frac{\partial u}{\partial x}\right)_{i+1,j}\Delta x_i+\left(\frac{\partial u}{\partial x}\right)_{i,j}\Delta x_{i+1}}{\Delta x_i+\Delta x_{i+1}}. \tag{5.91}$$

In both (5.90) and (5.91)

$$\left(\frac{\partial u}{\partial x}\right)_{i+1,j} = \frac{u_{i+\frac{3}{2},j} - u_{i+\frac{1}{2},j}}{\Delta x_{i+1}} \tag{5.92}$$

$$\left(\frac{\partial u}{\partial x}\right)_{i,j} = \frac{u_{i+\frac{1}{2},j} - u_{i-\frac{1}{2},j}}{\Delta x_{i}} \tag{5.93}$$

are defined. Since the upwind scheme usually introduces significant numerical damping and the central difference scheme generates numerical instability, a combination of these two schemes usually yields a more accurate numerical solution. Thus, the general formula for the spatial derivative becomes

$$\left(\frac{\partial u}{\partial x}\right)_{i+\frac{1}{2},j} = \\ = \frac{\left[1 + \alpha sgn\left(u_{i+\frac{1}{2},j}\right)\right]\left(\frac{\partial u}{\partial x}\right)_{i,j}\Delta x_{i+1} + \left[1 - \alpha sgn\left(u_{i+\frac{1}{2},j}\right)\right]\left(\frac{\partial u}{\partial x}\right)_{i+1,j}\Delta x_i}{\Delta x_i + \Delta x_{i+1} + \alpha sgn\left(u_{i+\frac{1}{2},j}\right)(\Delta x_{i+1} - \Delta x_i)} \tag{5.94}$$

and similarly

$$\left(\frac{\partial u}{\partial y}\right)_{i+\frac{1}{2},j} = \\ = \frac{\left[1 + \alpha sgn\left(v_{i+\frac{1}{2},j}\right)\right]\left(\frac{\partial u}{\partial y}\right)_{i+\frac{1}{2},j-\frac{1}{2}}\Delta y_{j+\frac{1}{2}} + \left[1 - \alpha sgn\left(v_{i+\frac{1}{2},j}\right)\right]\left(\frac{\partial u}{\partial y}\right)_{i+\frac{1}{2},j+\frac{1}{2}}\Delta y_j}{\Delta y_{j+\frac{1}{2}} + \Delta y_{j-\frac{1}{2}} + \alpha sgn\left(v_{i+\frac{1}{2},j}\right)\left(\Delta y_{j+\frac{1}{2}} - \Delta y_{j-\frac{1}{2}}\right)} \tag{5.95}$$

where

$$\left(\frac{\partial u}{\partial y}\right)_{i+\frac{1}{2},j+\frac{1}{2}} = \frac{u_{i+\frac{1}{2},j+1} - u_{i+\frac{1}{2},j}}{\Delta y_{j+\frac{1}{2}}} \tag{5.96}$$

and

$$\left(\frac{\partial u}{\partial y}\right)_{i+\frac{1}{2},j-\frac{1}{2}} = \frac{u_{i+\frac{1}{2},j} - u_{i+\frac{1}{2},j-1}}{\Delta y_{j-\frac{1}{2}}}. \tag{5.97}$$

For the advection terms in the y-direction we have to define the following derivatives:

$$\left(\frac{\partial v}{\partial x}\right)_{i,j+\frac{1}{2}} =$$

$$= \frac{\left[1+\alpha sgn\left(u_{i,j+\frac{1}{2}}\right)\right]\left(\frac{\partial v}{\partial x}\right)_{i+\frac{1}{2},j+\frac{1}{2}} \Delta x_{i-\frac{1}{2}} + \left[1-\alpha sgn\left(u_{i,j+\frac{1}{2}}\right)\right]\left(\frac{\partial v}{\partial x}\right)_{i-\frac{1}{2},j+\frac{1}{2}} \Delta x_i}{\Delta x_{i-\frac{1}{2}} + \Delta x_{i+\frac{1}{2}} + \alpha sgn\left(u_{i,j+\frac{1}{2}}\right)\left(\Delta x_{i-\frac{1}{2}} - \Delta x_{i+\frac{1}{2}}\right)} \tag{5.98}$$

and

$$\left(\frac{\partial v}{\partial y}\right)_{i,j+\frac{1}{2}} =$$

$$= \frac{\left[1+\alpha sgn\left(v_{i,j+\frac{1}{2}}\right)\right]\left(\frac{\partial v}{\partial y}\right)_{i,j} \Delta y_{j+1} + \left[1-\alpha sgn\left(v_{i,j+\frac{1}{2}}\right)\right]\left(\frac{\partial v}{\partial y}\right)_{i,j+1} \Delta y_j}{\Delta y_{j+1} + \Delta y_j + \alpha sgn\left(v_{i,j+\frac{1}{2}}\right)\left(\Delta y_{j+1} - \Delta y_j\right)} \tag{5.99}$$

where

$$\left(\frac{\partial v}{\partial x}\right)_{i+\frac{1}{2},j+\frac{1}{2}} = \frac{v_{i+1,j+\frac{1}{2}} - v_{i,j+\frac{1}{2}}}{\Delta x_{i+\frac{1}{2}}} \tag{5.100}$$

$$\left(\frac{\partial v}{\partial x}\right)_{i-\frac{1}{2},j+\frac{1}{2}} = \frac{v_{i,j+\frac{1}{2}} - v_{i-1,j+\frac{1}{2}}}{\Delta x_{i-\frac{1}{2}}} \tag{5.101}$$

$$\left(\frac{\partial v}{\partial y}\right)_{i,j} = \frac{v_{i,j+\frac{1}{2}} - v_{i,j-\frac{1}{2}}}{\Delta y_j} \tag{5.102}$$

$$\left(\frac{\partial v}{\partial y}\right)_{i,j+1} = \frac{v_{i,j+\frac{3}{2}} - v_{i,j+\frac{1}{2}}}{\Delta y_{j+1}} \tag{5.103}$$

In the above equations, the coefficient α is the weighing factor between the up-wind method and the central difference method. When $\alpha = 0$, the finite difference form becomes the central difference; while when $\alpha = 1$, the finite difference form becomes the upwind difference. In practice, α is generally selected in the range of 0.3 to 0.5 to produce the stable and accurate results.

In the x-direction is also necessary to define

$$v_{i+\frac{1}{2},j} = \frac{\left(v_{i+1,j+\frac{1}{2}} + v_{i+1,j-\frac{1}{2}}\right)\Delta x_i + \left(v_{i,j+\frac{1}{2}} + v_{i,j-\frac{1}{2}}\right)\Delta x_{i+1}}{2(\Delta x_i + \Delta x_{i+1})} \tag{5.104}$$

and in the y-direction

$$u_{i,j+\frac{1}{2}} = \frac{\left(u_{i+\frac{1}{2},j+1} + u_{i+\frac{1}{2},j+1}\right)\Delta y_j + \left(u_{i+\frac{1}{2},j} + u_{i+\frac{1}{2},j}\right)\Delta y_{j+1}}{2\left(\Delta y_j + \Delta y_{j+1}\right)} \ . \tag{5.105}$$

5.5.2 New advection terms

Since the sediment presence, the density is not constant. Therefore, in equations (5.66), (5.67), (5.68) and (5.69) new terms appears. These terms will be evaluated at the n-th time step. In the x-momentum equation the new term is $\frac{u}{\rho}\left(u\frac{\partial \rho}{\partial x} + v\frac{\partial \rho}{\partial y}\right)$ and has to be evaluated at the right face of the cell. In the y-momentum equation the new term is $\frac{v}{\rho}\left(u\frac{\partial \rho}{\partial x} + v\frac{\partial \rho}{\partial y}\right)$ and has to be evaluated at the top face of the cell.

For the -x and -y direction we have respectively:

$$\frac{u_{i+\frac{1}{2},j}}{\rho_{i+\frac{1}{2},j}}\left[u_{i+\frac{1}{2},j}\left(\frac{\partial\rho}{\partial x}\right)_{i+\frac{1}{2},j}+v_{i+\frac{1}{2},j}\left(\frac{\partial\rho}{\partial y}\right)_{i+\frac{1}{2},j}\right] \tag{5.106}$$

$$\frac{u_{i+\frac{1}{2},j}}{\rho_{i+\frac{1}{2},j}}\left[u_{i+\frac{1}{2},j}\left(\frac{\partial\rho}{\partial x}\right)_{i+\frac{1}{2},j}+v_{i+\frac{1}{2},j}\left(\frac{\partial\rho}{\partial y}\right)_{i+\frac{1}{2},j}\right] \tag{5.107}$$

where

$$\rho_{i+\frac{1}{2},j}=\frac{\rho_{i+1,j}\Delta x_i+\rho_{i,j}\Delta x_{i+1}}{\Delta x_i+\Delta x_{i+1}} \tag{5.108}$$

$$\rho_{i,j+\frac{1}{2}}=\frac{\rho_{i,j+1}\Delta y_j+\rho_{i,j}\Delta y_{j+1}}{\Delta y_j+\Delta y_{j+1}} \tag{5.109}$$

$$\left(\frac{\partial\rho}{\partial x}\right)_{i+\frac{1}{2},j}=\frac{\rho_{i+1,j}-\rho_{i,j}}{\Delta x_{i+\frac{1}{2}}} \tag{5.110}$$

$$\begin{aligned}\left(\frac{\partial\rho}{\partial y}\right)_{i+\frac{1}{2},j}&=\frac{1}{\Delta y_j+\Delta y_{j+1}}\left(\frac{\rho_{i+1,j+1}\Delta x_i+\rho_{i,j+1}\Delta x_{i+1}}{\Delta x_i+\Delta x_{i+1}}\right)+\\&+\frac{\Delta y_{j+1}-\Delta y_{j-1}}{(\Delta y_j+\Delta y_{j+1})(\Delta y_j+\Delta y_{j-1})}\left(\frac{\rho_{i+1,j}\Delta x_i+\rho_{i,j}\Delta x_{i+1}}{\Delta x_i+\Delta x_{i+1}}\right)+\\&-\frac{1}{\Delta y_j+\Delta y_{j-1}}\left(\frac{\rho_{i+1,j-1}\Delta x_i+\rho_{i,j-1}\Delta x_{i+1}}{\Delta x_i+\Delta x_{i+1}}\right)\end{aligned} \tag{5.111}$$

$$\begin{aligned}\left(\frac{\partial\rho}{\partial x}\right)_{i,j+\frac{1}{2}}&=\frac{1}{\Delta x_i+\Delta x_{i+1}}\left(\frac{\rho_{i+1,j+1}\Delta y_j+\rho_{i+1,j}\Delta y_{j+1}}{\Delta y_j+\Delta y_{j+1}}\right)+\\&+\frac{\Delta x_{i+1}-\Delta x_{i-1}}{(\Delta x_i+\Delta x_{i+1})(\Delta x_i+\Delta x_{i-1})}\left(\frac{\rho_{i,j+1}\Delta y_j+\rho_{i,j}\Delta y_{j+1}}{\Delta y_j+\Delta y_{j+1}}\right)\\&-\frac{1}{\Delta x_i+\Delta x_{i-1}}\left(\frac{\rho_{i-1,j+1}\Delta y_j+\rho_{i-1,j}\Delta y_{j+1}}{\Delta y_j+\Delta y_{j+1}}\right)\end{aligned} \tag{5.112}$$

$$\left(\frac{\partial \rho}{\partial y}\right)_{i,j+\frac{1}{2}} = \frac{\rho_{i,j+1} - \rho_{i,j}}{\Delta y_{j+\frac{1}{2}}} \tag{5.113}$$

5.5.3 Tangential terms

5.3.3.1 Fluid phase

The gradient of the total stress for the fluid in Equation (5.66) is multiplied to $\frac{1}{\rho_{fc}^{n}}$. This term has to be defined in the first equation at the right face of the cell and in the second at the top face (see equations 5.108 and 5.109 respectively).

The gradient of the total stresses in (5.66) can be written as

$$\frac{\partial \tau_{xx}^{f}}{\partial x} + \frac{\partial \tau_{xy}^{f}}{\partial y} \tag{5.114}$$

for the x-momentum equation and

$$\frac{\partial \tau_{yx}^{f}}{\partial x} + \frac{\partial \tau_{yy}^{f}}{\partial y} \tag{5.115}$$

for the y-momentum equation. Once again the stress gradient in the x-direction is calculated at the right face of the computational cell, while in the y-direction it is computed at the top face of the cell. Thus, the first term of 5.114 can be written in the following finite difference from

$$\left(\frac{\partial \tau_{xx}^{f}}{\partial x}\right)_{i+\frac{1}{2},j} = \frac{\left(\tau_{xx}^{f}\right)_{i+1,j} - \left(\tau_{xx}^{f}\right)_{i,j}}{\Delta x_{i+\frac{1}{2}}}. \tag{5.116}$$

The second term in 5.114 can be written as

$$\left(\frac{\partial \tau_{xy}^{f}}{\partial x}\right)_{i+\frac{1}{2},j} = \frac{\left(\tau_{xy}^{f}\right)_{i+\frac{1}{2},j+\frac{1}{2}} - \left(\tau_{xy}^{f}\right)_{i+\frac{1}{2},j+\frac{1}{2}}}{\Delta y_j}. \tag{5.117}$$

The total stresses (normal and shear) above are the summation of molecular stresses and Reynolds stresses. The former are the products of the molecular viscosity and the strain rates of the mean flow, and the latter can be obtained by the nonlinear algebraic Reynolds stress model (5.118). Both of them involve the evaluation of the strain rates of the mean flow. The normal stress in the x-direction is evaluated at the center of the cell which involves the calculation of normal strain rate of the mean flow

$$\left(\frac{\partial u^{f}}{\partial x}\right)_{i,j}^{n} = \frac{\left(u^{f}\right)_{i+\frac{1}{2},j}^{n} - \left(u^{f}\right)_{i-\frac{1}{2},j}^{n}}{\Delta x_i}. \tag{5.118}$$

The shear stress is evaluated at the vertices of the cell which involves the calculations of both $\frac{\partial u^{f}}{\partial y}$ and $\frac{\partial v^{f}}{\partial x}$. The finite difference form of these derivatives can be referred to (5.96) and (5.97). the similar finite-difference formulas can be obtained for stress gradient terms in the y-momentum equation (5.117). The shear strain rate of the mean flow can be again referred to (5.96) and (5.97) and the normal strain rate at the cell (i, j) in the y-direction is expressed as

$$\left(\frac{\partial v^{f}}{\partial y}\right)_{i,j}^{n} = \frac{\left(v^{f}\right)_{i,j+\frac{1}{2}}^{n} - \left(v^{f}\right)_{i,j-\frac{1}{2}}^{n}}{\Delta y_j}. \tag{5.119}$$

5.3.3.2 Sediment phase

Also the gradient of the total stress of the sediment phase is multiplied in Equation (5.67) to $\frac{1}{\rho_{fc}^{n}}$ (see equations 5.108 and 5.109 respectively).

The gradients of the total stresses can be written as

$$\frac{\partial \tau_{xx}^{s}}{\partial x}+\frac{\partial \tau_{xy}^{s}}{\partial y} \tag{5.120}$$

for the x-momentum equation and

$$\frac{\partial \tau_{yy}^{s}}{\partial y}+\frac{\partial \tau_{yx}^{s}}{\partial x} \tag{5.121}$$

for the y-momentum equation. One again the stress gradient in the x-momentum equation is calculated at the right face of the computational cell, while in the y-momentum equation it is computed at the top face of the cell.

In finite difference form for the x-direction we can write:

$$\begin{aligned}\frac{\partial \tau_{xx}^{n}}{\partial x}+\frac{\partial \tau_{xy}^{n}}{\partial y}=\left(\frac{\partial \tau_{xx}^{n}}{\partial x}\right)_{i+\frac{1}{2},j}+\left(\frac{\partial \tau_{xy}^{n}}{\partial y}\right)_{i+\frac{1}{2},j}= \\ =\frac{(\tau_{xx}^{n})_{i+1,j}-(\tau_{xx}^{n})_{i,j}}{\Delta x_{i+\frac{1}{2}}}+\frac{\left(\tau_{xy}^{n}\right)_{i+\frac{1}{2},j+\frac{1}{2}}-\left(\tau_{xy}^{n}\right)_{i+\frac{1}{2},j-\frac{1}{2}}}{\Delta y_{j}}\ .\end{aligned} \tag{5.122}$$

and for the y-direction we have

$$\begin{aligned}\frac{\partial \tau_{yy}^{n}}{\partial y}+\frac{\partial \tau_{yx}^{n}}{\partial x}=\left(\frac{\partial \tau_{yy}^{n}}{\partial y}\right)_{i,j+\frac{1}{2}}+\left(\frac{\partial \tau_{yx}^{n}}{\partial x}\right)_{i,j+\frac{1}{2}}= \\ =\frac{\left(\tau_{yy}^{n}\right)_{i,j+1}-\left(\tau_{yy}^{n}\right)_{i,j}}{\Delta y_{j+\frac{1}{2}}}+\frac{\left(\tau_{yx}^{n}\right)_{i+\frac{1}{2},j+\frac{1}{2}}-\left(\tau_{yx}^{n}\right)_{i-\frac{1}{2},j+\frac{1}{2}}}{\Delta x_{i}}.\end{aligned} \tag{5.123}$$

The total stresses $\left(\tau_{xx}^{s},\tau_{xy}^{s},\tau_{yy}^{s},\tau_{yx}^{s}\right)$ are the summation of the mean particle shear and normal stresses due to small scale interactions $\left(\tau_{xx}^{s0},\tau_{xy}^{s0},\tau_{yx}^{s0},\tau_{yy}^{s0}\right)$ and the large-scale sediment Reynolds stress $\left(R_{xx}^{s},R_{xy}^{s},R_{yx}^{s},R_{yy}^{s}\right)$, see Equations 5.36, 5.37, 5.38, 5.39.

The mean particle shear and normal stresses due to small scale interactions for the x-direction is

$$(\tau_{xx}^{s0})_{i+\frac{1}{2},j} = -\frac{2}{3}(\rho_{sc})_{i+\frac{1}{2},j}\left[1 + 4G_{i+\frac{1}{2},j}\right](K_s)_{i+\frac{1}{2},j} + A_{i+\frac{1}{2},j}E_{i+\frac{1}{2},j}\left(\frac{\partial u^s}{\partial x}\right)_{i+\frac{1}{2},j} \quad (5.124)$$

$$(\tau_{xy}^{s0})_{i+\frac{1}{2},j} = A_{i+\frac{1}{2},j}E_{i+\frac{1}{2},j}\left[\left(\frac{\partial u^s}{\partial y}\right)_{i+\frac{1}{2},j} + \left(\frac{\partial v^s}{\partial x}\right)_{i+\frac{1}{2},j}\right] \quad (5.125)$$

and for the y-direction is:

$$(\tau_{yy}^{s0})_{i,j+\frac{1}{2}} = -\frac{2}{3}(\rho_{sc})_{i,j+\frac{1}{2}}\left[1 + 4G_{i,j+\frac{1}{2}}\right](K_s)_{i,j+\frac{1}{2}} + A_{i,j+\frac{1}{2}}E_{i,j+\frac{1}{2}}\left(\frac{\partial v^s}{\partial y}\right)_{i,j+\frac{1}{2}} \quad (5.126)$$

$$(\tau_{yx}^{s0})_{i,,j+\frac{1}{2}} = A_{i,j+\frac{1}{2}}E_{i,j+\frac{1}{2}}\left[\left(\frac{\partial u^s}{\partial y}\right)_{i,j+\frac{1}{2}} + \left(\frac{\partial v^s}{\partial x}\right)_{i,j+\frac{1}{2}}\right]. \quad (5.127)$$

In which $\left(\frac{\partial u^s}{\partial x}\right)_{i+\frac{1}{2},j}$ is defined as in Equation (5.94), $\left(\frac{\partial u^s}{\partial y}\right)_{i+\frac{1}{2},j}$ as in Equation (5.95), $\left(\frac{\partial v^s}{\partial y}\right)_{i,j+\frac{1}{2}}$ as in Equation (5.98) and $\left(\frac{\partial v^s}{\partial x}\right)_{i,j+\frac{1}{2}}$ as in Equation (5.99). While $\left(\frac{\partial v^s}{\partial x}\right)_{i,j+\frac{1}{2}}$ and $\left(\frac{\partial v^s}{\partial x}\right)_{i+\frac{1}{2},j}$ are defined as:

$$\left(\frac{\partial v^s}{\partial x}\right)_{i,j+\frac{1}{2}} = \\ = \frac{v^s_{i+1,j+\frac{1}{2}}(\Delta x_i + \Delta x_{i-1}) + v^s_{i,j+\frac{1}{2}}(\Delta x_{i+1} - \Delta x_{i-1}) - v^s_{i-1,j+\frac{1}{2}}(\Delta x_i + \Delta x_{i+1})}{(\Delta x_i + \Delta x_{i+1})(\Delta x_i + \Delta x_{i-1})} \quad (5.128)$$

$$\left(\frac{\partial v^s}{\partial x}\right)_{i+\frac{1}{2},j} = \frac{v^s_{i+1,j+\frac{1}{2}} + v^s_{i+1,j-\frac{1}{2}} - v^s_{i,j+\frac{1}{2}} - v^s_{i,j-\frac{1}{2}}}{2\Delta x_{i+\frac{1}{2}}} \quad (5.129)$$

In Equations (5.124) and (5.125), $G_{i+\frac{1}{2},j}, A_{i+\frac{1}{2},j}$ and $E_{i+\frac{1}{2},j}$ depend on $c_{i+\frac{1}{2},j}$:

$$c_{i+\frac{1}{2},j} = \frac{c_{i,j}\Delta x_{i+1} + c_{i+1,j}\Delta x_i}{\Delta x_{i+1} + \Delta x_i} \tag{5.130}$$

and in Equations (5.126) and (5.127), $G_{i,j+\frac{1}{2}}, A_{i,j+\frac{1}{2}}$ and $E_{i,j+\frac{1}{2}}E$ depend on $c_{i,j+\frac{1}{2}}$:

$$c_{i,j+\frac{1}{2}} = \frac{c_{i,j}\Delta y_{j+1} + c_{i,j+1}\Delta y_j}{\Delta y_{j+1} + \Delta y_j} \ . \tag{5.131}$$

The Reynolds stresses for the x-direction are written as

$$(R^s_{xx})_{i+\frac{1}{2}j} = -\frac{2}{3}(\rho_{sc})_{i+\frac{1}{2},j}(K_s)_{i+\frac{1}{2},j} + \frac{4}{3}\rho^s(\nu_{st})_{i+\frac{1}{2},j}\left(\frac{\partial u^s}{\partial x}\right)_{i+\frac{1}{2},j} \tag{5.132}$$

$$\left(R^s_{xy}\right)_{i+\frac{1}{2},j} = \rho^s(\nu_{st})_{i+\frac{1}{2},j}\left[\left(\frac{\partial u^s}{\partial y}\right)_{i+\frac{1}{2},j} + \left(\frac{\partial v^s}{\partial x}\right)_{i+\frac{1}{2},j}\right] \tag{5.133}$$

and for the y-direction as

$$\left(R^s_{yy}\right)_{i,j+\frac{1}{2}} = -\frac{2}{3}(\rho_{sc})_{i,j+\frac{1}{2}}(K_s)_{i,j+\frac{1}{2}} + \frac{4}{3}\rho^s(\nu_{st})_{i,j+\frac{1}{2}}\left(\frac{\partial v^s}{\partial y}\right)_{i,j+\frac{1}{2}} \tag{5.134}$$

$$\left(R^s_{yx}\right)_{i,j+\frac{1}{2}} = \rho^s(\nu_{st})_{i,j+\frac{1}{2}}\left[\left(\frac{\partial u^s}{\partial y}\right)_{i,j+\frac{1}{2}} + \left(\frac{\partial v^s}{\partial x}\right)_{i,j+\frac{1}{2}}\right] \tag{5.135}$$

5.5.4 Drag force terms

As for the others terms, also the drag force terms are defined in the x-direction at the right face of the numerical cell and in the y-direction at the top face.

$$-\beta c\left(u^f - u^s\right) + \beta v_{ft}\frac{\partial c}{\partial x} = \\ = -\beta_{i+\frac{1}{2},j} c_{i+\frac{1}{2},j}\left(u^f_{i+\frac{1}{2},j} - u^s_{i+\frac{1}{2},j}\right) + \beta_{i+\frac{1}{2},j}\left(v_{ft}\right)_{i+\frac{1}{2},j}\left(\frac{\partial c}{\partial x}\right)_{i+\frac{1}{2},j} \tag{5.136}$$

$$-\beta c\left(v^f - v^s\right) + \beta v_{ft}\frac{\partial c}{\partial y} = \\ = -\beta_{i,j+\frac{1}{2}} c_{i,j+\frac{1}{2}}\left(v^f_{i,j+\frac{1}{2}} - v^s_{i,j+\frac{1}{2}}\right) + \beta_{i,j+\frac{1}{2}}\left(v_{ft}\right)_{i,j+\frac{1}{2}}\left(\frac{\partial c}{\partial y}\right)_{i,j+\frac{1}{2}} \tag{5.137}$$

where

$$\beta_{i+\frac{1}{2},j} = \frac{\rho^f \left(U_r\right)_{i+\frac{1}{2},j}}{d}\left(\frac{18}{Re_{p_{i+\frac{1}{2},j}}} + 0.3\right)\frac{1}{\left(1 - c^n_{i+\frac{1}{2},j}\right)^{n_{i+\frac{1}{2},j}}} \tag{5.138}$$

$$\beta_{i,j+\frac{1}{2}} = \frac{\rho^f \left(U_r\right)_{i,j+\frac{1}{2}}}{d}\left(\frac{18}{Re_{p_{i,j+\frac{1}{2}}}} + 0.3\right)\frac{1}{\left(1 - c^n_{i,j+\frac{1}{2}}\right)^{n_{i,j+\frac{1}{2}}}} \tag{5.139}$$

$$\left(\frac{\partial c}{\partial x}\right)_{i+\frac{1}{2},j} = \frac{c_{i+1,j} - c_{i,j}}{\Delta x_{i+\frac{1}{2},j}} \tag{5.140}$$

$$\left(\frac{\partial c^n}{\partial y}\right)_{i,j+\frac{1}{2}} = \frac{c_{i,j+1} - c_{i,j}}{\Delta y_{i,j+\frac{1}{2}}} \tag{5.141}$$

$$\left(v_{ft}\right)_{i+\frac{1}{2},j} = C_\mu \frac{\left(k_f^n\right)^2_{i+\frac{1}{2},j}\left(1 - c^n_{i+\frac{1}{2},j}\right)}{\epsilon^n_{i+\frac{1}{2},j}} \tag{5.142}$$

$$\left(v_{ft}\right)_{i,j+\frac{1}{2}} = C_\mu \frac{\left(k_f^n\right)^2_{i,j+\frac{1}{2}}\left(1 - c^n_{i,j+\frac{1}{2}}\right)}{\epsilon^n_{i,j+\frac{1}{2}}} \tag{5.143}$$

5.5.5 Pressure terms

Pressure is defined at the center of the computational cell, hence the Poisson Equation has to be discretized calculating all terms at the center of the cell.

If we consider the right terms of Equation (5.73), we have:

$$\begin{aligned}
&\frac{\partial}{\partial x}\left[(1-c^n)\left(\frac{\partial P^{n+1}}{\partial x}\right)\right] + \frac{\partial}{\partial y}\left[(1-c^n)\left(\frac{\partial P^{n+1}}{\partial y}\right)\right] = \\
&= \left\{\frac{\partial}{\partial x}\left[(1-c^n)\left(\frac{\partial P^{n+1}}{\partial x}\right)\right]\right\}_{i,j} + \left\{\frac{\partial}{\partial y}\left[(1-c^n)\left(\frac{\partial P^{n+1}}{\partial y}\right)\right]\right\}_{i,j} = \\
&= \frac{1}{\Delta x_i}\left\{\left(1 - c^n_{i+\frac{1}{2},j}\right)\left(\frac{\partial P^{n+1}}{\partial x}\right)_{i+\frac{1}{2},j} - \left(1 - c^n_{i-\frac{1}{2},j}\right)\left(\frac{\partial P^{n+1}}{\partial x}\right)_{i-\frac{1}{2},j}\right\} + \\
&+ \frac{1}{\Delta y_j}\left\{\left(1 - c^n_{i,j+\frac{1}{2}}\right)\left(\frac{\partial P^{n+1}}{\partial y}\right)_{i,j+\frac{1}{2}} - \left(1 - c^n_{i,j-\frac{1}{2}}\right)\left(\frac{\partial P^{n+1}}{\partial y}\right)_{i,j-\frac{1}{2}}\right\}
\end{aligned} \tag{5.144}$$

where

$$\left(\frac{\partial P^{n+1}}{\partial x}\right)_{i+\frac{1}{2},j} = \frac{P^{n+1}_{i+1,j} - P^{n+1}_{i,j}}{\Delta x_{i+\frac{1}{2}}} \tag{5.145}$$

$$\left(\frac{\partial P^{n+1}}{\partial x}\right)_{i-\frac{1}{2},j} = \frac{P_{i,j}^{n+1} - P_{i-1,j}^{n+1}}{\Delta x_{i-\frac{1}{2}}} \tag{5.146}$$

$$\left(\frac{\partial P^{n+1}}{\partial y}\right)_{i,j+\frac{1}{2}} = \frac{P_{i,j+1}^{n+1} - P_{i,j}^{n+1}}{\Delta y_{j+\frac{1}{2}}} \tag{5.147}$$

$$\left(\frac{\partial P^{n+1}}{\partial y}\right)_{i,j-\frac{1}{2}} = \frac{P_{i,j}^{n+1} - P_{i,j-1}^{n+1}}{\Delta y_{j-\frac{1}{2}}} \tag{5.148}$$

$$c_{i-\frac{1}{2},j}^{n} = \frac{c_{i,j}^{n}\Delta x_{i-1} - c_{i-1,j}^{n}\Delta x_i}{\Delta x_i + \Delta x_{i-1}} \tag{5.149}$$

$$c_{i,j-\frac{1}{2}}^{n} = \frac{c_{i,j}^{n}\Delta y_{j-1} - c_{i,j-1}^{n}\Delta y_j}{\Delta y_j + \Delta y_{j-1}} \tag{5.150}$$

The left terms of the Equation (5.73) can be discretized as:

$$\begin{aligned}
&\frac{\rho_{fc}^{n} - \rho_{fc}^{n-1}}{\Delta t^2} + \frac{\rho_{fc}^{n}}{\Delta t}\left[\frac{\partial\left(\tilde{u}^f\right)^{n+1}}{\partial x} + \frac{\partial\left(\tilde{v}^f\right)^{n+1}}{\partial y}\right] + \\
&+ \frac{\left(\tilde{u}^f\right)^{n+1}}{\Delta t}\frac{\partial \rho_{fc}^{n}}{\partial x} + \frac{\left(\tilde{v}^f\right)^{n+1}}{\Delta t}\frac{\partial \rho_{fc}^{n}}{\partial y} = \frac{\left(\rho_{fc}^{n}\right)_{i,j} - \left(\rho_{fc}^{n-1}\right)_{i,j}}{\Delta t^2} + \\
&+ \frac{\left(\rho_{fc}^{n}\right)_{i,j}}{\Delta t}\left[\left(\frac{\partial\left(\tilde{u}^f\right)^{n+1}}{\partial x}\right)_{i,j} + \left(\frac{\partial\left(\tilde{v}^f\right)^{n+1}}{\partial y}\right)_{i,j}\right] + \\
&+ \frac{\left(\tilde{u}^f\right)_{i,j}^{n+1}}{\Delta t}\left(\frac{\partial \rho_{fc}^{n}}{\partial x}\right)_{i,j} + \frac{\left(\tilde{v}^f\right)_{i,j}^{n+1}}{\Delta t}\left(\frac{\partial \rho_{fc}^{n}}{\partial y}\right)_{i,j}
\end{aligned} \tag{5.151}$$

where $\left(\frac{\partial\left(\tilde{u}^f\right)^{n+1}}{\partial x}\right)_{i,j}$, $\left(\frac{\partial\left(\tilde{v}^f\right)^{n+1}}{\partial y}\right)_{i,j}$, $\left(\tilde{u}^f\right)_{i,j}^{n+1}$ and $\left(\tilde{v}^f\right)_{i,j}^{n+1}$ are defined in Equations (5.118), (5.119), (5.80) and (5.81), respectively. Whereas the derivatives of the density at the centre of the computational cells are defined as following:

$$\left(\frac{\partial \rho_{fc}^{n}}{\partial x}\right)_{i,j} = \\ = \frac{\left(\rho_{fc}^{n}\right)_{i+1,j}(\Delta x_{i-1} + \Delta x_i) + \left(\rho_{fc}^{n}\right)_{i,j}(\Delta x_{i+1} + \Delta x_{i-1}) - \left(\rho_{fc}^{n}\right)_{i-1,j}(\Delta x_{i+1} + \Delta x_i)}{(\Delta x_i + \Delta x_{i+1})(\Delta x_i + \Delta x_{i-1})} \quad (5.152)$$

$$\left(\frac{\partial \rho_{fc}^{n}}{\partial y}\right)_{i,j} = \\ = \frac{\left(\rho_{fc}^{n}\right)_{i,j+1}\left(\Delta y_{j-1} + \Delta y_j\right) + \left(\rho_{fc}^{n}\right)_{i,j}\left(\Delta y_{j+1} + \Delta y_{j-1}\right) - \left(\rho_{fc}^{n}\right)_{i,j-1}\left(\Delta y_{j+1} + \Delta y_j\right)}{\left(\Delta y_j + \Delta y_{j+1}\right)\left(\Delta y_j + \Delta y_{j-1}\right)} \quad (5.153)$$

By this way, a set of linear algebraic equations for the pressure field that can be solved by standard matrix solvers. Here the conjugate gradient method with the preconditioner of incomplete Cholesky decomposition is used to solve the resulting sparse and symmetric system of equations.

Solving the PPE equation the values of the pressure at the n+1 time step are determined and the values of the sediment and fluid velocities and the concentration can be update.

CHAPTER 6

WAVE-INDUCED EROSION AND DEPOSITION PATTERNS: VERIFICATION OF MODEL RESULTS.

In this chapter a preliminary verification of the two-phase numerical model is presented. Some simple cases were chosen in order to check all the new subroutines and equations implemented in the IH-2VOF model. In Table 6.1 the principal characteristic of the cases tested are summarized. The behavior of the sediment bottom in terms of concentration and elevation was investigated.

Table 6.1. Characteristics of cases tested.

Test	Wave attack		Water depth	Boundary Condition		Mesh resolution	
	H_s [m]	T_p [s]	wd [m]	Seaward	Landward	cell width [m]	cell height [m]
P1	0.1	4.3	2.5	H_s , T_p regular waves	open	0.05	0.05
P2	0.1	4.3	2.5	H_s , T_p regular waves	close	0.05	0.05

6.1 Computational set-up

Both tests - P1 and P2 - were performed in a numerical flume 10 m long and 4 m deep under regular waves with significant wave height $H_S = 0.1\,m$ and peak period $T_p = 4.3\,s$. An homogeneous layer of sand ($h_s = 1\,m$) on the bottom of the channel was present. The solid phase was characterized by a density $\rho^s = 2.6\,kg/m^3$ and a diameter $d = 3\,mm$. The water depth h_w was set equals to 2.5 m (Figure 6.1).

In the test P1 an open boundary condition was set on the landward (right) boundary, whereas, in the test P2, the right boundary condition has been changed and a close boundary was set.

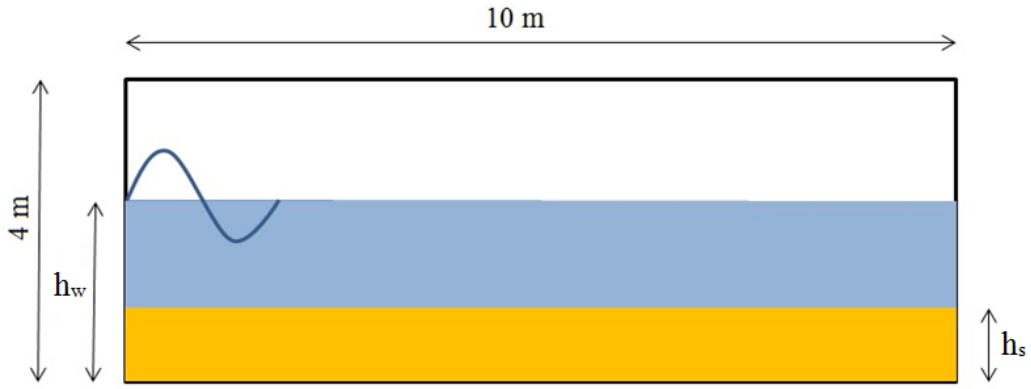

Figure 6.1. Sketch of the cases tested.

In both tests the same regular wave attack is imposed and in Figure 6.2 the water level at the wave gouge sets 2 m from the beginning of the channel is reported.

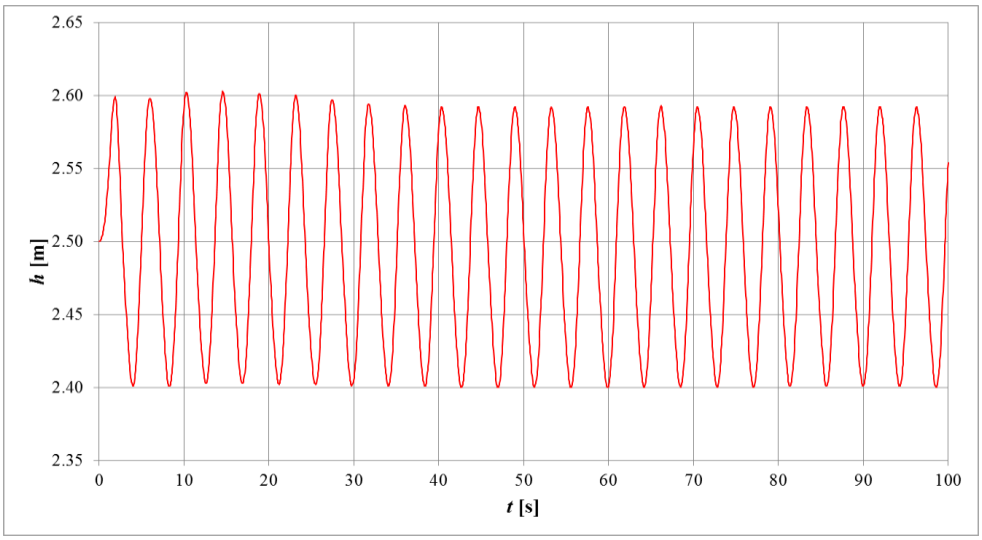

Figure 6.2. Water depth trend measured at $x = 2\ m$ from the beginning of the channel.

6.2 Results for test P1

Figure 6.3 reports the water level along the channel at three different time steps: 20 s (red color), 50 s (green color) and 80 s (blue color). Because the wave length is about equals to 20 m and the channel length 10 m, we can observe one wave along the channel for each time step.

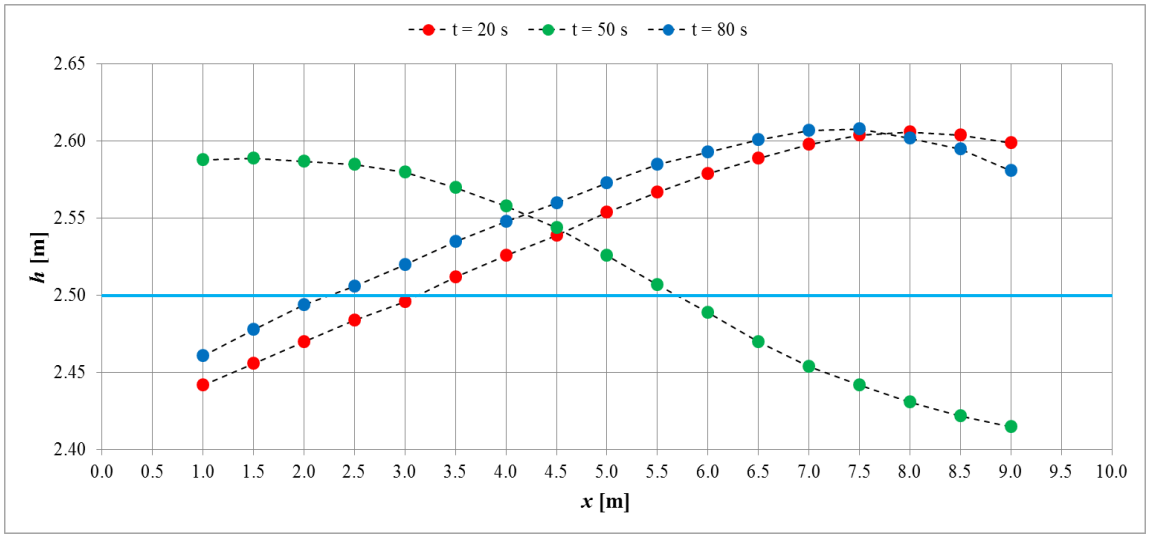

Figure 6.3. Water depth trend along the channel at t = 20 s (red), t = 50 s (green) and t = 80 s (blue).

The evolution of the sand bottom at the same time steps (20 s, red color; 50 *s*, green color; 80 *s*, blue color) is reported in Figure 6.4. It is possible to observe that the trend is the following: erosion in the first half of the channel and deposition in the second half. Besides, the bottom level along the numerical channel tends to decrease over the time because the landward boundary condition (right) is open and the sand can get out from the numerical domain.

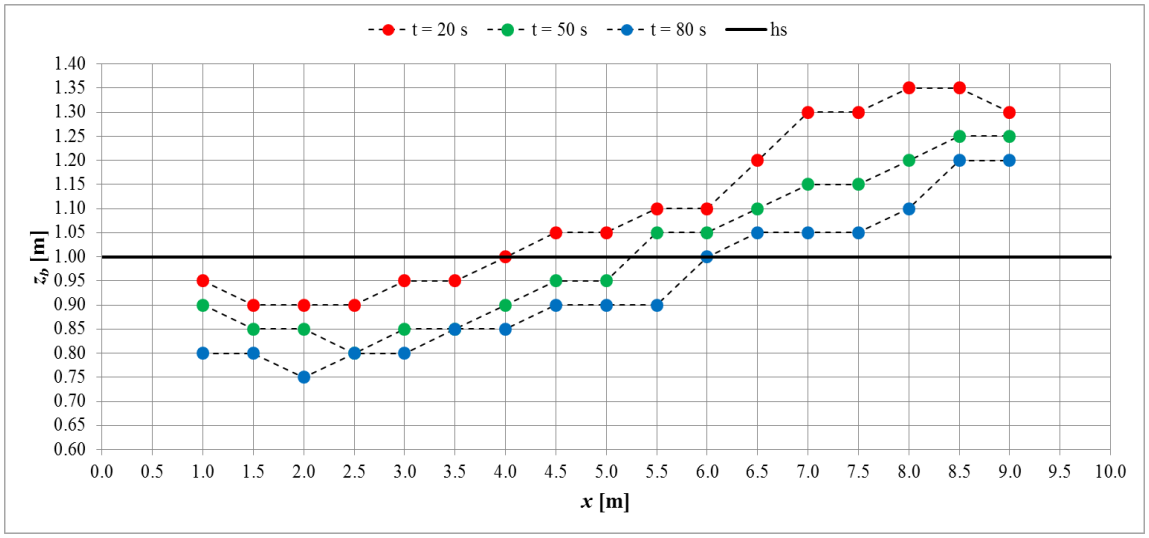

Figure 6.4. Bottom level along the channel at t = 20 s (red), t = 50 s (green) and t = 80 s (blue). hs is the original sediment bottom.

Figures 6.5 and 6.6 report the velocity profiles at different time steps and at different distances from the beginning of the channel. In particular, in Figure 6.5 the horizontal velocities at the gauge sets at $x = 1\,m$ from the beginning of the channel are shown whereas Figure 6.6 presents the velocity profiles at the gauge sets at $x = 8\,m$. By comparing these figures with Figure 6.3, it can be observed, as expected, that in correspondence with the wave crest the velocity values are positive whereas in correspondence with the wave trough the velocity values are negative.

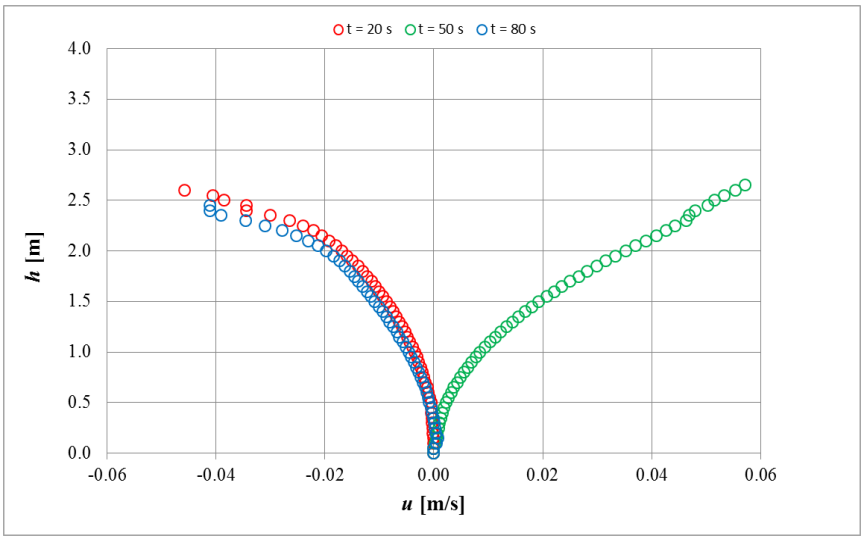

Figure 6.5. Horizontal velocity at the gauge sets at $x = 1\,m$ from the begin of the channel.

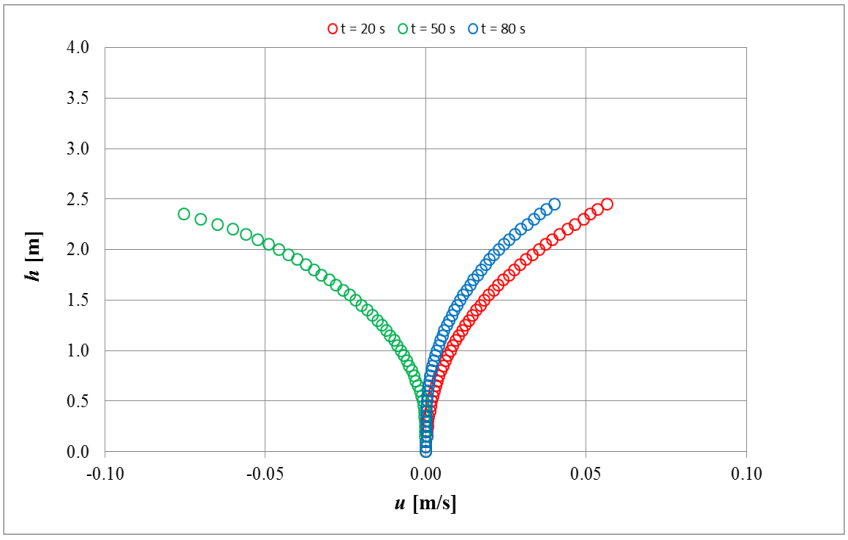

Figure 6.6. Horizontal velocity at the gauge sets at $x = 8\,m$ from the begin of the channel.

Figures 6.7 and 6.8 present calculated values of the concentration. In the lowest portion of the sheet there is a high concentration (almost equal to close-packed concentration, $c^* = 0.635$) and then the concentration slowly decreases in the vertical direction. In the same region, the fluid velocity is relatively weak (see Figures 6.5 and 6.6). Such features are due to the contact stress and the high viscosity implemented in the model for the region of enduring contacts. Over time the values of the concentration decrease because the right boundary condition is open.

The position of the bottom (that you can see in Figure 6.4) is determined by considering that if, in a given cell, the concentration has a value greater than 50% of the close-packed concentration, then that cell is part of the bottom. However, there is some material in suspension that is not included in the seabed.

In particular, Figure 6.7 presents the sediment concentration at the gauge sets at $x = 1\ m$ from the beginning of the channel. By observing Figure 6.4, it appears clearly that in this section the sediment bottom is eroded, hence in Figure 6.7 the diamonds show the concentration of cells that are included into the seabed, whereas the crosses the concentration of cells that have less material and then are not included into the seabed. These are cells with materials in suspension.

As said before, in the second half of the numerical domain an deposition phenomenon is present. As for the previous figure, the diamonds represent the concentration of the cells that are included into the seabed and the crosses the concentration of the cells that are not included.

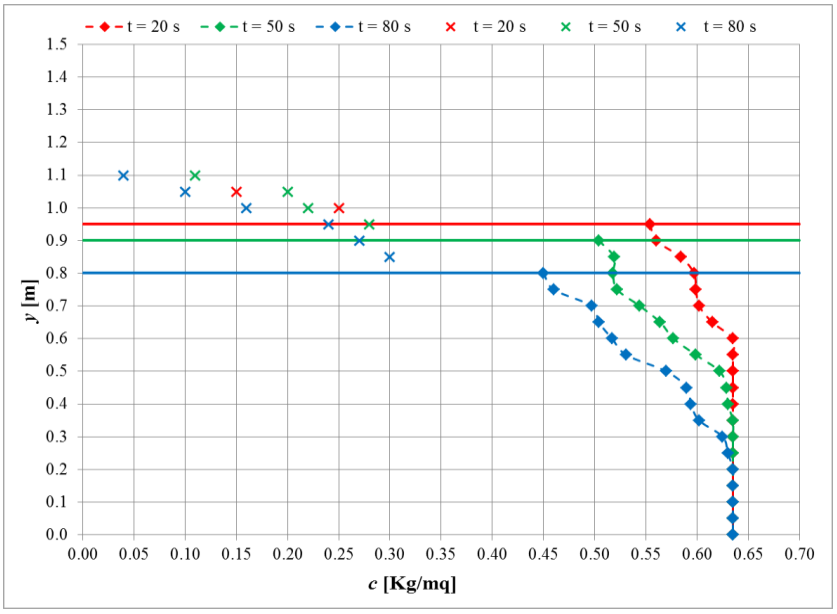

Figure 6.7. Sediment concentration at the gauge sets at $x = 1\ m$ from the begin of the channel.

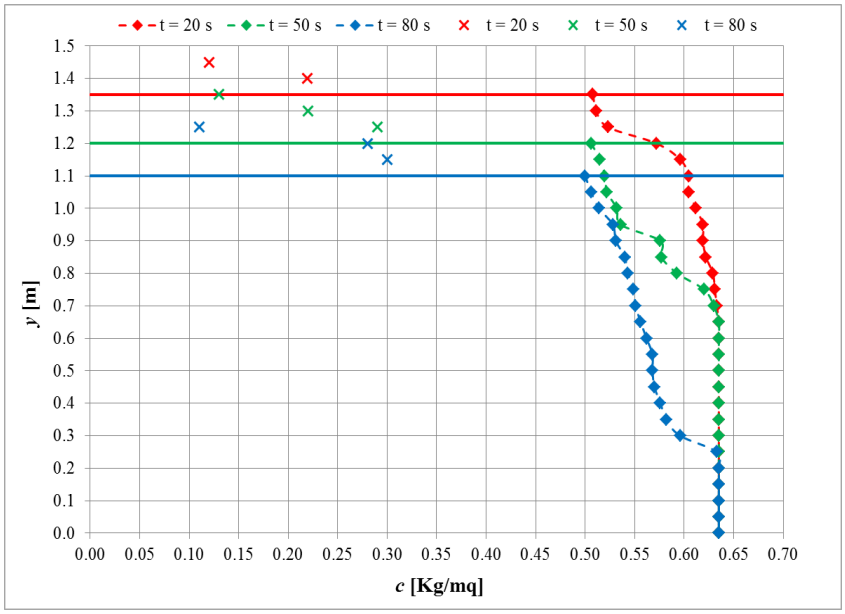

Figure 6.8. Sediment concentration at the gauge sets at $x = 8\ m$ from the begin of the channel.

6.3 Results for test P2

The only difference between tests P1 and P2 is that in P1 the landward (right) boundary was set as an open boundary, whereas, in test P2, the right boundary was set as a close boundary. The goal in this paragraph is to verify if the numerical model is affected by changing the boundary condition.

As for test P1, Figure 6.9 reports the water level along the channel at three different time steps: 20 s (red color), 50 s (green color) and 80 s (blue color). Also in this case, the channel length (10 m) is half the wave length (about 20 m), therefore only one wave along the channel for each time step is observed.

The following figure (Figure 6.10) shows the evolution of the sand bottom at the time steps: 20 s (red color), 50 s (green color) and 80 s (blue color). By comparing this figure with Figure 6.4, it is clear that the numerical model is affected by the change of the right boundary condition. In fact, the erosion-accumulation pattern change completely. In particular, the principal area of erosion is set at the middle of the channel in correspondence with the antinode point. In the second half of the numerical domain is present a strong deposition of the sediment because sand cannot get out from the channel (landward boundary close). Also close to the beginning of the channel, there is a deposition section. Moreover, over the time, the erosion and the accumulation increase because the landward boundary is close and the sediment remains inside the channel.

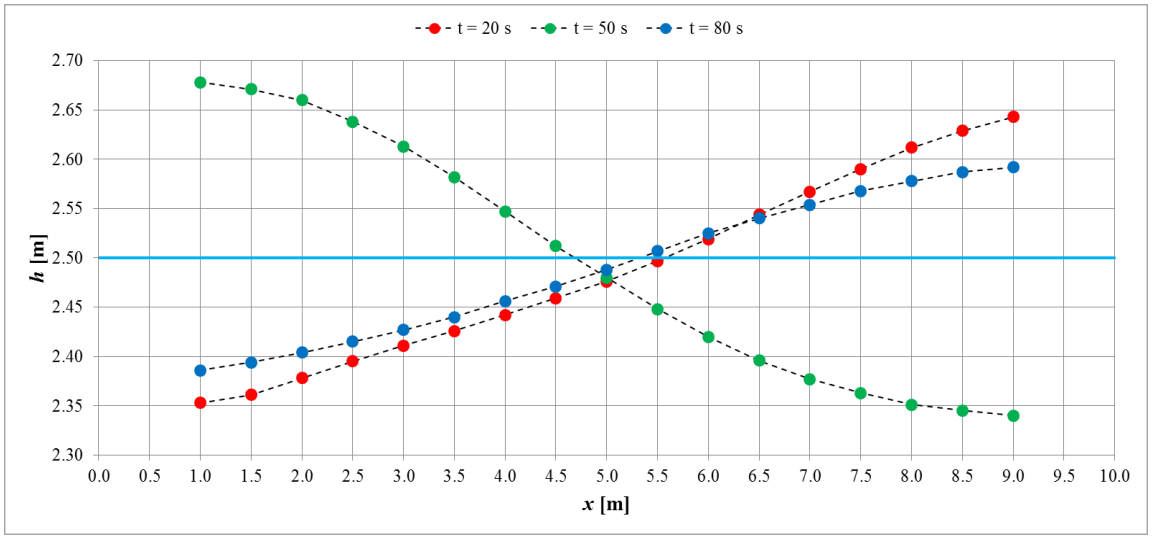

Figure 6.9. Water depth trend along the channel at t = 20 s (red), t = 50 s (green) and t = 80 s (blue).

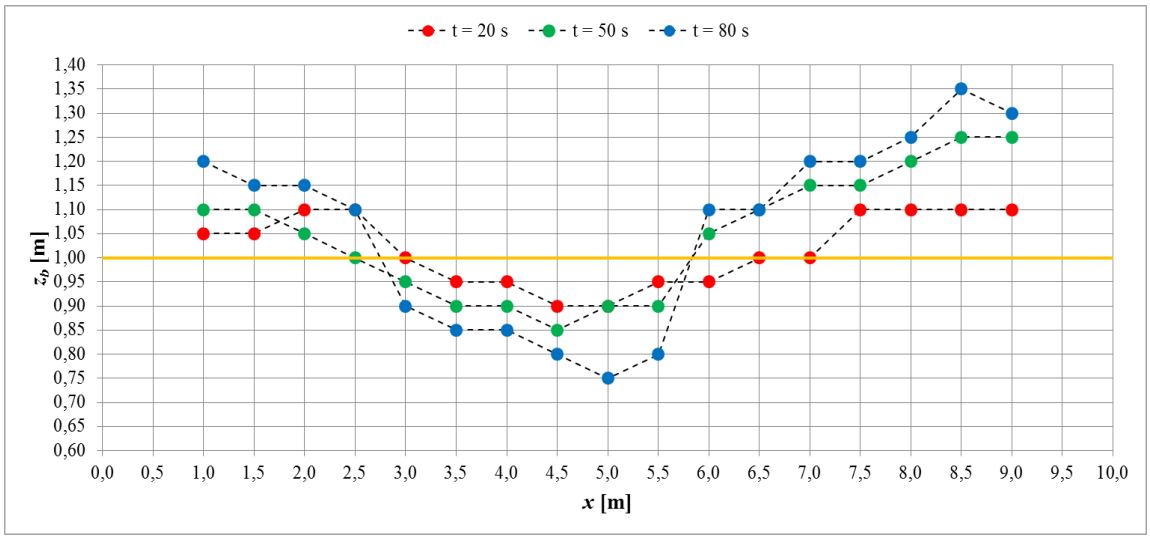

Figure 6.10. Bottom level along the channel at t = 20 s (red), t = 50 s (green) and t = 80 s (blue).

Figure 6.11, 6.12 and 6.13 present the sediment concentration at the gauges set at $x = 2\ m$, $x = 4.5\ m$ and $x = 8\ m$ from the beginning of the channel respectively. As said before, in the first and second half of the numerical domain an accumulation phenomenon is present. Hence, Figure 6.11 and 6.13 show that the maximum bottom level exceed the original value $h_s = 1\ m$.

In the section $x = 4.5\,m$ the sediment bottom is eroded (see Figure 6.10), hence Figure 6.12 shows that the maximum bottom level remains always under $1\,m$, and in particular the erosion increase over the time.

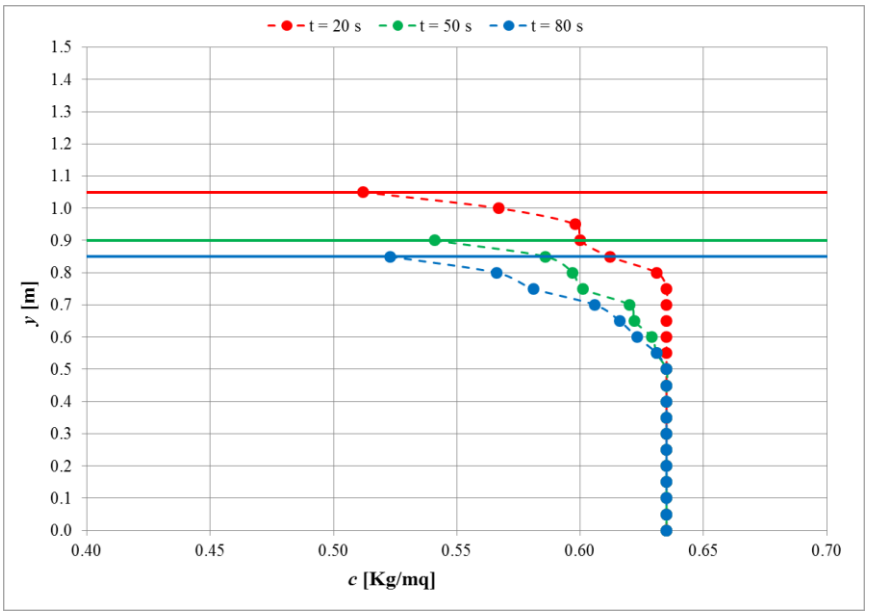

Figure 6.11. Sediment concentration at the gauge sets at $x = 2\,m$ from the begin of the channel.

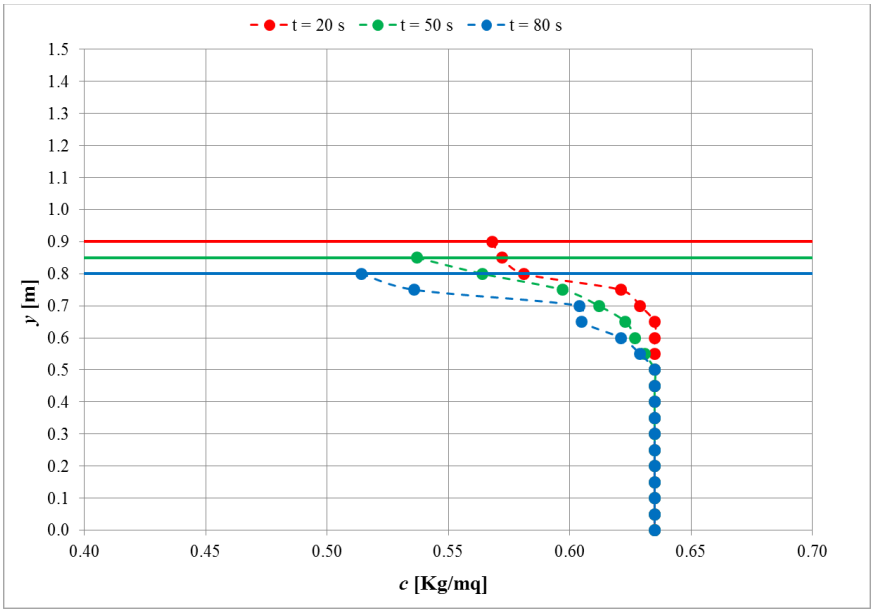

Figure 6.12. Sediment concentration at the gauge sets at $x = 4.5\,m$ from the begin of the channel.

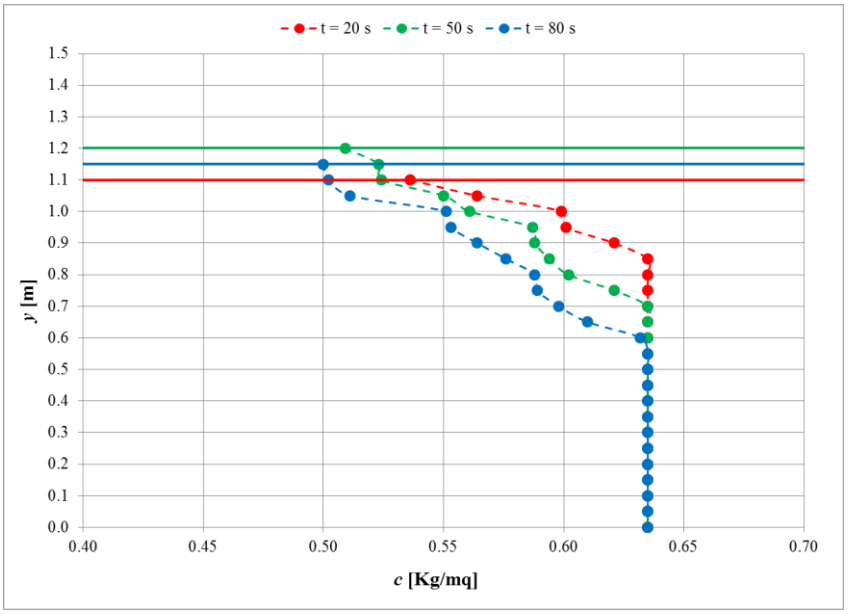

Figure 6.13. Sediment concentration at the gauge sets at $x = 8\ m$ from the begin of the channel.

CHAPTER 7

CONCLUSIONS AND FUTURE WORK.

The main objective of this thesis work was to develop a tool that can represent wave run-up and overtopping together with beach reshaping during storms. A two-dimensional numerical model based on the Reynolds Averaged Navier–Stokes equations (RANS), called IH-2VOF, was selected. This numerical model was used to study the wave-structure interaction and then the new equations for the representation of the sediment transport were introduced.

More than 90 numerical simulations with IH-2VOF model were carried out in order to analyze the flow characteristics (velocities and layer thicknesses) on a dike crest. The numerical data, derived by this analysis, allowed to perform a systematic investigation, which may be useful to extend the existing theoretical approach and provide criteria for design application.

First, in order to verify the numerical simulations, selected numerical results were compared against experimental data and consolidated theoretical formulae. In particular, the wave reflection coefficients calculated numerically for each test was compared with the experimental results obtained by Zanuttigh et al. (2006). The numerical values of K_r appear to be slightly greater than the experimental values. However, the numerical trends show two key issues in agreement with the physical process: the greater the submergence and/or the lower the wave height, the lower the reflection.

As regards the discharge, the numerical values were compared with the theoretical formulae proposed by Eurotop 2007. Both for emerged and zero freeboard cases, the theoretical discharge was well represented by the numerical one. Instead, for submerged cases, the theoretical overflow discharge is well represented by the numerical one, whereas the theoretical overtopping discharge is overestimated. However, this contribute is very small and so it does not affect too much the total results.

The effects of the structure design parameters (i.e. slopes and submergence) on the trend of both depths and velocities over the crest were in-depth investigated. First it was found that the seaward/landward slope does not significantly affect the evolution of the flow depth and velocity over the dike crest whereas the most important parameter is the relative submergence. Wave heights decrease and flow velocities increase while waves travel over the crest. In particular, by increasing the submergence, the wave height decay is less marked and it completely disappears when $R_c/H_s = 1.5$, whereas the increase of the velocity start from about the middle of the crest of the structure and however are very modest. Besides, an appropriate curve able to fit the variation of the wave height/velocity over the dike crest were found. Both for the wave height and for the wave velocity different fitting coefficients were determined on the basis of the submergence and of the significant wave height. The results show that by keeping in constant the submergence, the wave height decay tends to decrease, almost halved, when the significant wave height increases. Similarly, the numerical results show that the wave height decay increases with increasing the submergence when the significant wave height is constant.

These conclusions can be very important in terms of design criteria. In particular, by considering that climate change might cause sea level rise and the increase of the intensity of storms, an increasing of the risk of flooding of low lying areas, an accelerate erosion of exposed soft beach and a damage to existing coastal protection structures may occur. The results obtained in this thesis work (in particular reported in Chapter 4) could be taken into consideration for the upgrade of the structures.

In this context it is also important to predict the dimensionless decay coefficient c_h in order to understand the rate of decay of the wave height on the dike crest. Hence the eventual dependence of the decay coefficient on the characteristics of the structure and/or wave attack was investigated. In particular, an equation describing the trend of the dimensionless coefficient c_h for the wave height was derived. By this way it is possible to predict the decay coefficient that controls the decrease of the wave height over the dike crest.

The second part of this thesis work was focused on further developing the numerical model for sediment transport, aiming at representing beach erosion while waves run-up and overtop the sea banks during storms. Balance equations for the average mass, momentum and energy for the two phases are phrased in terms of concentration-weighted (Favre averaged) velocities. Closures for the correlations between fluctuations in concentration and particle velocities are based on those for collisional grain flow.

The new model allows us to calculate sediment fluxes everywhere in the water column together with the sediment concentration. Moreover it is possible to model the bed profile evolution.

Two different tests were performed under low-intensity regular waves with an homogeneous layer of sand on the bottom of a channel whose length is about half the tested wave length. The only difference between the two tests is that in the first one the landward (right) boundary was set as an open boundary, whereas, in the second one, the right boundary was set as a closed boundary. The change of boundary conditions affects the numerical model response as it can be observed from the erosion-deposition pattern. When the landward boundary is an open boundary, erosion occurs in the first half of the channel (within L/4 from the wave-maker) and the deposition in the second half (between L/4 and L/2). When the landward boundary is set as a closed boundary instead, the erosion area occurs in the middle of the channel, i.e. in correspondence with the antinode point (L/4). In the second half of the numerical domain a strong deposition of the sediment occurs because of the closing wall. Another important difference is that in the first case, the sediment mass tends to decrease over the time because the landward boundary is open and the sand can get out from the numerical domain, whereas in the second case the sediment mass is trapped inside the channel and therefore erosion and accumulation patterns appear to be more marked in time.

Further work should be done to

- validate the sediment transport model on a quantitative basis, considering experimental and theoretical results available in the literature;

- examine the robustness of the model to reproduce different wave attacks and sediment configurations, including the representation of more complex sediment geometries inside the numerical code developed so far;
- analyse beach reshaping during storms and compare to real prototype data for assessing beach retreat and increase hydraulic vulnerability.

REFERENCES

Alsina, J.M., Baldock, T.E., Hughes, M.G., Weir, F., Sierra, J.P., 2005. *Sediment transport numerical modelling in the swash zone.* In: Proceedings of Coastal Dynamics '05, Barcelona, ASCE.

Antuono, M., Brocchini, M., Grosso, G., 2007. *Integral properties of the swash zone and averaging. Part 3. Longshore shoreline boundary conditions for wave-averaged nearshore circulation models.* Journal of Fluid Mechanics 573, 399–415.

Archetti, R., Brocchini, M., 2002. *An integral swash zone model with friction: an experimental and numerical investigation.* Coastal Engineering 45, 89–110.

Asano, T., 1990. *Two-phase flow model on oscillatory sheet-flow.* In: Proceedings of the 22nd ICCE, Delft, Netherlands, pp. 2372–2384.

Asano, T., 1994. *Swash motion due to obliquely incident waves.* In: Proceedings of the 24th Coastal Engineering conference, ASCE, October 23–38, Kobe, Japan, pp. 27–41.

Baba, Y., Camenen, B., 2008. *Importance of the swash longshore sediment transport in morphodynamic models.* Coastal Sediments '07, ASCE, pp. 1938–1946.

Bagnold, R.A., 1963. *Mechanics of marine sedimentation.* In: Hill, M.N. (Ed.), The Sea. Wiley-Interscience, New York, pp. 507–528.

Bagnold, R.A., 1966. *An Approach to the Sediment Transport Problem from General Physics.* US Geological Survey, Washington, DC, 37pp.

Bailard, J.A., 1981. *An energetics total load sediment transport model for a plane sloping beach.* Journal of Geophysical Research 86 (C11), 938–954.

Bakhtyar, R., Yeganeh-Bakhtiary, A., Ghaheri, A., 2007. *Numerical simulation of wave breaking and wave run-up in nearshore.* International Conference on Violent Flow, 20–22 November 2007, Fukuoka, Japan.

Bakhtyar, R., Ghaheri, A., Yeganeh-Bakhtiary, A., Baldock, T.E., 2008. *Longshore sediment transport estimation using fuzzy inference system.* Applied Ocean Research (in press).

Bakhtyar, R., Barry, D.A., Yeganeh-Bakhtiary, A., Ghaheri, A., 2009. *Numerical simulation of surf-swash zone motions and turbulent flow.* Advances in Water Resources 32, 250–263.

Baldock, T.E., Holmes, P., 1997. *Swash hydrodynamics on a steep beach.* Coastal Dynamics Conference, ASCE, Plymouth, UK, pp. 784–793.

Baldock, T.E., Huntley, D.A., 2002. *Long wave forcing by the breaking of random gravity waves on a beach.* Proceedings of Royal Society of London A 458, 2177–2201.

Baldock, T.E., Hughes, M.G., Day, K., Louys, J., 2005. *Swash overtopping and sediment overwash on a truncated beach.* Coastal Engineering 52, 633–645.

Battjes, J. A., 1974. *Computation of set-up, longshore currents, run-up and overtopping due to wind –generated waves.* Report 74-2. Committee on Hydraulics. Dept. Of Civil Engineering, Delf University of Technology.

Bayram, A., Larson, M., Miller, H.C., Kraus, N.C., 2001. *Cross-shore distribution of longshore sediment transport: comparison between predictive formulas and field measurements.* Coastal Engineering 44, 79–99.

Bijker, E.W., 1971. *Longshore transport computations.* Journal of the Waterways, Harbors and Coastal Engineering Division, ASCE 97 (4), 687–703.

Bocquet, L., Losert, W., Schalk, D., Lubensky, T. C. & Gollub, J. P., 2001 *Granular shear flow dynamics and forces: experiment and continuum theory*. Phys. Rev. E65, 011307.

Bosman, G., van der Meer, J. W., Hoffmans, G., Schuttrumpf, H., and Verhagen, H., 2008. *Individual overtopping events at dikes.* Proc., 31st Int. Conf. Coastal Engineering, Vol. 4, ASCE, Reston, Va., 2944–2956.

Bradford, S.F., 2000. *Numerical simulation of surf zone dynamics.* Journal of Waterway, Port, Coastal, and Ocean Engineering, ASCE 126 (1), 1–13.

Brocchini, M., Peregrine, D.H., 1995. *Flow properties of the swash zone.* Proceedings of Coastal Dynamics'95, ASCE, 221-232.

Brocchini, M., Peregrine, D.H., 1996. *Integral flow properties of the swash zone and averaging.* Journal of Fluid Mechanics 317, 241–273.

Calantoni, J., Puleo, J.A., Holland, K.T., 2006. *Simulation of sediment motions using a discrete particle model in the inner surf and swash-zones.* Continental Shelf Research 26, 610–621.

Carrier, G.F., Greenspan, H.P., 1958. *Water waves of finite amplitude on a sloping beach.* Journal of Fluid Mechanics 4 (1), 97–109.

Champagne, F.H., Harris, V.G., Coorsin, S., 1970. *Experiments on nearly homogeneous turbulent shear flow.* Journal of Fluid Mechanics, 41: 81-139.

Chapman, S. & Cowling, T. G., 1970 *The mathematical theory of non-uniform gases.* 3rd edn. Cambridge University Press.

Chopakatla1, S.C., Lippmann, T.C., Richardson, J.H., 2008. *Field verification of a computational fluid dynamics model for wave transformation and breaking in the surf zone.* Journal of Water way, Port, Coastal, and Ocean Engineering, ASCE 134 (2), 71–80.

Christensen, E.D., Deigaard, R., 2001. *Large eddy simulation of breaking waves.* Coastal Engineering 42, 53–86.

Christensen, E.D., 2006. *Large eddy simulation of spilling and plunging breakers.* Coastal Engineering 53, 463–485.

CLASH, 2004. *Crest Level Assessment of coastal Structures by full scale monitoring, neural network prediction and Hazard analysis on permissible wave overtopping.* EC-contract EVK3-CT-2001-00058. www.clash-eu.org.

Crowe, C.T. (Ed.), 2006. *Multiphase Flow Handbook.* Taylor and Francis, Boca Raton.

Cundall, P.A., Strack, O.D., 1979. *A discrete numerical model for granular assembles. Geotechnique* 29 (1), 47–65.

Dalrymple, R.A., Gómez-Gesteira M., Rogers B.D., Panizzo A., Zou S., Crespo A.J.C., Cuomo G., M. Narayanaswamy, 2009. *Smoothed Particle Hydrodynamics for Water Waves*, in Advances in Numerical Simulation of Nonlinear Waves Shi F., Q.Ma, ed., World Scientific Press, ISBN 981-283-649-7.

Davies, A.G., Ribberink, J.S., Temperville, A., Zyserman, J.A., 1997. *Comparisons between sediment transport models and observations made in wave and current flows above plane beds.* Coastal Engineering 31 (1–4), 163–198.

Dodd, N., 1998. *A numerical model of wave run-up, overtopping and regeneration.* Journal of Waterway, Port, Coastal, and Ocean Engineering, ASCE 124 (2), 73–81.

Dong, P., Zhang, K., 1999. *Two-phase flow modeling of sediment motions in oscillatory sheet flow.* Coastal Engineering 36, 87–109.

Drake, T.G., Calantoni, J., 2001. *Discrete particle model for sheet flow sediment transport in the nearshore.* Journal of Geophysical Research 106 (C9), 19859–19868.

Drago, M., Iovenitti, L., 1995. The modelling of plunging breakers by the introduction of a K-l turbulence *closure model.* In: Proceedings of Coastal Dynamics, ASCE, pp. 317–328.

Drew, D. A., 1976 *Production and dissipation of energy in the turbulent flow of a particle–fluid mixture, with some results on drag reduction.* J. Appl. Mech. 43, 543–547.

Elfrink, B., Baldock, T.E., 2002. *Hydrodynamics and sediment transport in the swash zone: a review and perspectives.* Coastal Engineering 45, 149–167.

Elghobashi, S. E. & Abou-Arab, T. W., 1983. *A two-equation turbulence model for two-phase flows.* Phys. Fluids 26, 931–938.

EUROSION, European Union Project ENV.B.3-SER-2001-0030, Reports Online, *Living with coastal erosion in Europe: sediment and space for sustainability*, Part 1 – Major Findings and Policy Recommendations of the Eurosion project, www.eurosion.org.

EurOtop, 2007. *European Manual for the Assessment of Wave Overtopping.* T. Pullen, N.W.H. Allsop, T. Bruce, A. Kortenhaus, H. Schüttrumpf and J.W. van der Meer. At: www.overtopping-manual.com.

Favre, A., 1965. *Equations des gaz turbulent compressible.* J. Méc. 4, 361–390.

Frijlink,H.C., 1952. *Discussion des formules de debit solide de Kalinske, Einstein et Meyer-Peter et Mueller compte tenue des mesures recentes de transport dans les rivieres Neerlandaises.* 2me Journal Hydraulique Societe Hydraulique de France, Grenoble (in French), pp.98–103.

Fuhrman,D.R., Madsen, P.A.,2008. *Simulation of non-linear wave run-up with a high-order Boussinesq model.* Coastal Engineering 55, 139–154.

Garcia, N., Lara, J.L., Losada, I.J., 2004a. *2-D numerical analysis of near-field flow at low-crested breakwaters.* Coastal Engineering 51 (10), 991–1020.

Garcia, N., Lara, J.L., Lomonaco, P., Losada, I.J., 2004b. Flow at low-crested breakwaters under breaking conditions. Proceedings of the 29th International Conference on Coastal Engineering. Word Scientific, pp. 4240-4252.

Gotoh,H., Sakai,T., 1997. *Numerical simulation of sheet flow as granular materials.* Journal of Waterway, Port, Coastal, and Ocean Engineering 123(6),329–336.

Guanche, R., I.J. Losada and J.L. Lara., 2009. *Numerical analysis of wave loads for coastal structure stability*, Coastal Engineering, ELSEVIER, vol. 56, 543-558

Guard, P.A., Baldock,T.E., 2007. *The influence of seaward boundary conditions on swash zone hydrodynamics.* Coastal Engineering 54, 321–331.

Higuera, P., Lara, J.L., Losada, I.J., 2013. *Realistic wave generation and active wave absorption for Navier–Stokes models. Application to OpenFOAM*. Coastal Engineering.

Higuera, P., Lara, J.L., Losada, I.J., 2013. *Simulating Coastal Engineering Processes with OpenFOAM.* Coastal Engineering.

Hirt, C.W., Nichols, B.D., 1981. *Volume of fluid (VOF) method for the dynamics of free boundaries.* Journal of Computational Physics 39, 201–225.

Hoffmann, M. et al., 2008. *Conservation planning and the IUCN Red List*. Endangered Species Research 6, 113–125.

Hsu, T.-J., 2002. *A two-phase flow approach for sediment transport.* PhD thesis, University, Ithaca, NY, USA.

Hsu, T.-J., Sakakiyama, T., Liu, P.L.-F., 2002. *A numerical model for wave motions and turbulence flows in front of a composite breakwater.* Coastal Engineering, 46: 25-50.

Hsu, T.-J., Jenkins, J.T., Liu, P.L.-F., 2003. *On two-phase sediment transport: dilute flow.* Journal of Geophysical Research 108, 3057.

Hsu, T., Jenkins, J.T., Liu, P.L.-F., 2004. *On two-phase sediment transport sheet flow of massive particles.* Proceedings of the Royal Society of London, Seriees A 460, 2223–2250.

Hsu, T.-J., and B. Raubenheimer, 2006. .A numerical and field study on inner-surf and swash sediment transport, Cont. Shelf. Res., 26, 589-598.

Hu, K., Mingham, C.G., Causon, D.M., 2000. *Numerical simulations of wave overtopping of coastal structures using the non-linear shallow water wave equations.* Coastal Engineering 41, 346–365.

Hughes, M.G., Masselink, G., Brander, R.W., 1997. *Flow velocity and sediment transport in the swash zone of a steep beach.* Marine Geology 138, 91–103.

Hughes, M.G., Baldock, T.E., 2004. *Eulerian flow velocities in the swash zone: field data and model predictions.* Journal of Geophysical Research 109, C08009.

Hughes, S.A., N.C. Nadal, 2009. *Laboratory study of combined wave overtopping and storm surge overflow of a levee*. Coastal Engineering, 56, 244-259.

Hughes, S, C. Thornton, J.W. van der Meer and B. Scholl, 2012. *Improvements in describing wave overtopping processes.* ASCE, Proc. ICCE 2012, Santander, Spain.

Hunt, A., 1959. *Design of seawalls and breakwaters*. Journal of the Waterways and Harbors Division. ASCE, pp. 123– 152.

Jenkins, J. T. & Savage, S. B., 1983. *A theory for the rapid flow of identical, smooth, nearly elastic particles.* J. Fluid Mech. 370, 29–52.

Jenkins, J. T., Cundall, P. A. & Ishibashi, I., 1989. *Micromechanics modeling of granular material.* In Powders and grains (ed. J. Biarez & R. Gourves), pp. 257–264. Rotterdam: Balkema.

Jenkins, J. T. & Hanes, D. M., 1998 *Collisional sheet flows of sediment driven by a turbulent fluid.* J. Fluid Mech. 370, 29–52.

Jensen, A., Pedersen, G.K., Wood, D.J., 2003. *An experimental study of wave run-up at a steep beach.* Journal of Fluid Mechanics 486, 161–188.

Kamphuis, J.W., 1991. *Alongshore sediment transport rate distribution.* In: Coastal Sediments '91, ASCE, pp. 170–183.

Kamphuis, J.W., 2002. *Alongshore transport of sand*, Proceedings of the 28th Coastal Engineering Conference, ASCE, in press.

Karambas, T.V., Koutitas, C., 2002. *Surf and swash zone morphology evolution induced by nonlinear waves.* Journal of Waterway, Port, Coastal, and Ocean Engineering, ASCE 128 (3), 101–142.

Karambas, T.V., 2003. *Modelling of infiltration–exfiltration effects of cross-shore sediment transport in the swash zone.* Coastal Engineering Journal 45, 63–82.

Karambas, T.V., 2006. *Prediction of sediment transport in the swash zone by using a nonlinear wave model.* Continental Shelf Research 26, 599–609.

Karunarathna, H., Chadwick, A., Lawrence, J., 2005. *Numerical experiments of swash oscillations on steep and gentle beaches.* Coastal Engineering 52, 497–511.

Kennedy, A.B., Chen, Q., Kirby, J., Dalrymple, R.A., 2000. *Boussinesq modeling of wave transformation, breaking, and run-up.* I: 1D. Journal of Waterway, Port, Coastal, and Ocean Engineering, ASCE 126 (1), 39–47.

Kirby, J.T., 2003. *Boussinesq models and applications to nearshore wave propagation, surf zone processes and wave-induced currents*. In: Lakhan, C. (Ed.), Advances in Coastal Engineering. Elsevier, Amsterdam.

Kobayashi, N., Seo, S.N., 1985. *Fluid and sediment interaction over a plan bed.* Journal of Hydraulic Engineering 111 (6), 903–921.

Kobayashi, N., De Silvia, G.S., Watson, K.D., 1989. *Wave transformation and swash oscillation on gentle and steep slopes.* Journal of Geophysical Research 94 (C1), 951–966.

Kobayashi, N., Poff, M.T., 1994. *Numerical model RBREAK2 for random waves on impermeable coastal structures and beaches.* Research Report No. CACR-94-12, Center for Applied Coastal Research, Department of Civil Engineering, University of Delaware, Newark, 325pp.

Kobayashi, N., Agarwal,A., Johnson,B.D., 2007. *Longshore current and sediment transport on beaches.* Journal of Waterway, Port, Coastal, andOcean Engineering, ASCE133(4),296–304.

Komar, P.D., Inman, D.L., 1970. *Longshore sand transport on beaches.* Journal of Geophysical Research 75(30), 5514–5527.

Komar, P.D., 1998. *Beach processes and sedimentation (2nd edition).* Prentice-Hall, New Jersey, 545 p.

Koshizuka, S., Go, S., Oka, Y., Tanizawa, K., 2004. *Numerical analysis of a two-dimensional experiment of shipping water on deck using a particle method.* Proceedings of ASME HTFED'04.

Kothe, D.B., Mjolsness, R.C., Torrey, M.D., 1991. *RIPPLE: a computer program for incompressible flows with free surfaces*, Los Alamos National Laboratory.

Kumar, V.S., Anand, N.M., Chandramohan,P., Naik, G.N., 2003. *Longshore sediment transport rate – measurement and estimation, central west coast of India.* Coastal Engineering 48,95–109.

Lara, J.L., Losada, I.J., Liu, P.L.-F., 2006. *Breaking waves over a mild gravel slope: experimental and numerical analysis.* Journal of Geophysical Research, AGU, Vol. 111, C11019; doi: 10-1029/2005 JC003374.

Lara J.L., Losada I.J., R. Guanche, 2008. *Wave interaction with low-mound breakwater using a rans model.* Ocean Engineering, 56, 543-558.

Lara, J.L., Ruju, A. and Losada, I.J., 2011. *Reynolds Averaged Navier-Stokes modelling of long waves induced by a transient wave group on a beach.* Proceedings of the Royal Society A, vol. 467, 1215-1242.

Larson, M., Kubota,S., Erikson,L., 2004. *Swash-zone sediment transport and foreshore evolution: field experiment sand mathematical modeling.* Marine Geology 212 (1–4), 61–80.

Lemos, C.M., 1992. *Wave breaking.* Springer-Verlag, New York, USA.

Leont'yev, I.O., 1999. *Modelling of morphological changes due to coastal structures.* Coastal Engineering 38,143–166.

Lin, P., 1998. *Numerical modeling of breaking waves.* Ph.D. Thesis, Cornell University.

Lin, P., Liu, P.L.-F., 1998a. *A numerical study of breaking wave in the surf zone.* Journal of Fluid Mechanics 359, 239–264.

Lin, P., Liu, P.L.-F., 1998b. *Turbulence transport, vorticity dynamics, and solute mixing under plunging breaking waves in surf zone.* Journal of Geophysical Research 103, 15677–15694.

Lin, P., Liu, P.L.-F., 1999. *Internal wave maker for Navier-Stokes equations models.* Journal of Waterway, Port, Coastal, and Ocean Engineering, ASCE 125, 207–215.

Liu, P.L.-F., Lin, P., 1997. *A numerical model for breaking waves: the volume of fluid method.* Research Report No. CACR-97-02, Center for Applied Coastal Research, Ocean Engineering Laboratory, University of Delaware, Newark, DE.

Liu, P.L.-F., Lin, P., Chang, K.-A., Sakakiyama, T., 1999. *Numerical modeling of wave interaction with porous structures.* J. Waterw., Port, Coast., and Ocean Eng., ASCE 125 (6), 322 – 330.

Liu, H., Sato, S., 2006. *A two-phase flow model for asymmetric sheet flow conditions.* Coastal Engineering 53, 825–843.

Losada I.J., 2003. *Advances in modeling the effects of permeable and reflective structures on waves and nearshore flows.* In: Chris Lakhan, V. (Ed.), Advances in Coastal Modeling. Elsevier Oceanography Series, vol. 67.

Losada, I.J., Lara, J.L., Christensen, E.D., Garcia, N., 2005. *Breaking process, velocities and turbulence intensity around low crested structures.* Coastal Engineering, "DELOS" Special Issue.

Losada, I.J., J.L. Lara, R. Guanche and J.M. Gonzalez-Ondina, 2008. *Numerical analysis of wave overtopping of rubble mound breakwaters*, Coastal Engineering, ELSEVIER, 55(1), 47-62 (2008)

Lynett, P., Wu, T.-R., Liu, P.L.-F., 2002. *Modelling wave run-up with depth-integrated equations.* Coastal Engineering 46, 89–107.

Lynett, P., Liu, P.L.-F., 2004. *A two-layer approach to water wave modeling.* Proceedings of the Royal Society of London, Series A 460, 2637–2669.

Lynett, P., 2006. *Nearshore modeling using high-order Boussinesq equations.* Journal of Waterway, Port, Coastal, and Ocean Engineering, ASCE 132 (5), 348–357.

McTigue, D. F., 1981. *Mixture theory for suspended sediment transport.* J. Hydraul. Div. ASCE 107, 659–673.

Madsen, O.S., 1991. *Mechanics of cohesionless sediment transport in coastal waters.* Coastal Sediments '91. ASCE, Seattle, Washington, pp. 15–27.

Madsen, O.S., 1993. Sediment transport on the shelf. In: Proceedings of the Sediment Transport Workshop DRP TA1, 8–9 June. CERC, Vicksburg, MS.

Madsen, P.A., Sørensen, O.R., Schaffer, H.A., 1997b. *Surf zone dynamics simulated by a Boussinesq type model. Part II. Surf beat and swash oscillations for wave groups and irregular waves.* Coastal Engineering 32, 289–319.

Masselink, G., Hughes, M., 1998. *Field investigation of sediment transport in the swash zone.* Continental Shelf Research 18 (10), 1179–1199.

Masselink, G., Evans, D., Hughes, M.G., Russell, P., 2005. *Suspended sediment transport in the swash zone of a dissipative beach.* Marine Geology 216, 169–189.

Meyer-Peter, E., Muller, R., 1948. *Formulas for bed-load transport.* In: Proceedings of the 3rd Meeting of the International Association for Hydraulic Research, Stockholm, Sweden, pp. 39–64.

Miles, L., Newton, A. C., Defries, R., Ravilious, C., May, I., Blyth, S., Kapos, V., Gordon, J., 2006. A global overview of the conservation status of tropical dry forests. Journal of Biogeography 33: 491-505.

Nakayama, A., Kuwahara, F., 1999. *A macroscopic turbulence model for flow in a porous medium.* Journal of Fluids Engineering, 121: 427-433.

Nield, D.A., Bejan, A., 1999. *Convection in porous media.* 2nd edition, Springer-Verlag, New York, USA.

Nielsen, P., 1990. *Tidal dynamics of the water table in beaches.* Water Resources Research 26 (9), 2127–2134.

Nielsen, P., 2002. *Shear stress and sediment transport calculations for swash zone modeling.* Coastal Engineering 45, 53–60.

Nielsen, K.B., Mayer, S., 2004. *Numerical prediction of green water incidents.* Ocean Engineering 31 (3–4), 363–399.

Ono, M., Deguchi, I., Sawaragi, T., 1996. *Numerical modeling of sediment transport for various mode.* In: Proceedings of 25th International Conference on Coastal Engineering. ASCE, New York, pp. 3888–3900.

Owen, M.W., 1980. *Design of seawalls allowing for wave overtopping.* Technical Report EX-924. H.R. Wallingford, United Kingdom.

Park, J.C., Kim, M.H., Miyata, H., 1999. *Fully non-linear free-surface simulations by a 3D viscous numerical wave tank.* International Journal for Numerical Methods in Fluids 29 (6), 685–703.

Pedrozo-Acuña, A., Simmonds, D.J., Otta, A.K., Chadwick, A.J., 2006. *On the cross- shore profile change of gravel beaches.* Coastal Engineering 53(4), 335–347.

Pedrozo-Acuña, A., Simmonds, D.J., Chadwick, A.J., Silva, R., 2007. *A numerical- empirical approach for evaluating morphodynamic processes on gravel and mixed sand-gravel beaches.* Marine Geology 241, 1–18.

Pilkey, O. H., Hume, T., 2001. *Coastal research – the shoreline erosion problem: lessons from the past.* Water and Atmosphere, 9(2), National Institute of Water and Atmosphere, New Zealand. [http://www.niwa.cri.nz]

Pope, S.B., 2000. *Turbulent Flows.* University Press, Cambridge, UK,771pp.

Puleo, J.A., Slinn, D.N., Holland, K.T., Smith, E., Webb, B.M., 2002. *Numerical modeling of swash zone hydrodynamics.* In: Proceedings of the American Society of Civil Engineers, Cardiff, Wales, UK.

Puleo, J.A., Holland, K.T., Plant, N., Slinn, D.N., Hanes, D.M., 2003. *Fluid acceleration effects on suspended sediment transport in the swash zone.* Journal of Geophysical Research 108 (C11), 3350, 10.1029/2003JC001943.

Rakha, K.A., Deigaard, R., Brøker, I., 1997. *A phase-resolving cross shore sediment transport model for beach profile evolution.* Coastal Engineering 31, 231–261.

Raubenheimer, B., 2002. *Observations and predictions of fluid velocities in the surf and swash zones.* Journal of Geophysical Research 107 (C11), 3190.

Ribberink, J.S., Al-Salem, A.A., 1995. *Sheet flow and suspension of sand in oscillatory boundary layers.* Coastal Engineering 25, 205–225.

Richardson, J. F., Zaki, W. N., 1954. *Sedimentation and fluidization*. Part 1. Trans. IChE 32, 35–53.

Rodi, W., 1980. *Turbulence models and their application in hydraulics – a state-of-the-art review.* IAHR Publication.

Schüttrumpf, H., 2001. *Wellenüberlaufströmung bei Seedeichen – Experimentelle und Theoretische Untersuchungen.* PhD-Thesis.

Schüttrumpf, H., van Gent, M.R., 2003. *Wave overtopping at seadikes.* Proceedings of Coastal Structures, '03. American Society of Civil Engineers, pp. 431–443.

Schüttrumpf H., H. Oumeraci, 2005. *Layer thicknesses and velocities of wave overtopping flow at sea dikes*. Coastal Engineering, 52 (6), 473-495.

Shen, M.C. and Meyer, R.E., 1963. *Climb of a bore on a beach*. Part 3. Runup. J. Fluid Mech., 16: 113-125.

Shiach, J.B., Mingham, C.G., Ingram, D.M., Bruce, T., 2004. *The applicability of the shallow water equations for modelling violent wave overtopping.* Coastal Engineering 51 (1), 1–15.

Shih, T.H., Zhu, J., Lumley, J.L., 1996. *Calculation of wall-bounded complex flows and free shear flows.* International Journal for Numerical Methods in Fluids, 23: 1133-1144.

Shore Protection Manual,1984. USArmy Engineer Waterways Experiment Station, US Government Printing Office, Washington, DC. Shen, M.C., Meyer, R.E., 1963. *Climb of a bore on a beach: Part3*, run-up. Journal of Fluid Mechanics 16(8),113–125.

Shen, Y.M., Ng, C.O., Zheng, Y.H., 2004. *Simulation of wave propagation over a submerged bar using the VOF method with a two-equation k-eps turbulence modeling.* Ocean Engineering 31(1), 87–95.

Shields, A.,1936. *An wending der Ahnlichkeits Mechanik und der Turbulenz-forschung auf die Geschiebe Bewegung*, 26. Mitteilungen Preuss. Versuchan- stalt fur Wasserbau and Schiffbau, Berlin, 26pp.

Sitanggang, K., Lynett, P., 2005. *Parallel computation of a highly nonlinear Boussinesq equation model through domain decomposition.* International Journal for Numerical Methods in Fluids 49 (1), 57–74.

Smith, E.R.,Ebersole,B.A.,Wang,P.,2004. *Dependence of total longshore sediment transport rate son incident wave parameter sand breaker type.* Technical Report ERDC/CHLCHETN-IV-62, USArmy Engineer Research and Development Center, Vicksburg, MS.

Sørensen, O.R., Schaffer, H.A., Sørensen, L.S., 2004. *Boussinesq-type modelling using an unstructured finite element technique.* Coastal Engineering 50, 181–198.

Sumer, B. M., Kozakiewicz, A., Fredsoe, J. & Deigaard, R., 1996. *Velocity and concentration profiles in sheet-flow layer of movable bed.* J. Hydraul. Engng 122, 549–558.

Tajima, Y., 2004. *Waves, currents, and sediment transport in the surf zone along long, straight beaches.* Ph.D. Thesis, Massachusetts Institute of Technology, 313 pp.

Tautenhain, E., 1981. *Der Wellenu¨berlauf an Seedeichen unter Beru¨cksichtigung des Wellenauflaufs.* Mitteilungen des Franzius- Instituts. H., 53, 1 – 245.

THESEUS project "*Innovative technologies for safer European coasts in a changing climate*", FP7.2009-1, Contract 244104, is gratefully acknowledged.

Torquato, S., 1995. *Nearest-neighbor statistics for packings of hard spheres and disks*. Phys. Rev. E51, 3170–3182.

Torres-Freyermuth, A., Lara, J.L. and Losada, I.J., 2010. *Numerical modelling of short and long-wave transformation on a barred beach.* Coastal Engineering, vol. 57, 317-330.

Van der Meer, J.W., Janssen, W., 1995. *Wave run-up and wave overtopping at dikes.* In: Kabayashi, Demirbilek (Eds.),Wave Forces on Inclined and VerticalWall Structures. American Society of Civil Engineers, pp. 1–27.

Van der Meer, J.W., Bernardini, P., Snijders,W., E. Regeling, 2006. *The wave overtopping simulator.* Proceedings of the 30th International Conference on Coastal Engineering, vol. 5. World Scientific, 4654–4666.

Van der Meer, J. W., Steendam, G. J., de Raat, G., and Bernardini, P.,2008. *Further developments on the wave overtopping simulator.* Proc., 31st Int. Conf. Coastal Engineering, Vol. 4, ASCE, Reston, Va., 2957–2969.

Van der Meer, J.W., R. Schrijver, B. Hardeman, A. van Hoven, H. Verheij and G.J. Steendam, 2009. *Guidance on erosion resistance of inner slopes of dikes from three years of testing with the Wave Overtopping Simulator.* Proc. ICE, Breakwaters, Marine Structures and Coastlines; Edinburgh, UK.

Van der Meer J. W., Hardeman B., Steendam S.J., Schüttrumpf H., H. Verheij, 2010. *Flow depth and velocities at crest and landward slope of a dike, in theory and with the wave overtopping simulator.* ASCE, Proc. ICCE 2010, Shanghai.

Van Wellen, E., Baldock, T., Chadwick, A.J., Simmonds, D., 2000. *STRAND: a model for longshore sediment transport in the swash zone.* In: Proceedings of the 27th International Conference on Coastal Engineering, ASCE, Sydney, pp. 3139–3150.

Van Gent, M.R., 1994. *The modelling of wave action on and in coastal structures.* Coastal Engineering, 22: 311-339.

Van Gent M.R., 2002. *Wave overtopping events at dikes.* Proceedings of the 28th International Coastal Engineering Conference, vol. 2. World Scientific, 2203–2215.

Victor, L., J.W. van der Meer and P. Troch, 2012. *Probability distribution of individual wave overtopping volumes for smooth impermeable steep slopes with low crest freeboards.* Coastal Engineering, 64, pp.87–101.

Wassing, F., *Model investigations of wave run-up on dikes carried out in the Netherlands during the past twenty years*, Proc. 6th Conf. Coastal Eng., Gainesville, 1957, p. 700-714.

Walton Jr., T.L., Bruno, R.O., 1989. *Longshore transport at a detached break water, phase II.* Journal of Coastal Research 65 (9), 667–668.

Watanabe, A., 1992. *Total rate and distribution of longshore sand transport.* In: Proceedings of the 23rd Coastal Engineering Conference, ASCE, New York, pp. 2528–2541.

Wood, D.J., Pedersen, G.K., Jensen, A., 2003. *Modelling of run-up of steep non- breaking waves.* Ocean Engineering 30, 625–644.

Yeganeh-Bakhtiary, A., Gotoh, H., Sakai, T., 2000. *Applicability of Euler–Lagrange coupling multiphase-flow model to bed-load transport under high bottom shear.* Journal of Hydraulic Research 38, 389–398.

Zanuttigh B., J.W. van der Meer, *Wave reflection from coastal structures in design conditions*, Coastal Engineering, 2008, 55 (10), pp. 771 – 779.

Zanuttigh, B., J.W. van der Meer, T. Bruce and S. Hughes, 2013. *Statistical characterization of extreme overtopping wave volumes*. Proc. ICE 2013, Edinburgh.

Zhang, Y., Campbell, C. S., 1992 *The interface between fluid-like and solid-like behavior in two-dimensional granular flows.* J. Fluid Mech. 237, 541–568.

Zhang, Q., Liu, P.L.-F., 2008. *A numerical study of swash flows generated by bores.* Coastal Engineering 55 (12), 1113–1134. Zhao, Q., Armfield, S., Tanimoto, K., 2004. Numerical simulation of breaking waves by a multi-scale turbulence model. Coastal Engineering 51, 53–80.

Zhao, Q., S. Armfield and K. Tanimoto, 2004: *Numerical simulation of breaking waves by a multi-scale turbulence model.* Coastal Engineering 51, pp. 53-80.

Zhou, J.G., Stansby, P.K., 1999. *An arbitrary Lagrangian–Eulerian model with non- hydrostatic pressure for shallow water flows.* Computer Methods in Applied Mechanics and Engineering 178, 199–214.